Title
Lensfree Holographic On-Chip Imaging and Three-Dimensional Tracking

Author
Su, Ting-Wei

Publication Date
2012

Peer reviewed|Thesis/dissertation

UNIVERSITY OF CALIFORNIA

Los Angeles

Lensfree Holographic On-Chip Imaging and Three-Dimensional Tracking

A dissertation submitted in partial satisfaction of the
requirements for the degree Doctor of Philosophy
in Electrical Engineering

by

Ting-Wei Su

2012

ABSTRACT OF THE DISSERTATION

Lensfree Holographic On-Chip Imaging and

Three-dimensional Tracking

By

Ting-Wei Su

Doctor of Philosophy in Electrical Engineering

University of California, Los Angeles, 2012

Professor Aydogan Ozcan, Chair

Despite the rapid progress in optical imaging, most of the advanced microscopy modalities still require complex and costly set-ups that unfortunately limit their use beyond well-equipped laboratories. To provide affordable and easy-to-use microscopes for resource-limited settings, I developed a holographic on-chip imaging technology that utilizes cost-effective and compact optoelectronic components to enable the digital reconstruction of microscopic amplitude and phase images for biological cells with sub-micron resolution over a field-of-view of >24 mm^2. Without the need for any lenses, bulky optical components or coherent sources such as lasers, this partially-coherent computational imaging modality can automatically analyze thousands of cells in parallel for their cell type, concentration, structure, and dynamics. As being compact, light-weight, cost-effective, high-throughput, and highly-sensitive, this lensfree imaging

technology is especially suitable for field diagnostics applications involving global health problems such as HIV, malaria, infectious diarrhea, or male infertility.

Based on this lensfree imaging technology, I also devised a dual-angle dual-color holographic scheme to achieve sub-micron accuracy and sub-12-minisecond resolution for three-dimensional tracking of >1,500 human sperms in a field-of-view of >17 mm^2 and a depth-of-field of >0.5 mm. The high accuracy and high throughput of this lensfree imaging platform enabled the first observation of human sperms' tight (1-6um wide), fast (3-20 r/sec), and rare (4-5%) helical trajectories, which surprisingly are dominated by right-handed ones (~90%) and can be significantly suppressed by seminal plasma. Such a high-throughput 3D tracking platform can also be a valuable tool for observing the statistical swimming patterns of various micro-organisms, leading to new insights in their 3D dynamics.

The dissertation of Ting-Wei Su is approved.

Benjamin M. Wu

Benjamin Williams

Oscar M. Stafsudd, Jr.

Aydogan Ozcan, Committee Chair

University of California, Los Angeles

2012

To my wife and my son

Table of Contents

Acknowledgements

First of all, I would like to thank my advisor, Dr. Aydogan Ozcan, for his guidance and support throughout my PhD study. The creative and energetic atmosphere that he creates in the lab has inspired me to pursue the highest level of achievement for my research. I am really grateful that he gave me a chance to be a part of this exciting and productive environment. In addition, I would like to thank my doctoral committee members, Dr. Benjamin Wu, Dr. Benjamin Williams, and Dr. Oscar Stafsudd, for their kind support and valuable comments on my dissertation.

During my study at UCLA, I had the fortunate opportunity to work together with many brilliant people in my lab. Sungkyu, Bahar, Ikbal, Derek, Anthony, Onur, Ahmet, Serhan, Waheb, Gabriel, MJ, Kellie, Alon, Wei, Zoltan, Sam, Steve, Frank, Caglar, Serap, Liang, Uzair, Oguzhan, Evan, Euan, and Qingshan. My collaboration with you has greatly enriched my dissertation and I also want to thank you for your warm friendship.

I also had the privilege to corporate with various people both inside and outside UCLA, receiving generous help and valuable suggestions from Christina Wang and Andrew Leung in Harbor-UCLA Medical Center; Lora Turovsky, Rama Tyagi, and Judylyn Rubio-Hong in California Cryobank; Prof. Eric Chiou and his students, Ting-Hsiang, Kuo-wei, Ray, Yu-Chun; Prof. Dino Di Carlo and his students, Danny, Westbrook, Ivan. I sincerely thank the people listed above for their kind support.

Lastly, I have to thank my wife and my son for their understanding and patience when I was busy with my research work and couldn't spend much time with them. Also, I need to thank my mom and my father-in-law for their company with my wife and my son so that I can focus on my work. The encouragements from my friends and my family members, including those from my

parents, my grandparents, my uncles/aunts, and my brother, were my strongest support to overcome this great challenge. I thank all of you.

Vita

1996-2000	Bachelor of Science in Electrical Engineering
	National Taiwan University, Taiwan
2000-2002	Master of Science in Electro-Optical Engineering
	National Taiwan University, Taiwan
2002-2004	Instructor
	Army Comm. Elec. Info. School, Taiwan
2004-2007	Senior Engineer
	AU Optronics Corp. (AUO), Taiwan
2007-2012	Doctor of Philosophy in Electrical Engineering
	University of California, Los Angeles, U.S.

Publications

Sungkyu Seo, Ting-Wei Su, A. Erlinger, and A. Ozcan, "Lensfree on-chip cytometry using tunable wavelength illumination and digital noise reduction", *Cellular and Molecular Bioengineering*, Vol. 1, Nos. 2–3, 2008, 146–156.

Ting-Wei Su, Sungkyu Seo, A. Erlinger, and A. Ozcan, "High-throughput Imaging and Characterization of a Heterogeneous Cell Solution On a Chip", *Biotechnology and Bioengineering*, Vol. 102, No. 3, February 15, 2009.

Sungkyu Seo, Ting-Wei Su, D. K. Tseng, and A. Ozcan, "Lensfree Holographic Imaging for On-Chip Cytometry and Diagnostics," Lab Chip, 2009, 9, 777 – 787.

O. Mudanyali, A. Erlinger, S. Seo, Ting-Wei Su, D. Tseng, and A. Ozcan, "Lensless On-chip Imaging of Cells Provides a New Tool for High-throughput Cell-Biology and Medical Diagnostics," Journal of Visualized Experiments, no. 34, Dec. 2009.

A. F. Coskun, Ting-Wei Su, and A. Ozcan, "Wide field-of-view lens-free fluorescent imaging on a chip," Lab on a Chip, vol. 10, no. 7, p. 824, 2010.

Bahar Khademhosseinieh, Ikbal Sencan, Gabriel Biener, Ting-Wei Su, Ahmet F. Coskun, Derek Tseng, and Aydogan Ozcan, "Lensfree on-chip imaging using nanostructured surfaces," Applied Physics Letters, vol. 96, no. 17, p. 171106, 2010.

Ting-Wei Su, S. O. Isikman, W. Bishara, D. Tseng, A. Erlinger, and A. Ozcan, "Multi-angle lensless digital holography for depth resolved imaging on a chip," Optics Express, vol. 18, no. 9, pp. 9690-9711, Apr. 2010.

Sungkyu Seo, Serhan O. Isikman, Ikbal Sencan, Onur Mudanyali, Ting-Wei Su, Waheb Bishara, Anthony Erlinger and Aydogan Ozcan, "High-Throughput Lens-Free Blood Analysis on a Chip," Analytical Chemistry, vol. 82, no. 11, pp. 4621-4627, Jun. 2010.

A. F. Coskun, I. Sencan, Ting-Wei Su, and A. Ozcan, "Lensless wide-field fluorescent imaging on a chip using compressive decoding of sparse objects," Optics Express, vol. 18, no. 10, pp. 10510-10523, May. 2010.

W. Bishara, Ting-Wei Su, A. F. Coskun, and A. Ozcan, "Lensfree on-chip microscopy over a wide field-of-view using pixel super-resolution," Optics Express, vol. 18, no. 11, pp. 11181-11191, May. 2010.

Ting-Wei Su, A. Erlinger, D. Tseng, and A. Ozcan, "Compact and Light-Weight Automated Semen Analysis Platform Using Lensfree on-Chip Microscopy," Analytical Chemistry, vol. 82, no. 19, pp. 8307-8312, Oct. 2010.

H. Zhu, O. Yaglidere, Ting-Wei Su, D. Tseng, and A. Ozcan, "Cost-effective and compact wide-field fluorescent imaging on a cell-phone," Lab on a Chip, vol. 11, no. 2, p. 315, 2011.

B. Khademhosseinieh, G. Biener, I. Sencan, Ting-Wei Su, A. F. Coskun, and A. Ozcan, "Lensfree sensing on a microfluidic chip using plasmonic nanoapertures," Applied Physics Letters, vol. 97, no. 22, p. 221107, Dec. 2010.

A. F. Coskun, I. Sencan, Ting-Wei Su, and A. Ozcan, "Lensfree Fluorescent On-Chip Imaging of Transgenic Caenorhabditis elegans Over an Ultra-Wide Field-of-View," PLoS ONE, vol. 6, no. 1, p. e15955, Jan. 2011.

A. F. Coskun, I. Sencan, Ting-Wei Su, and A. Ozcan, "Wide-field lensless fluorescent microscopy using a tapered fiber-optic faceplate on a chip," The Analyst, 2011.

W. Bishara, U. Sikora, O. Mudanyali, Ting-Wei Su, O. Yaglidere, S. Luckhart, and A. Ozcan, "Holographic pixel super-resolution in portable lensless on-chip microscopy using a fiber-optic array", Lab Chip, 2011, 11, 1276-1279.

S.O. Isikman, W. Bishara, O. Mudanyali, I. Sencan, Ting-Wei Su, D. Tseng, O. Yaglidere, U. Sikora, A. Ozcan, Lensfree On-Chip Microscopy and Tomography for Bio-Medical Applications, Selected Topics in Quantum Electronics, IEEE Journal of , vol.PP, no.99, pp.1.

Coskun, A. F., Ting-Wei Su, Sencan, I., Ozcan, A., Lensless Fluorescent Microscopy on a Chip. http://www.jove.com/details.php?id=3181 doi: 10.3791/3181. J Vis Exp. 54 (2011).

S.O. Isikman, A. Greenbaum, M. Lee, W. Bishara, O. Mudanyali, Ting-Wei Su, and A. Ozcan, "Lensfree computational microscopy tools for cell and tissue imaging at the point-of-care and in low-resource settings," Anal. Cell. Pathology, vol. 36, pp. 1-19 (2012).

Chapter 1 Introduction

For decades optical microscopy has been the workhorse of various fields including engineering, physical sciences, medicine and biology. Despite its long history, until relatively recently, there has not been a significant change in the design and working principles of optical microscopes. Over the last decade, motivated partially by the quest to better understand the realm of the nano-world, super-resolution techniques started a renaissance for optical microscopy by addressing some of the most fundamental limitations of optical imaging such as the diffraction limit.[1–8] Besides these super-resolution techniques, several other novel imaging architectures were also implemented to improve the state of the art in optical microscopy towards better speed, signal to noise ratio (SNR), contrast, throughput, specificity, etc.[9–14] This recent progress in microscopy utilized various innovative technologies to overcome the fundamental barriers in imaging and has created significant excitement in a diverse set of fields by enabling new discoveries to be made. However, together with this progress, the overall complexity and the cost of the optical imaging platform relatively increased which limits the wide spread use of some of these advanced optical imaging modalities beyond well-equipped laboratories.

In the meantime, we have been also experiencing a rapid advancement in digital technologies, with much cheaper two-dimensional solid state detector arrays having significantly larger areas with smaller pixels, better dynamic ranges, frame rates and signal to noise ratios, as well as much faster, cheaper and more powerful digital processors and memories. This on-going digital revolution, when combined with advanced imaging theories and numerical algorithms, also creates an opportunity for optical imaging and microscopy to face another dimension in this renaissance towards simplification of the optical imaging apparatus, making it significantly more

compact, cost-effective and easy to use, potentially without a trade-off in its performance. As I illustrate in this dissertation, lensfree computational imaging can be considered to be at the heart of this new opportunity and when combined with the advanced state of the art and cost-effective nature of digital electronics, it can provide a transformative solution to some of the unmet needs of bio-medicine and diagnostics especially for resource-limited settings.

Lenses for decades have been helping detectors (analog or digital) to operate at the lowest possible space-bandwidth product that are determined by the desired field-of-view and the resolution of the image. However, the above discussed digital revolution has already advanced the state of the art for digital imagers such that a 2D space-bandwidth product of several tens of million is readily available nowadays. This implies that today's detector arrays are now much better suited to handle the information distortion caused by diffraction, which may then raise questions on the absolute necessity of the use of lenses in optical imaging. Moreover, today's digital processors together with novel algorithms are also in much better shape to process, almost instantaneously, the acquired information at the detector end for taking over the job of a physical lens. Looking at this picture, one can conclude that the widespread use of lenses (or similar wavefront shaping elements) in optical imaging can now be potentially replaced for several application needs (specifically for cellular micro-analysis) by cost-effective, compact and much simpler optical architectures that compensate in the digital domain for the lack of complexity of optical components. This approach should especially address the needs and the requirements of resource limited settings, potentially providing a leapfrog in our fight against various global health related problems involving infectious diseases.

Quite importantly, microscopy in resource-limited settings have requirements considerably different from those of advanced laboratories, and such imaging devices should be simple to use

and operate, cost-effective, compact, and light-weight, while at the same time being properly accurate. Another field that would enormously benefit from lensfree, compact and cost-effective on-chip digital imagers is the field of microfluidics.[15,16] Over the last decade, microfluidics has revolutionized the available toolset to handle cells by significantly reducing the required device and reagent volumes as well as the associated costs. Despite all the progress that is taken on merging optical technologies with microfluidics,[17] one area that still remains relatively low-throughput, bulky and costly is the optical microscopy platform that is coupled to the micro-channels. Without significant miniaturization and simplification of this imaging platform together with an increase in throughput, the true extent of the microfluidic revolution cannot be fully realized especially for cytometry applications in the field.

The fruits of this thinking have already appeared in the literature, where various lensfree on-chip imaging architectures were successfully demonstrated.[17–26] Among these approaches, lensfree digital holography[18–22] deserves a special attention since with new computational algorithms and mathematical models,[27] it has the potential to make the most out of this digital revolution. In this context, lensfree digital in-line holography has already been successfully demonstrated for high-resolution microscopy and 3D imaging of cells and other micro-organisms.[19] Conventional coherent lensfree in-line holography approaches demand near-perfect spatial coherence for illumination, and therefore require focusing of a laser light on a small aperture that is on the order of a wavelength for spatial filtering.[19,22] The use of a small aperture size (e.g., 1-2μm) requires a mechanically stable and a carefully aligned system together with a high numerical aperture (NA) lens to efficiently couple the laser radiation to the aperture for improved light throughput. In addition, keeping such a small aperture clean and operational over an extended period of time can be another challenge especially for field use. Further, the cells of

interest are typically positioned far away (e.g., >1-2 cm) from the sensor surface such that the holographic signature of each cell is spread almost over the entire sensor area, where all the cells' signatures significantly overlap. Such an approach unfortunately limits the imaging field-of-view (FOV) at the cell plane. All these requirements not only relatively increase the cost and the size of the optical instrument, but also make lensfree coherent in-line holography somewhat inconvenient for use in resource limited settings.

Incoherent or partially coherent sources in holography have also been utilized in different lens-based optical architectures.[13,28–31] These holographic imaging techniques are not on-chip as they utilize various bulky optical components and therefore they can be considered under the same category as the advanced imaging modalities discussed in the introduction making them less suitable for field use. Much simpler approaches using partially coherent lensfree in-line holography have also been recently demonstrated for imaging of latex particles,[21,32] but these techniques also suffer from a small field-of-view as they position the objects-of-interest far away from the sensor surface. Further, these studies used coupling optics for the illumination such as a microscope objective-lens and had relatively coarse imaging performance.

In this dissertation, I report an alternative incoherent cell holography and microscopy platform that utilizes cost-effective and compact optical components to enable digital recognition and microscopic imaging of cells, achieving sub-cellular resolution over a large field-of-view without the need for any lenses, other bulky optical components or coherent sources such as lasers. With this lensless system, I illustrate that we can record individual phase and amplitude holograms of various cell types for digital recognition and automated counting of each cell type based on their 2D holographic signatures, as well as accurately reconstruct their microscopic images featuring sub-micron resolution over a >24 mm^2 field-of-view even at cell densities

reaching up to ~0.4 million cells/μL. Because this platform utilizes simple, compact, light-weight and cost-effective optical components that are misalignment tolerant it may also provide an important tool for telemedicine based cytometry and diagnostics applications in field-portable settings for various global health problems such as HIV, malaria, infectious diarrhea, or male infertility. Toward this end, here I also demonstrate the 2D and 3D tracking with this lensfree imaging technology to investigate the dynamical motion of motile cells, such as human sperms. Especially as a high-accuracy high-throughput 3D tracking platform, this technology can be a valuable tool for observing the statistical swimming patterns of various micro-organisms, leading to new insights in their 3D dynamics.

There are several aspects of this novel platform that makes it highly advantageous for cytometry applications in resource limited settings. *(1)* The light source in this holographic approach does not need to be a laser such that an incoherent source, such as light emitting diode, can be used without the need for any lenses or other bulky optical components. This feature greatly simplifies the optical set-up, making it cost-effective and compact, as well as eliminating the coherent speckle noise[33] and substrate induced multiple-reflection effects in cell holograms. *(2)* The presented on-chip holography approach does not require a small aperture size for illumination and therefore improves the light throughput of the imaging system by orders-of-magnitude without causing an issue for cell hologram pattern analysis or digital image reconstruction. This large aperture size (e.g., 50-100 μm) also makes it robust to mechanical misalignments or potential clogging problems permitting a long time of operation without imaging artifacts or the need for realignment, making it highly suitable for field use. *(3)* Because no optical lens is used and the cells of interest are placed much closer to the sensor array (typically <0.5-2 mm) than to the light source, I can image a much larger field-of-view typically

by >10 fold than an optical microscope or >100 fold than a conventional lensless in-line holographic microscope. *(4)* Apart from reconstructing microscopic images of cells through holographic processing of the embedded optical phase, we can also detect a unique two dimensional holographic texture (i.e., a fingerprint) corresponding to each cell, which provides an alternative source of information that complements the reconstructed cell images. Through pattern/texture analysis of such holographic cell signatures (both phase and amplitude) it is possible to recognize the type and the state of each cell of interest (without digital reconstruction), which is especially important for cytometry applications towards making a diagnostic decision e.g., based on a comparison of healthy vs. diseased cell hologram signatures. *(5)* The wide light-acceptance angle of image sensors and the small object-sensor distance allow the object images of different perspectives (i.e., viewing angles) to be captured easily by changing the illumination angles of light sources. This feature enables high-throughput tomographic imaging and high-accuracy 3D dynamic tracking of micro-objects to be done in a compact and cost-effective format. *(6)* The performance of the imaging system, such as resolution, field-of-view, or frame rate, is highly scalable with the technological advancement of image sensor fabrication. Whenever a better image sensor becomes available on the market, the technology gets an immediate upgrade in its performance. Such scalability places my lensfree on-chip microscopy technology on a sweet spot to follow the rapid trend of the Moore's Law observed in the micro-electronics industry.

Chapter 2 Lensfree Holographic Imaging for On-Chip Cytometry and Diagnostics

2.1 Introduction

Flow cytometry is a powerful technology that enables counting, characterization and sorting of cells flowing through a hydro-dynamically concentrated channel. By collecting fluorescence and scattered light from the cells as a function of time, this technology can provide various sources of information such as the count, type or surface morphology variation of the cells, which are all very important in clinical diagnostics.[34] Most flow cytometers use rather bulky and expensive equipment such as photomultiplier tubes (PMTs) and avalanche photodiodes, which limit their application at the point-of-care especially in resource limited settings.[35,36] To address this issue, there have been a variety of studies to miniaturize conventional bench-top flow cytometers into portable micro flow systems. For instance, to miniaturize the source and detection in micro flow cytometry, researchers adopted commercial waveguides that are integrated with micro-fluidic channels.[37–40] Cleaved ends of these waveguides are aligned to the micro-channel to illuminate and detect the scattered or fluorescence light from the cells. To address another significant challenge in miniaturized system design(i.e., to provide reliable and rapid flow of cells on a chip) electrokinetic focusing in micro-fabricated channel structures has also been widely used to achieve 2D and even 3D hydrodynamic focusing.[41–46] All of these heroic efforts and others[47–50] are still based on the fundamental principles of conventional flow cytometry and analyze cells one at a time (i.e., on-chip detection is achieved serially).

In this chapter I introduce a lensless holographic imaging platform that can provide a versatile solution to on-chip cytometry and diagnostics. In this scheme, by use of a variable

pinhole, I control the spatial coherence of the illumination source to enable lensfree recording of the holographic diffraction pattern of each cell on the chip using a high-resolution opto-electronic sensor array that has ~2 μm pixel size (see Fig. **Error! Reference source not found.**). fter recording of this holographic lensfree image, a custom developed decision algorithm is utilized to process the 2D texture of acquired holograms to rapidly recognize and characterize the type and 3D location of each cell/micro-object located within a heterogeneous solution of interest. Since this holographic approach does not rely on conventional optical components such as lenses, mirrors, beam splitters, etc., it offers a flexible, compact and cost-effective alternative for many on-chip diagnostics applications such as whole blood analysis.

The holographic diffraction pattern of each cell/micro-object is created by the interference of the scattered light from the cell/micro-object with the un-scattered light directly emanating from the source. This holographic diffraction pattern should not be confused with the classical diffraction signature of the same micro-object. When recorded with a high-resolution sensor array, holographic diffraction signature exhibits several advantages compared to the classical diffraction pattern of the same micro-object. These advantages will be further explored in the Discussions Section.

Since there exist several different forms of on-chip cytometry, lensless imaging or holographic imaging systems, let me briefly outline the key differences between some of the existing systems and the approach of this article:

(1) When compared to miniaturized flow cytometers, the proposed approach does not involve any fluid flow and captures the holographic diffraction information of the cells on the chip all in parallel within less than 0.3 seconds. Quite different from flow-cytometry, my approach relies on

digital processing of the holographic diffraction signatures of different cell types to rapidly characterize a heterogeneous cell solution on a chip.

(2) When compared to existing digital in-line holographic microscopy (DIHM) systems[19,22,51] the approach reported in this chapter differs in several significant ways such as much simpler digital processing, simpler optical design, and elimination of the use of lenses. However, for the general audience, in the Discussions Section I will further expand on these key technical differences between DIHM and my approach.

(3) There exist various other *non-holographic* lensless imaging and microscopy approaches in the literature.[23,52–54] Several of these approaches are not designed for cytometry, but rather aim to achieve high resolution imaging of e.g., *C. elegans* within a micro-fluidic channel. For instance, the ingenious concept of opto-fluidic microscopy (OFM)[23,52,53] can achieve a high spatial resolution of ~0.5 μm on a chip using a slanted array of holes that capture a transformed image of the micro-object of interest as it moves through a micro-fluidic channel at a constant speed. My lensless on-chip cytometry approach makes use of digital holography to identify different cell types on a chip, and in this sense is quite different from these on-chip microscopy systems. Furthermore, my approach does not utilize any fluidic motion unlike OFM and therefore can monitor a larger field of view much faster, increasing the throughput of cell characterization.

(4) Finally I would like to discuss the major differences of my new holographic cytometry approach with respect to some of the existing on-chip imaging work that my lab has previously demonstrated.[24–26] To realize high-throughput cell counting and characterization within a compact and cost-effective platform, my lab have recently reported a lensfree on-chip imaging platform termed LUCAS (***L***ensfree ***U***ltra-wide-field **C**ell monitoring ***A***rray platform based on

Shadow imaging).[24] In this initial proof-of-concept, using spatially incoherent broadband white-light illumination I recorded the classical diffraction pattern (not the holographic diffraction) of a homogenous solution of cells using a low-resolution sensor array that had ~9 μm pixel size. In this primitive LUCAS platform, the volume of the sample solution that could be monitored within a second was limited to <0.1 ml.[24] Relatively recently, this original LUCAS platform has been further improved by my lab using narrowband (i.e., monochromatic) tunable wavelength illumination together with a custom-developed pattern recognition algorithm.[25,26] These improvements enabled label-free characterization of a heterogeneous cell population on a chip over a field of view of ~10 cm^2 and a depth of field of >4 mm, corresponding to a solution volume of >4 ml.

Holographic on-chip cytometry approach of this manuscript is significantly different from the existing LUCAS based techniques.[24–26] LUCAS utilizes spatially incoherent light which implies that the detected quantity is simply the classical diffraction pattern of each cell/microparticle, whereas the proposed approach of this manuscript uses spatially coherent illumination to record the holographic diffraction of each cell/micro-object on the chip. As discussed earlier, this important difference brings several advantages to my new approach when compared to existing LUCAS systems. First, since classical diffraction fringes are due to self-interference of the scattered light from the cell with itself, they are much weaker in signal strength when compared to holographic diffraction patterns. In other words, this improved signal to noise ratio (SNR) is due to heterodyne nature of holographic interference, whereas classical diffraction can be modeled as a homodyne system. This SNR improvement is especially more pronounced for small cells or bacteria that act as weak scatterers. This point will be experimentally verified in the Results section. Second, holographic diffraction exhibits improved

signature uniformity for a given cell type, i.e., the digital similarity among different holographic signatures of the same micro-object type is significantly improved. This is especially quite relevant to enable automated pattern recognition of the target cell type within a heterogeneous solution using a decision algorithm. Third, with holographic diffraction, the signature differences among different cell types become more evident. I will quantify the statistical performance of this improvement in the Results section, however, intuitionally this improvement is due to the fact that with self-interference most phase related information of the cell/micro-object is lost, whereas by recording a hologram with respect to a reference beam (the un-scattered direct light) this phase information is now encoded into amplitude oscillations, which enriches the 2D information content of the detected cell signature on the chip. A more rigorous discussion of this claim will be provided in Chapter 3.

Another major difference between the presented technique and the previous LUCAS work[24–26] is that here I use a much higher resolution sensor array that has more than 4 fold smaller pixel size (i.e., 2.2 μm vs. 9.0 μm). The significance of this higher resolution sensor array will be further quantified in the Results section.

These significant improvements of the holographic cytometry approach permit improved performance for automated characterization of different cell types within a heterogeneous cell solution based on 2D texture analysis of the detected holograms. Apart from these noteworthy differences and advances, conceptually, the on-chip lensfree imaging idea of my holographic technique can be considered as a significant improvement of the existing LUCAS approach, and therefore to help me establish this link, I will refer to this new on-chip cytometry approach as "Holographic-LUCAS".

In summary, Holographic-LUCAS exhibits several advantages within a novel lensfree imaging and digital processing scheme to provide a flexible, compact and cost-effective alternative to existing approaches for point-of-care cytometry and diagnostics applications such a monitoring of HIV patients in resource scarce settings.

2.2 Experimental Methods

Set-up: Figure **Error! Reference source not found.** shows the experimental configuration of y Holographic-LUCAS imaging set-up. The results that are presented in this manuscript are acquired using two different sensor arrays: (1) a charged couple device (CCD, KAI-10002, Kodak) and complementary metal-oxide-semiconductor (CMOS, MT9P031, Micron) image sensor which have pixel sizes of 9.0μm (CCD) and 2.2μm (CMOS), respectively. As illustrated in the schematic diagram of Fig. **Error! Reference source not found.**(b), using these two opto-lectronic sensor arrays I recorded the holographic diffraction signatures of various micro-objects such as red blood cells, yeast cells (*S. pombe*), polystyrene micro-particles of various diameters (D=3, 5, 10 and 20μm, Duke Scientific) and *Escherichia Coli* (*E. Coli*) samples. The same optical set-up can also record the classical diffraction fringes of the cells/micro-objects by removing the pinhole or enlarging its diameter. The micro-objects to be imaged are diluted with 1X PBS, and a total solution volume of 10-100 μl is dropped on a microscope slide using a micro-pipette and gently sandwiched by another identical cover glass. Then, the sample is positioned using a vacuum pen (NT57-636, Edmund Optics) onto the active region of the sensor array. To be able to illuminate the sample volume with tunable monochromatic light (scanning a wavelength range of λ=350-1000 nm), I used a digital monochromator (Oriel Cornerstone^{TM} 260-1/4m, Newport) along with a standard grade fused silica fiber which consists of a bundle of 250μm diameter fibers (77564, Newport). For Holographic-LUCAS experiments, I used a

pinhole diameter of ~100 μm placed ~5 cm above the sensor array. As will be discussed later on, this configuration implies no fringe magnification (close to unity) for the detected holograms.

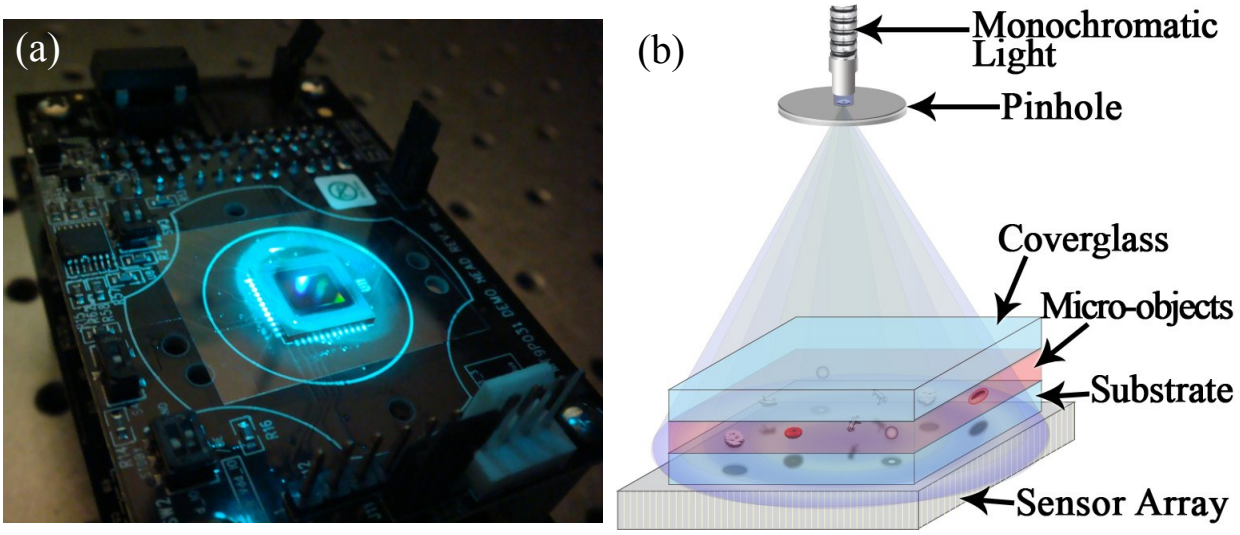

Figure 2-1 | (a) Experimental apparatus (under blue light illumination) and (b) schematic diagram of the Holographic-LUCAS platform are shown.

Image Quality Metrics and Decision Algorithm: To provide quantitative comparison for the improvement in the quality of Holographic-LUCAS images, I utilized three metrics: (1) digital signal-to-noise ratio (SNR), (2) spot/shadow radius (R_{rms}), and (3) correlation index, all of which will mathematically be defined below.

Digital SNR of my images is calculated using $SNR=|(\max(I)-\mu_b)/\sigma_b|$, where I is the light intensity on the sensor array, and μ_b and σ_b are the mean and variance of the background noise region. For R_{rms} calculations, I used the concept of root-mean-square (RMS) width which is defined as

$$R_{rms} = \sqrt{\sum_{x=1}^{W}(x-\bar{x})^2\left|f(x,y=y_0\right|^2 \Big/ \sum_{x=1}^{W}\left|f(x,y=y_0)\right|^2},$$

where W is the maximum number of pixels in the region of interest, and

$$\bar{x} = \left(\sum_{x=1}^{W} x \left| f(x, y = y_0) \right|^2 \Big/ \sum_{x=1}^{W} \left| f(x, y = y_0) \right|^2 \right).$$

In these equations, (x,y) and $f(x,y=y_0)$ denote the index of the image pixel and the detected intensity profile of a line represented by $y = y_0$, respectively.[55]

To better quantify the digital similarity between different holograms of the same cell/object type, I introduced the concept of "correlation index" which simply calculates the numerical deviation of a given cell image compared to a mean library image of the same cell type. For each cell/micro-object type a mean library image, $L(x,y)$, was formed by averaging >20 arbitrarily chosen samples within a homogenous solution that are imaged under the same conditions (*e.g.*, the same wavelength, the same depth of field *etc.*). Each individual holographic (or classical) diffraction pattern of an unknown particle (*i.e.*, $f(x,y)$) was first compared to the library image of a known particle type to calculate its "deviation" given by

$$Dev = \sum_{(x,y) \in ROI} \left| f(x,y) - L(x,y) \right|.$$

The region of interest (ROI) for each calculation occupies an equal amount of area as that of the library image. After this step, the correlation of the unknown particle image $f(x,y)$ to the average library image $L(x,y)$ is calculated using:

$$Corr = 1 - \frac{Dev - Dev_{MIN}}{Dev_{MAX} - Dev_{MIN}},$$

where Dev_{MAX} and Dev_{MIN} refer to the maximum and minimum of the deviation values of $f(x,y)$ calculated using the individual library images forming $L(x,y)$. Therefore, a target image $f(x,y)$ that has the maximum deviation from all the library images will have a correlation index of "0",

and a correlation index of "1" will be assigned to an image with minimal deviation from the same set of library images.

To characterize the acquired Holographic-LUCAS images, a 2D correlation map is calculated for each one of the existing cell/particle image libraries. The user can select which target cell libraries to be used, or otherwise, all the existing image libraries are used. To generate the 2D correlation map for each library image, first a 2D deviation profile is calculated:

$$Dev(x,y) = \sum_{(x',y')\in D_L} \left| f(x'+x, y'+y) - L(x',y') \right|,$$

where D_L represents the domain of the library image. Then the 2D deviation map is converted into a 2D correlation map using:

$$Corr(x,y) = 1 - \frac{Dev(x,y) - Dev_{MIN}}{Dev_{MAX} - Dev_{MIN}}.$$

After the creation of this 2D correlation map, potential candidates showing a large correlation peak (that is above a certain threshold value) are further investigated using R_{rms} and/or *SNR* criterion to make a characterization and counting decision. I should note here that a similar decision making process is also utilized in existing LUCAS based incoherent system.[25,26] As far as the decision algorithm is concerned, the most important difference between Holographic-LUCAS and the previous approaches in [25,26] is that the cell signatures (together with their image libraries) now exhibit richer source of texture information, together with better uniformity and SNR, which then translate into improved characterization performance, which will be quantified in the discussions to follow.

2.3 Results

To illustrate the performance of the Holographic-LUCAS platform with a high-resolution sensor array, I initially imaged a mixture of polystyrene micro-particles (3μm diameter) and *E. Coli*

samples. To provide a direct comparison, Fig. 2-2(a) shows the classical diffraction image of this mixture that is acquired with a conventional incoherent LUCAS system as described in the literature,[24–26] i.e., a pixel size of 9.0μm, under λ = 400nm and at Z = 200μm, where λ and Z are the illumination wavelength and the distance from the sample to the sensor plane, respectively. In this figure, conventional diffraction patterns of five 3μm beads and one *E. Coli* sample are shown. The same region of interest is also imaged using a 40X objective-lens as shown in Fig. 2-2(b) to verify the LUCAS results. As illustrated in Fig. 2(a), because this mixture contains small particles (3 μm) and weakly scattering phase objects (*E. coli*), the conventional LUCAS system has serious issues with signature non-uniformity and low SNR. To demonstrate the improvement of the Holographic-LUCAS platform with the high-resolution sensor array, in Fig. 2-2(d) I show the holographic diffraction pattern of the same solution sampled with a pixel size of 2.2 μm. In contrast to the poor SNR and signature non-uniformity of the conventional LUCAS system (Fig. 2-2(a)), Fig. 2-2(d) now clearly shows the details of the holographic diffraction signatures of three 3μm beads and two *E. coli* samples, which were again verified by acquiring a high resolution (40X) microscope image of the same region of interest as shown in Fig. 2-2(e). In particular, this experimental comparison illustrates significantly improved performance of the Holographic-LUCAS platform for on-chip imaging of phase objects such as *E. Coli* samples that are quite difficult to see even under a 40X objective lens. For instance, the *E. Coli* diffraction pattern which was very close to the background noise level in Fig. 2-2(a) is significantly improved in Fig. 2-2(d) with over 40 times SNR improvement even at a larger sample-to-sensor distance of Z = 625μm. Furthermore, the signature uniformity of the micro-particles is now much better (see Fig. 2-2(d)) with the use of the high-resolution holographic set-up.

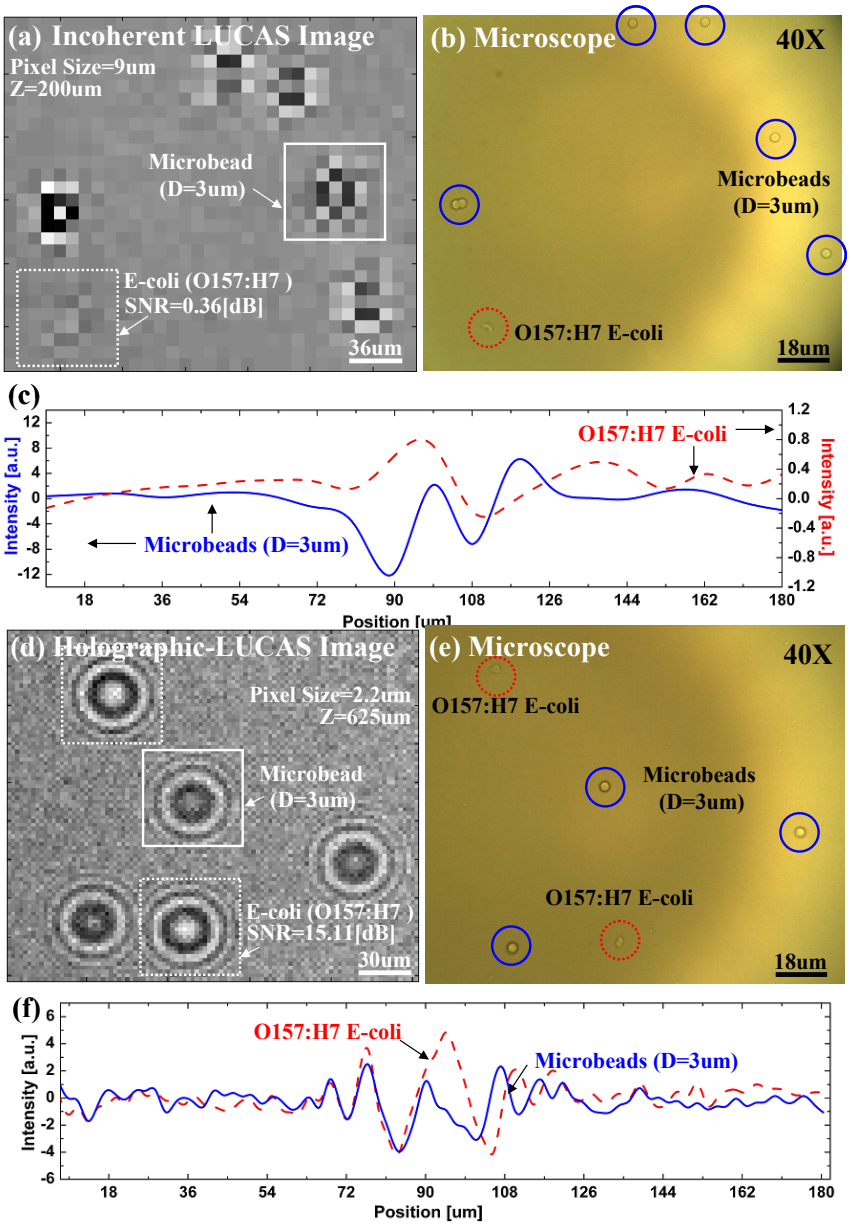

Figure 2-2 | (a) Conventional incoherent LUCAS image for a mixture of polystyrene micro-particles (D = 3µm) and *E. Coli* samples imaged with a 9 µm pixel size sensor array. (b) For comparison purposes, a microscope image of the same field of view that is acquired with a 40X objective-lens is also shown. (c) The cross sectional intensity profile (taken from (a)) of the classical diffraction pattern of a microbead and an *E. coli* sample is illustrated. (d) Holographic-LUCAS image of the same heterogeneous solution now exhibits much better signature uniformity. Furthermore, the weak diffraction pattern of the *E. coli* samples is now significantly improved with over 40 times SNR improvement. (e) For comparison purposes, a microscope image of the

same field of view that is acquired with a 40X objective-lens is also shown. (f) The cross sectional intensity profile (taken from (d)) of the holographic diffraction pattern of a microbead and an *E. Coli* sample is illustrated. Notice that the signal scale is different for the *E. coli* signature when compared to (c), which illustrates the improved performance of the Holographic-LUCAS platform for imaging weakly scattering phase objects such as small bacteria.

Another advantage of using the high-resolution Holographic-LUCAS platform is the on-chip detection of 2D orientation of asymmetric cells with a finer accuracy. One example is illustrated in Fig. 2-3 for yeast cells (*S. Pombe*), where the broken symmetry of the hologram uniquely determines the 2D orientation of each yeast cell on the chip. This performance would be greatly degraded with a coarser pixel size of e.g., ~9 µm since the fine details of the holographic pattern would mostly be smeared out.

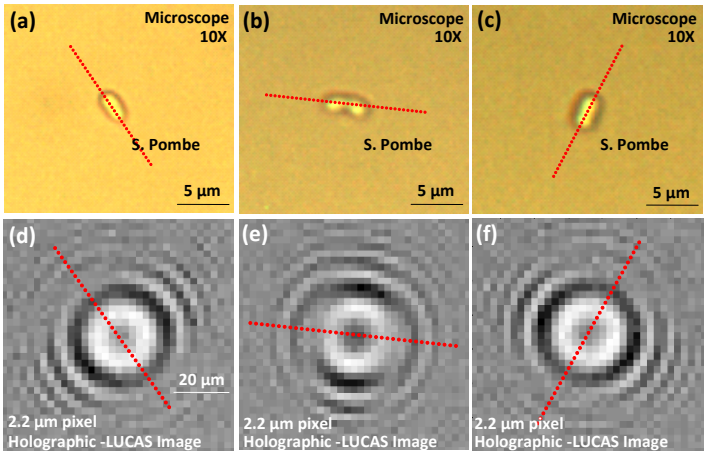

Figure 2-3 | Detection of 2D orientation of asymmetric cells using Holographic-LUCAS is illustrated. (a), (b), and (c) are the microscope images of *S. Pombe* yeast cells imaged under 10X objective-lens. (d), (e), and (f) show the corresponding Holographic-LUCAS images of the same field of view as in (a), (b), and (c), respectively. The orientation of each yeast cell can be uniquely determined by the broken symmetry as shown in the holographic-LUCAS images.

To better quantify the performance improvement of the high-resolution sensor array, I performed a series of characterization experiments with homogenous solutions containing 5, 10 and 20μm polystyrene beads. Statistical distribution of three major image parameters, *i.e. SNR*, R_{rms} and correlation index, are calculated for each particle type using 20 different samples. Figure 2-4 shows the performance summary of a large pixel size sensor (9.0μm) compared to a small pixel size sensor (2.2μm) for these three image metrics. In Figs. 2-4(a-b), *SNR* and R_{rms} distribution of three different sized particles, i.e., D=5, 10 and 20μm is shown with red triangles, green squares and blue circles, respectively. The performance of the large pixel size sensor array (Fig. 2-4(a)) reveals that there is significant overlap among the *SNR* and R_{rms} signatures of different sized particles, which may translate into possible characterization errors. Furthermore, Fig. 2-4(c) also plots the correlation index of these 3 different types of particles to their corresponding mean library images. Even though the correlation results of Fig. 2-4(c) reveal, as expected, three different groups that can be used for characterization decisions, the variation in the correlation index of the same particle type is relatively large, resulting in a large group size. On the other hand, the performance of the high-resolution sensor-array platform, as summarized in Figs. 2-4(b) and 2-4(d), shows significant improvement for characterization decisions. Both of these figures illustrate that the high-resolution sensor array can do a much better job to pick up the fine differences of the diffraction patterns corresponding to different particle types. As a result of this improved performance, the diffraction signature uniformity of each particle type is now much improved, yielding more reliable characterization decisions with distinct statistical groups for each image metric as shown in Figs. 2-4 (b) and 2-4 (d).

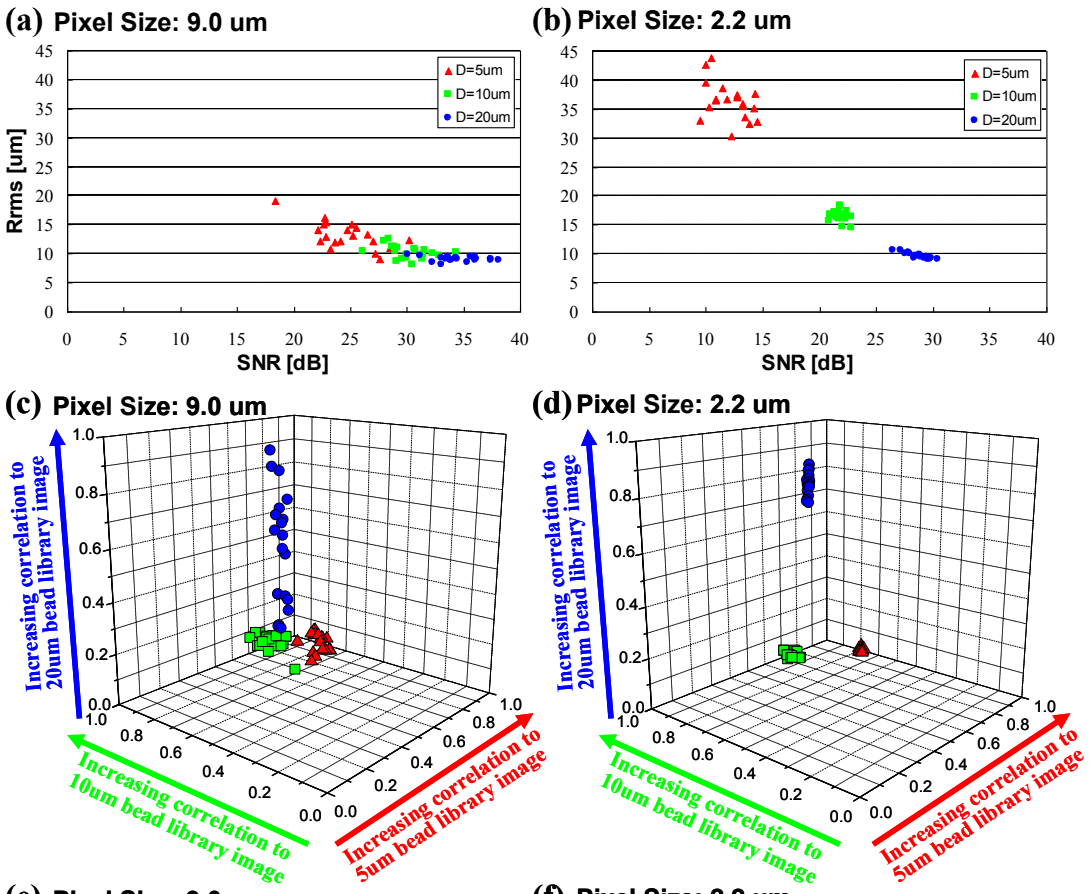

(e) Pixel Size: 9.0 um

Library	Target	Correlation Index		
		Ave.	Min	Max.
▲ 5 µm beads	5 µm	0.916	0.769	1.000
	10 µm	0.786	0.704	0.856
	20 µm	0.041	0.000	0.070
■ 10 µm beads	5 µm	0.746	0.695	0.834
	10 µm	0.915	0.731	1.000
	20 µm	0.063	0.000	0.107
● 20 µm beads	5 µm	0.064	0.000	0.145
	10 µm	0.244	0.163	0.357
	20 µm	0.715	0.489	1.000

(f) Pixel Size: 2.2 um

Library	Target	Correlation Index		
		Ave.	Min	Max.
▲ 5 µm beads	5 µm	0.985	0.953	1.000
	10 µm	0.784	0.766	0.795
	20 µm	0.010	0.000	0.025
■ 10 µm beads	5 µm	0.722	0.693	0.752
	10 µm	0.957	0.918	1.000
	20 µm	0.023	0.000	0.043
● 20 µm beads	5 µm	0.011	0.000	0.027
	10 µm	0.213	0.201	0.231
	20 µm	0.942	0.886	1.000

Figure 2-4 | The effects of the pixel size of the sensor array on the statistical distribution of various image metrics calculated for three different micro-particle types are shown. (a) 9 µm pixel size performance: SNR and Rrms map for 20 samples from each micro-particle type is shown. (b) same as (a) except for 2.2 µm pixel size sensor array. (c) 9 µm pixel size performance: The 3D correlation index map that is calculated using 20 samples from each micro-particle type is shown. (d) same as (c) except for 2.2 µm pixel size sensor array. The Tables in (e) and (f) briefly summarize the statistics of the correlation index results of (c) and (d), respectively. These results illustrate that the diffraction signature uniformity of each particle type is significantly improved

using a high-resolution sensor array, yielding more reliable characterization decisions with distinct statistical groups for each one of the image metrics.

Next I evaluated the performance improvement of the holographic on-chip system over the classical LUCAS platform using the same high-resolution sensor array. For this purpose, I imaged without using any lenses a heterogeneous solution that contained red blood cells (RBCs), yeast cells (*S. Pombe*), and 10μm polystyrene micro-particles, with and without a 100 μm pinhole to control the spatial coherence properties of the source. Figure 2-5 illustrates the significant differences between the holographic detection (Fig. 2-5(b)) vs. the conventional incoherent detection (Fig. 2-5(a)), both of which utilized the high-resolution sensor-array. As discussed earlier, with the pinhole, due to increased spatial coherence, the holographic diffraction pattern of each micro-object type exhibits much richer texture information with unique oscillating features containing the phase information of each cell/micro-particle. This phase information is normally lost during incoherent illumination as discussed in Chapter 3. Figures 2-5(c) and 2-5(d) also illustrate the cross-sectional profiles of the diffraction pattern of different objects under incoherent and coherent illuminations cases, respectively. These results, together with Figs. 2-5(e-j) clearly demonstrate that the holographic diffraction pattern of different cells/micro-particles are quite rich in 2D texture providing significant advantages when compared to conventional LUCAS systems[24–26] for lensless characterization and counting of a heterogeneous cell solution on a chip.

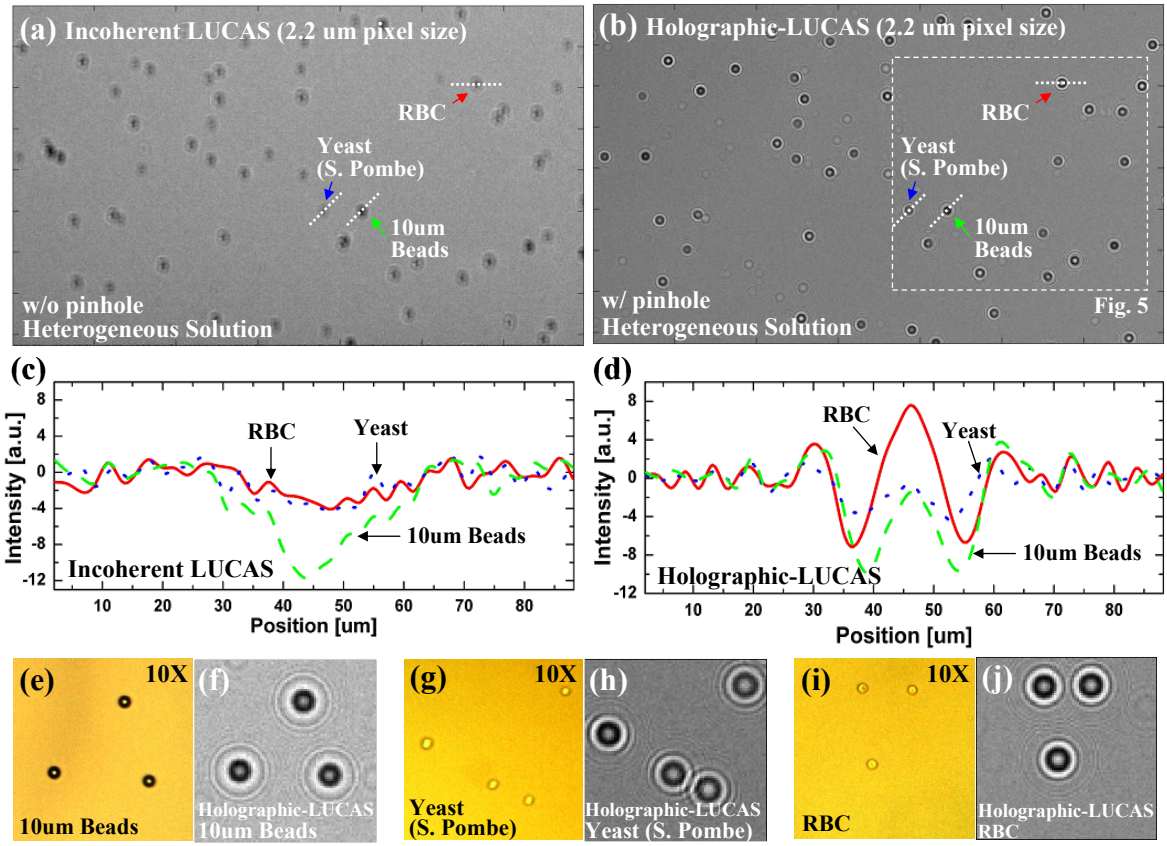

Figure 2-5 | (a) and (b) illustrate the performance differences between conventional LUCAS vs. Holographic-LUCAS. In each image a high-resolution CMOS sensor array (2.2 µm pixel size) was used. (c) and (d) show the cross sectional intensity profiles (taken from (a) and (b)) of various micro-objects imaged using conventional LUCAS and Holographic-LUCAS, respectively. Due to increased spatial coherence, the holographic diffraction pattern of each micro-object type exhibits much richer texture information with unique oscillating features containing phase information of the cell/micro-particle. This phase information is normally lost during incoherent illumination as discussed in the theory section of the article. (f,h,j) show zoomed images of the holographic diffraction signatures of 10um beads, yeast cells (S. Pombe) and RBCs, respectively. For comparison purposes, a microscope image of the same field of view that is acquired with a 10X objective-lens is also shown in (e,g,i).

To experimentally illustrate this last claim, Fig. 2-6 shows an example of automatic characterization of a heterogeneous solution including RBCs, fixed yeast cells (*S. Pombe*) and 10μm beads. These three types of micro-objects were individually identified within the acquired Holographic-LUCAS image by calculating their correlation to the mean library images of each type. The calculated *2D* correlation maps (see the Experimental Methods section) are illustrated in Figs. 2-6(b-d) for each one of the mean library images, exhibiting sharp correlation peaks for target cell/object types. In Fig. 2-6(a) which is taken from the white frame of Fig. 2-5(b), two 10μm beads, eight RBCs, and four yeast cells were successfully identified by the decision algorithm based on the 2D correlation maps shown in Figs. 2-6(b-d). These results demonstrate the proof-of-concept for on-chip characterization of a heterogeneous cell solution based on pattern recognition of the holographic diffraction pattern of each object type.

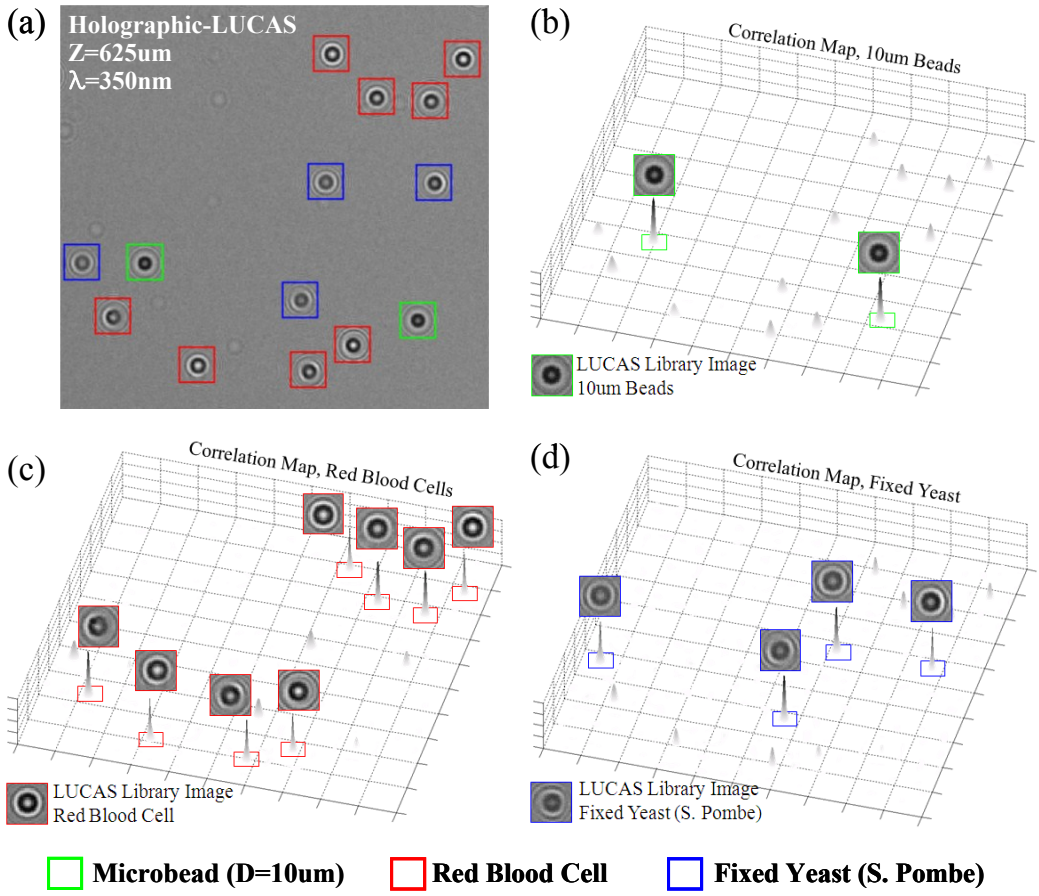

Figure 2-6 | (a) Automatic characterization of a heterogeneous solution of RBCs, Yeasts (S. Pombe) and 10 µm beads is illustrated using Holographic-LUCAS (λ=350nm). 2D correlation maps corresponding to each library image are also illustrated in (b-d), exhibiting sharp correlation peaks for the target cells/objects.

2.4 Discussions

As briefly outlined in the Introduction Section, the Holographic-LUCAS platform of this chapter exhibits several key differences when compared to pre-existing DIHM systems.[19,22,51] First, the detected holographic lensfree image is simply analyzed by a pattern recognition algorithm to classify different cell types on the chip. Note that this pattern recognition step is common to any other imaging based cytometry approach (including DIHM) once the image is captured or reconstructed, and therefore, it does not add an extra source of complexity and computation time

to the technique reported here. Therefore, numerically and computationally this approach is much simpler and faster when cell density is not a major concern.

Second, DIHM systems rely on near-perfect spatial coherence of the illumination source together with a large zero-order emission cone from the pinhole to achieve a high spatial resolution. That is the reason why in most DIHM systems a pinhole diameter of <2-3 μm is used. With my approach, these requirements are more relaxed since even with partially coherent illumination, the signature of different cells/micro-particles can exhibit uniquely different features enabling automated characterization of a cell solution using a pinhole diameter of ~100 μm (see the Results sections). This significantly larger diameter of the pinhole is quite important to increase the light throughput for illumination. For instance, in DIHM systems, usually a high magnification objective lens is utilized right in front of the pinhole to increase its transmission, which in my set-up is redundant, making it highly suitable for lensless on-chip miniaturization. This is especially significant to reduce the cost and the space requirement of a point-of-care on-chip cytometry system.

With my illumination scheme, for a pinhole diameter of 0.1 mm, using the van Cittert-Zernike Theorem,[56] one can estimate the diameter of *near-perfect* spatial coherence circle at the sensor-array plane as ~610λ. However, since Holographic-LUCAS is only concerned with the 2D texture of the cell holograms, it essentially also works for partially coherent illumination. This implies that the diameter within which I have a partial hologram of the cell is effectively larger than 610λ. I should note that one can utilize a smaller pinhole size to increase the diameter of this coherence circle at the detection plane. However, a smaller pinhole size will also increase the interference among neighboring cell holograms, which might reduce the pattern matching accuracy due to spatial overlap of the cell patterns. Therefore, a relatively large aperture size

such as 0.05-0.1mm does not only improve the light transmission efficiency without the use of any focusing optics, but also improves the accuracy of hologram classification.

2.5 Conclusion

In this chapter, I experimentally demonstrated the proof-of-concept of a lensfree holographic imaging platform, termed *Holographic-LUCAS,* for on-chip cytometry and diagnostics applications.[57] By controlling the spatial coherence of the illumination source, I recorded 2D holographic diffraction pattern of each cell/micro-particle on the chip using a high resolution sensor array. The recorded hologram was then processed by using a custom developed decision algorithm for matching the detected hologram texture to existing mean library images for on-chip characterization and counting of a heterogeneous solution of interest. When compared to existing on-chip systems, I verified significantly improved performance of this imaging approach by automatically characterizing heterogeneous solutions of red blood cells, yeast cells, *E. coli* and various sized micro-particles without the use any lenses or microscope objectives. This Holographic-LUCAS platform will especially be quite useful for point-of-care cytometry and diagnostics applications including e.g., infectious diseases such as HIV or malaria.

Chapter 3 Theory of Partially-Coherent In-Line Holography and Digital Iterative Phase Retrieval for Lensfree Microscopy

3.1 Partially-coherent in-line holography on a chip

Holography indirectly records the optical phase information through amplitude oscillations generated by the interference of coherent optical waves. For making use of this phase information toward microscopy, most existing lensless in-line holography systems require high level of spatial and temporal coherence and therefore utilize a laser source that is filtered through a small aperture, e.g., 1-2 μm wide.[11,58–66] The optical set-up, however, can be made simpler and more robust if a completely incoherent light source filtered through a large aperture (e.g., >100λ-200λ in diameter) could be used.[67,68]

One of the key steps for recording high-quality in-line holograms with a spatially incoherent source emanating from a large aperture is to bring the cell plane close to the detector array by ensuring $z_s << z_a$, where z_a defines the distance between the incoherently illuminated aperture plane and the object/cell plane, and z_s defines the distance between the object/cell plane and the sensor array (see Fig. 3-1), While the total aperture-to-detector distance (z_s+z_a) and the overall device length remain almost unchanged, conventional lensless in-line holography approaches typically choose to utilize $z_a << z_s$. Therefore, in addition to an incoherent source used with a large aperture, my choice of $z_s << z_a$ is also quite different from the main stream lensless in-line holographic imaging approaches.

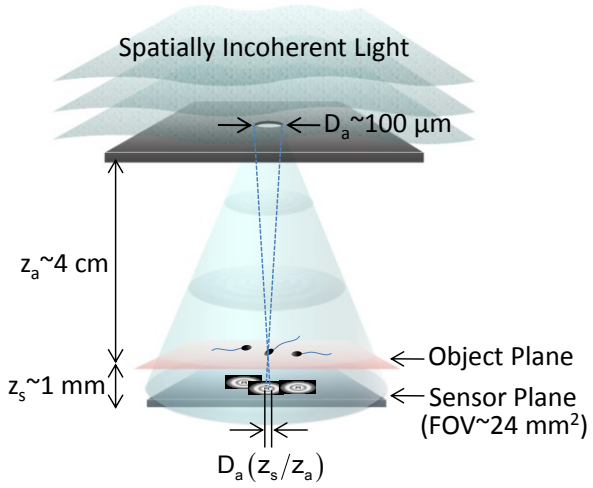

Figure 3-1 | Hologram formation of on-chip in-line holography with partially coherent illumination. The relative positions of the light source, the semen sample, and the sensor chip are depicted with typical distances. This schematic drawing is not drawn to scale.

To better quantify the impact of these differences on the detected holograms and their reconstructions, I assume two point scatterers (separated by 2a) located at the object/cell plane ($z=z_a$) with a field transmission of $t(x,y) = 1 + c_1\delta(x-a,y) + c_2\delta(x+a,y)$, where the intensities of c_1 and c_2 denote the strength of the scattering process for these two point-sources and $\delta(x,y)$ is a Dirac-delta function in space. Sub-cellular elements that make up a cell can be represented by such point scatterers. Let us further assume that there is a large aperture (of arbitrary shape) that is positioned at z=0 with a transmission function of $p(x,y)$ and that the digital recording device (e.g., a CMOS sensor array) is positioned at $z=z_a+z_s$, where typically z_a is 3-10 cm and z_s is 0.5-2 mm.

Assuming that a spatially incoherent light source uniformly illuminates the aperture $p(x,y)$, the cross-spectral density at the aperture plane can be written as

$$W(x_1,y_1,x_2,y_2,\nu) = S(\nu)p(x_1,y_1)\delta(x_1-x_2)\delta(y_1-y_2),$$

where (x_1, y_1) and (x_2, y_2) denotes two arbitrary points on the aperture plane and $S(\nu)$ represents the power spectrum of the incoherent source having its center frequency at ν_0 (corresponding to the center wavelength of λ_0). After propagating over a distance of z_a in free space, one can write the cross-spectral density at the object plane (just before interacting with the cells) as[27]

$$W(\Delta x, \Delta y, \eta, \nu) = \frac{S(\nu)}{(\lambda z_a)^2}\, e^{-j\frac{2\pi\nu q}{c z_a}} \iint p(x,y)\, e^{j\frac{2\pi}{\lambda z_a}(x\Delta x + y\Delta y)}\, dx\, dy,$$

where $\Delta x = x_1' - x_2'$, $\Delta y = y_1' - y_2'$, $\eta = \frac{x_1' + x_2'}{2}\Delta x + \frac{y_1' + y_2'}{2}\Delta y$, $\lambda = \frac{c}{\nu}$, c is the speed of light, and (x_1', y_1') (x_2', y_2') denotes two arbitrary points on the object plane. After interacting with the specimen, i.e., $t(x, y)$, the cross-spectral density right after the object plane can be written as

$$W(\Delta x, \Delta y, \eta, \nu) \cdot t^*(x_1', y_1') \cdot t(x_2', y_2').$$

Before reaching the detector plan, this cross-spectral density function will also propagate for another distance of z_s. Therefore, the cross-spectral density at the detector plane can be written as

$$W_D(x_{D1}, y_{D1}, x_{D2}, y_{D2}, \nu) = \iint \iint W(\Delta x, \Delta y, \eta, \nu)\; t^*(x_1', y_1')\; t(x_2', y_2')$$

$$h_C^*(x_1', x_{D1}, y_1', y_{D1}, \nu)\; h_C(x_2', x_{D2}, y_2', y_{D2}, \nu)\; dx_1'\; dy_1'\; dx_2'\; dy_2',$$

where (x_{D1}, y_{D1}) and (x_{D2}, y_{D2}) refer to two arbitrary points on the detector plane (within the hologram region of each cell) and $h_C(x', x_D, y', y_D, \nu) = \frac{1}{j\lambda\, z_s}\, e^{j\frac{2\pi z_s}{\lambda}}\, e^{j\frac{\pi}{\lambda\, z_s}[(x'-x_D)^2 + (y'-y_D)^2]}$.

At the sensor plane (x_D, y_D), one can then write the optical intensity $I(x_D, y_D)$ as

$$I(x_D, y_D) = \int W_D(x_D, y_D, x_D, y_D, \nu)\; d\nu.$$

Assuming $t(x, y) = 1 + c_1\delta(x - a, y) + c_2\delta(x + a, y)$, the optical intensity $I(x_D, y_D)$ can be further expanded into 4 terms, each with a different physical meaning, i.e.,

$$I(x_D, y_D) = I_S(x_D, y_D) + I_C(x_D, y_D) + H_1(x_D, y_D) + H_2(x_D, y_D)$$

where

$$I_S(x_D, y_D) = D_0 + \frac{|c_1|^2 S_0}{(\lambda_0 z_a z_s)^2}\tilde{P}(0,0) + \frac{|c_2|^2 S_0}{(\lambda_0 z_a z_s)^2}\tilde{P}(0,0) \tag{3-1}$$

$$I_C(x_D, y_D) = \frac{c_2 {c_1}^* S_0}{(\lambda_0 z_a z_s)^2}\tilde{P}\left(\frac{2a}{\lambda_0 z_a}, 0\right) e^{j\frac{4\pi a\, x_D}{\lambda_0 z_s}} + c.c. \tag{3-2}$$

$$H_1(x_D, y_D) = \frac{S_0}{(\lambda_0 z_a)^2}[c_1 \cdot \{p(-x_D \cdot M + a \cdot M \cdot F, -y_D \cdot M) * h_c(x_D, y_D)\} + \ c.c.] \tag{3-3}$$

$$H_2(x_D, y_D) = \frac{S_0}{(\lambda_0 z_a)^2}[c_2 \cdot \{p(-x_D \cdot M - a \cdot M \cdot F, -y_D \cdot M) * h_c(x_D, y_D)\} + \ c.c.] \tag{3-4}$$

where "c.c." and "$*$" denote the complex conjugate and convolution operations respectively, $M = \frac{z_a}{z_s}$, $F = \frac{z_a + z_s}{z_a}$, and $\tilde{P}$ is the 2D spatial Fourier Transform of the arbitrary aperture function $p(x, y)$. It should be emphasized that (x_D, y_D) in these equations is restricted to the extent of the cell/object hologram, rather than extended to the entire field-of-view of the detector array. Furthermore, $h_c(x_D, y_D) = \frac{1}{j\,\lambda_0 \cdot F \cdot z_s} e^{j\frac{\pi}{\lambda_0 \cdot F \cdot z_s}({x_D}^2 + {y_D}^2)}$ and it represents the 2D coherent impulse response of free space over a distance of $\Delta z = F \cdot z_s$. For the incoherent illumination source, I have assumed that the spectral bandwidth is much smaller than its center frequency ν_0, i.e., $S(\nu) \cong S_0 \delta(\nu - \nu_0)$. This is an appropriate assumption since the light sources (LEDs) that I have typically used in my experiments have their central wavelengths at 500-650 nm with a spectral FWHM of 10-15 nm.

In these derivations, paraxial approximation has also been assumed to simplify the results since z_a and z_s for my hologram recording geometry are typically much longer than the extent of each cell hologram. However, such an approximation was not used in the numerical reconstruction process of the cell images, which will be further discussed later on in this chapter. D_0 in Eq. (3-1) can further be expanded into

$$D_0 = \iint \iint \int \frac{W(\Delta x, \Delta y, \eta, \nu)}{(\lambda\, z_s)^2}\, e^{-j\frac{\pi}{\lambda z_s}[(x_1' - x_D)^2 + (y_1' - y_D)^2]} e^{j\frac{\pi}{\lambda z_s}[(x_2' - x_D)^2 + (y_2' - y_D)^2]} dx_1'\, dy_1'\, dx_2'\, dy_2' d\nu,$$

which physically represents the background illumination reaching the sensor plane and carries no spatial information regarding the cells' structure or distribution. For typical illumination configurations, D_0 constitutes a uniform or slowly-varying background, and hence can be digitally subtracted out without an issue.

Eqs. (3-1)-(3-4) are rather important to explain the key parameters in my partially-coherent lensless on-chip holography scheme utilizing an incoherent light source emanating through a large aperture. Eq. (3-1) includes the background illumination (D_0 term) and the self-interference of the scattered waves (the terms that are proportional to $|c_1|^2$ and $|c_2|^2$), both of which represent the classical diffraction that occurs between the object and the sensor planes under the paraxial approximation. Note also that these self interference terms in Eq. (3-1) are scaled with $\tilde{P}(0,0)$ as the physical extent of the spatial coherence at the cell plane is not a determining factor for self interference.

Eq. (3-2), on the other hand, represents the interference between these two scatterers located at the object plane. Just like self-interference, the cross-interference term, $I_C(x_D, y_D)$, is also not useful for holographic reconstruction of object images. Since this cross-interference term is proportional to the amplitude of $\tilde{P}\left(\frac{2a}{\lambda_0 z_a}, 0\right)$, two scatterers that are far from each other can still interfere effectively if a small aperture size is used (hence wide $\tilde{P}$). The $\tilde{P}\left(\frac{2a}{\lambda_0 z_a}, 0\right)$ term predicts that, if $2a < \frac{\lambda_0 z_a}{D_a}$ (where D_a is the aperture width), the cross-interference $I_C(x_D, y_D)$ from these two scattered fields will generate strong but undesired cross-interference patterns at the sensor plane. This conclusion is also supported by the fact that the coherence diameter at the object plane is on the order of $\sim\frac{\lambda_0 z_a}{D_a}$, as estimated by van Cittert-Zernike theorem. Therefore, as another advantage of using a large aperture that is illuminated by an incoherent light source, this

cross-interference noise term, $I_C(x_D, y_D)$, will only contain the contributions of a limited number of cells within the imaging field-of-view since the extent of $\tilde{P}\left(\frac{2a}{\lambda_0 z_a}, 0\right)$ will be suppressed by a large aperture. Therefore, incoherent illumination through a large aperture will provide better image quality for characterizing dense cell suspensions such as undiluted semen samples.

The final two terms (Eqs. (3-3) and (3-4)) represent the holographic diffraction patterns in the recorded intensity and are the foci of all digital holographic imaging systems, including the on-chip implementation discussed in this chapter. Ideally, these terms should dominate the information content of the recorded intensity, which is typically true for weakly scattering objects. More specifically, $H_1(x_D, y_D)$ is the holographic diffraction of the first scatterer $c_1\delta(x-a, y)$; and $H_2(x_D, y_D)$ is the holographic diffraction of the second scatterer $c_2\delta(x+a, y)$. Since ${h_c}^*(x_D, y_D)$ creates twin image artifacts at the reconstruction plane when propagated in the reverse direction, the complex conjugate (c.c.) terms in Eqs. (3-3) and (3-4) represent the source of the twin images. Numerical elimination of these twin image artifacts will be discussed in Section 3.2.

As indicated by the terms inside the curly brackets in Eqs. (3-4), a scaled and shifted version of the aperture function $p(x, y)$ coherently diffracts around the position of each scatterer. In other words, each point scatterer projects a scaled version of the aperture function (i.e., $p(-x_D \cdot M, -y_D \cdot M)$) to a location shifted by F folds from origin, and the distance between the object plane and the sensor plane is now also scaled by F folds (ie., $\Delta z = F \cdot z_s$). It is also important to emphasize that the aperture size is effectively narrowed down by M fold at the object plane. For $M >> 1$ (typically 50-200), a spatially-incoherent light source through a large aperture can still provide coherent illumination to each cell individually for generating each cell's holographic signature on the sensor plane. This is true as long as the cell's diffraction pattern is smaller than

the coherence diameter at the sensor plane. In my geometry, coherence diameter is typically $500\lambda_0 - 1000\lambda_0$ and it is much larger than the practical width of cell holograms on the sensor plane, which is easy to satisfy especially for small z_s values. Consequently, for a completely incoherent source emanating through an aperture width of D_a and illuminating a sensor area of A, the effective width of each point scatterer diffracting toward the sensor plane would be D_a/M and the effective imaging field-of-view, FOV, would be A/F^2. Considering typical values for z_a (e.g., 3-10 cm) and z_s (0.5-2mm), the scaling factor (M) becomes >100 and $F \approx 1$, as a result of which even a 50 μm wide pinhole would be scaled down to <500 nm and the entire active area of the sensor array now can be used as the imaging field-of-view (i.e., $FOV \approx A$).

Although the entire derivation above is based on the formalism of wave theory, the final result is also matched to a scaling factor of $M = \frac{z_a}{z_s}$ (see Figure 3-1) predicted by simple geometrical optics. In the case of M>>1 with partially coherent illumination, each cell hologram only occupies a tiny fraction of the entire field-of-view and has little cross-talk with other cell holograms. As a result, unlike conventional lensless in-line holography, there is no longer an overall Fourier transform relationship between the sensor plane and the object plane. Such a spatial Fourier transform relationship exists only between each individual hologram and its corresponding cell.

According to Eqs. (3-4), a narrow enough $p(-x_D\, M, -y_D\, M)$ can ensure that the spatial features of the cells are not being washed out by partially-coherent illumination through a large aperture, as a result of which the modulation of the holographic term at the detector plane to be approximated as $sin\left(\frac{\pi}{\lambda_0\, F\, z_s}({x_D}^2 + {y_D}^2)\right)$. Such a modulation term suggests that a large fringe magnification (F) allows the use of a larger pixel size of the sensor array for recording the holographic fringes of the objects and effectively increases the numerical aperture of hologram

recording, which is then only limited by the sensor width. There are, however, also disadvantages for having a large F: (1) a coherent light source emanating through a small aperture is needed to provide high spatial coherence at the sensor plane, which results in a more complicated set-up in terms of alignment of optical components, increasing the overall cost and complexity of the imaging platform; and (2) the effective imaging field-of-view is also reduced by a factor of F^2.

3.2 Digital iterative phase retrieval process and reconstruction of microscopic images

In partially-coherent lensless on-chip holography with $M \gg 1$ since the incident wave on each cell has very small curvature in its wavefront, the recorded cell holograms can be reconstructed assuming plane-wave illumination. To propagate the wavefronts, an angular spectrum approach is used for numerically solving the Rayleigh-Sommerfeld integral. Within a linear and isotropic medium, this calculation can be done by multiplying the Fourier transform of the incident field with a transfer function defining this propagation, i.e.,:

$$H_z(f_x, f_y) = \begin{cases} \exp\left(j2\pi z \frac{n}{\lambda}\right)\sqrt{1-\left(\frac{\lambda f_x}{n}\right)^2-\left(\frac{\lambda f_y}{n}\right)^2}, & \sqrt{{f_x}^2+{f_y}^2} < \frac{n}{\lambda} \\ 0, & otherwise \end{cases}$$

where f_x and f_y are the spatial frequencies along x and y, respectively, and n is the refractive index of the medium.

Among various reconstruction methods used in digital holography literature,[18–22,51,69–72] a simple yet effective phase-retrieval approach is chosen to reconstruct the microscopic images of cells (for both the amplitude and phase profiles) and eliminate the twin-image artifacts introduced by my in-line hologram recording geometry.[67,70] With a finite support constraint defined around each object, this technique can iteratively recover the phase of the diffracted field from a single intensity image recorded by the sensor array. As a result, the complete complex

field (both the amplitude and phase components) of the cell holograms can be back-propagated to the sample plane for reconstruction of the object's image without twin-image contamination. This numerical method can be summarized as follows:

a) In the first iteration, the intensity of the recorded hologram is propagated back to the object plane by a distance of $-z_s$, assuming zero as the initial phase value for the complex field. Object support, S, is defined for each object either by thresholding the field amplitude at the object plane, or by finding its local maxima/minima.

b) For the complex field at the object plane, $U^i_{-z_s}(x,y)$, the values outside the object support are substituted with a background value $D_{-z_s}(x,y)$, and the field inside the object support remains unchanged, i.e.,

$$U^i_{-z_s}(x,y) = \begin{cases} m \cdot D_{-z_s}(x,y), & x,y \notin S \\ U^{i-1}_{-z_s}(x,y)\ , & x,y \in S \end{cases}$$

where $D_{-z_s}(x,y)$ is generated by back-propagating the square root of the background image (obtained in the absence of the objects) and $m = mean(U^{i-1}_{-z_s}(x,y))/mean(D_{-z_2}(x,y))$ is a normalization factor.

c) The modified field at the object plane is then propagated forward to the sensor plane, on which the updated phase of the sensor plane field remains unchanged but the amplitude is replaced with the square root of the original recorded hologram intensity. In other words, the measured amplitude of the sensor plane field will be kept constant throughout these iterations to ensure convergence of the phase. Accordingly, the complex diffraction field at the sensor plane after the ith iteration, $U^{(i)}_0(x,y)$, can be written as

$$U^{(i)}_0(x,y) = \left|U^{(0)}_0(x,y)\right| \cdot \exp(\emptyset^{(i)}_0(x,y))$$

where the superscripts refer to the iteration step, and $\emptyset_0^{(i)}(x,y)$ denotes the phase of the field at sensor plane after the ith iteration. After this modification, the sensor plane complex field is again propagated backward to the object plane to get the updated object field.

By iterating between steps b and c, the phase values of the sensor field typically converge within 15-20 iterations. Once converged, the complex field is propagated backward to the object plane as the final output of the microscopic cell images containing both amplitude and phase profiles.

3.3 Experimental demonstration of lensfree on-chip microscopy

The efficacy of the presented computational lensfree microscopy approach has been tested by identifying and counting various cell types in human blood on a chip.[73]

First the cytometry performance of this lensfree approach was quantified by imaging whole blood samples at various dilution levels and was compared to the texture matching approach introduced in Chapter 2. Fig. 3-2(a) illustrates the lens-free red blood cell (RBC) hologram amplitudes, as well as their reconstructed images for various cell density levels, which clearly indicate the strength of the digital holographic reconstruction to handle highly dense cell solutions. Considering the highest concentration in Fig. 3-2(a), where all of the lens-free RBC holograms are completely overlapping (because of a high cell density of ~400,000 cells/μL), using the complementary information of the reconstructed cell images, one can individually separate the 2D holographic signature (both phase and amplitude) of any given cell within the hologram crowd. This duality between cell hologram texture and the digitally reconstructed cell images is especially useful for characterization of dense cell solutions such as whole blood samples.

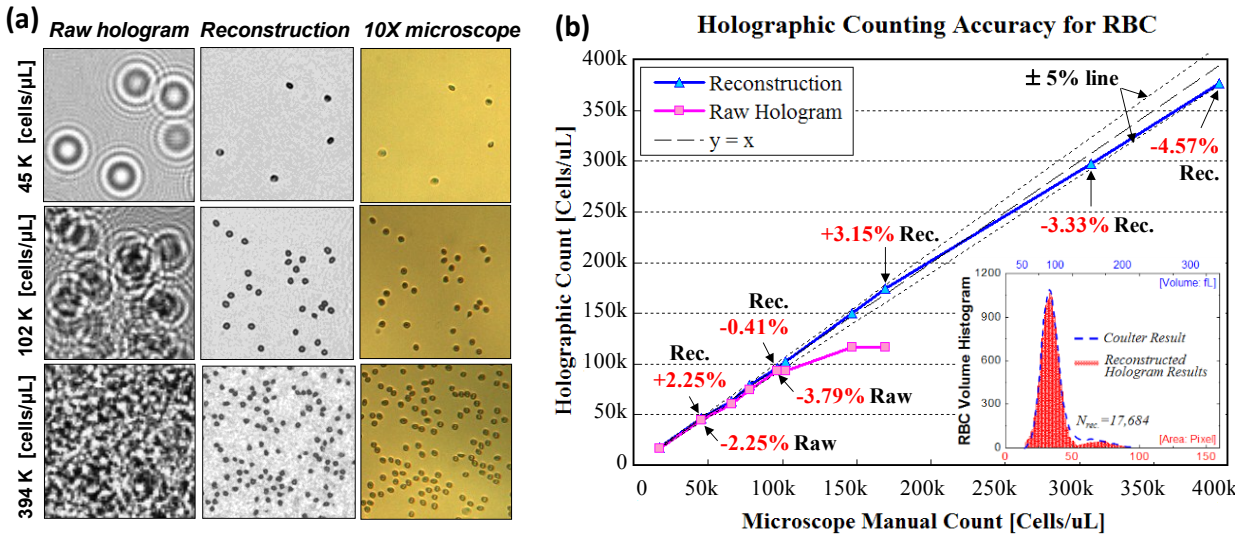

Figure 3-2 | (a) Raw holograms, digital reconstructions, and microscope images of whole human blood sample with various concentrations are shown. More than 90% of the cells are red blood cells (RBC). (b) Automated counting accuracy of the proposed incoherent cell holography method is illustrated at various RBC densities ranging from ~20,000 cells/µL up to ~400,000 cells/µL. Cell counting with 2D texture of raw cell holograms starts to lose its accuracy for densities beyond 100,000 cells/µL. The inset in (b) also illustrates a verification of RBC volume histogram that is estimated based on holographic reconstructions with a commercially available hematology analyzer.

In addition, for each dilution level, the density of RBCs based was measured on automated counting of digitally reconstructed cell images. The counting results Fig. 3-2(b) revealed that the reconstructed cell images yielded an absolute error rate of ~5%, up to a cell density of ~400,000 cells/µL, when compared to counting results of the same FOV obtained using a conventional lens-based microscope.

To further validate the holographic characterization results, the inset in Fig. 3-2(b) also illustrates a comparison of RBC volume histogram that is estimated based on the same digital reconstructions against a commercially available Coulter counter (Coulter LH750, Beckman Coulter), which showed a good fit to the results. In these cell volume calculations, it was

assumed that RBCs are phase-only objects with an average refractive index of ~1.4. Under these assumptions, the thickness of each RBC becomes proportional to its recovered and unwrapped optical phase, and the base area of each RBC can be estimated by simple thresholding of the recovered phase images. The cell volume of each RBC was then estimated by the product of its thickness and base area.

Lastly, the sub-cellular structure resolving capability of the presented lensfree microscopy approach was tested on blood smear samples that are prepared in accordance with conventional staining protocols.[73] Figure 3-3 illustrates the holographic imaging results of these blood smear samples, focusing specifically on the holographic signatures (both amplitude and phase) and the reconstructed microscopic images of various blood cells such as granulocytes, lymphocytes, monocytes, and platelets. These results, and their comparison to 40x□objective-lens microscope images (NA~0.6), indicate that the reconstructed holographic images can be used to discriminate sub-cellular differences among three major types of white blood cells (WBC) (i.e., granulocytes, lymphocytes, and monocytes), and have the potential to provide three-part differential WBC analysis within the same lensfree digital platform. Note also that some of the platelets in these images are located at a different depth of field than the WBC, which is why they do not appear in some of the reconstructed images.

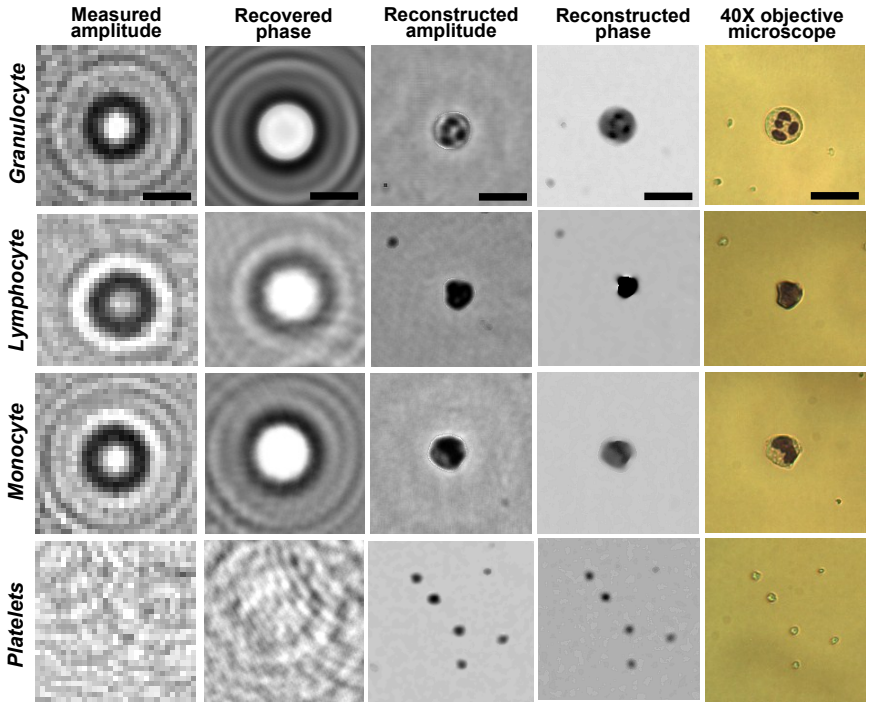

Figure 3-3 | Holographic imaging results of a blood smear sample, illustrating the lensfree shadow signatures of three major types of white blood cells (i.e., *granulocytes, lymphocytes and monocytes*) and *platelets*. Different than Fig. 8, these stained cells are imaged in a dry smear condition. Through iterative holographic processing, the lost phase information of each cell hologram is recovered (second column), which then leads to reconstruction of amplitude and phase images of the cells (3rd and 4th columns on the right). The same field of view in each case is also imaged using a 40X objective lens (NA=0.6) for comparison purposes (the 5th column on the right). Scale bars, 20μm.

According to the results presented here and in the related publication,[67,73] it can be concluded that such a computational lensfree microscopy approach can achieve a spatial resolution of 1-2 μm (NA~0.2) in a very compact and cost-effective setting, which can be very valuable for analyzing the micro-organisms that are involved in pandemic diseases in resource-limited areas, such as HIV, malaria, or infectious diarrhea.

3.4 Conclusion

In this chapter, I reviewed the fundamental principles of on-chip in-line holography with partially coherent illumination as well as the techniques that are used to reconstruct the microscopic amplitude and phase images of the micro-objects or cells. Through experiments with whole human blood, I demonstrated that this lensless imaging approach can reconstruct their microscopic amplitude and phase images with a resolution of 1-2 μm for accurate characterizing cells at densities up to 0.4 million cells/μL. With resolution and sensitivity that can differentiate between various white blood cell sub-types such as granulocytes, monocytes and lymphocytes, such lensless on-chip holography technology will be especially useful for point-of-care cytometry and diagnostics applications involving global health problems such as HIV,[74] malaria,[75] or infectious diarrhea.[76]

Chapter 4 Compact and Light-Weight Automated Semen Analysis Platform Using Lensfree on-Chip Microscopy

4.1 Introduction

Semen analysis is an important routine that is extensively practiced in laboratories for evaluating male fertility[77] and preparing artificial insemination.[78] To determine the sperm concentration in semen, visual assessment by putting the sample into a counting chamber and then manually counting the sperms through an optical microscope is still the gold standard. Not only that this method is recommended by the World Health Organization (WHO), but also it is widely used in most laboratories that process semen.[79] Due to the labor intensive nature of this manual method, several other optical approaches, including turbidimetry,[80,81,82,83,84,85,86,87] laser Doppler velocimetry,[88,89,90,91,92,93] and photon correlation spectroscopy,[94,95,96] have also been proposed to automatically analyze semen. However, these approaches are still not widely adopted partially because they can only provide indirect estimations of the sperm concentration and motility.

Currently, Computer-Assisted Semen Analysis (CASA) systems,[97–103] which utilize pattern analysis algorithms to automatically process the images recorded with a conventional optical microscope, is considered as one of the most promising technologies to replace the traditional manual semen analysis method. An important feature of CASA systems is their ability to provide quantitative information about sperm motility, such as the speed distribution of individual sperms, which has been proven to be rather important for predicting fertilization rate[104,105] as well as for evaluation of the correlation between various drugs and sperm quality.[106,107] However, despite the fact that state-of-the-art CASA systems are very efficient and versatile, their relatively large dimensions, high cost and maintenance needs partially hinder their wide-spread

use in fertility clinics. For the same reason, application of this platform to field-use in veterinary medicine such as stud farming and animal breeding[108,109,110] has also been significantly limited.

In addition to these, commercially available male fertility test kits for personal home use, such as FertilMARQ[111] or SpermCheck,[112] also aim to indirectly quantify sperm concentration by a color change due to chemical staining or labeling of sperm-specific proteins. These tests, however, cannot quantify sperm motility or the concentration of motile sperms. Recently, an alternative semen analysis platform involving a compact micro-fluidic device that can measure electrical impedance changes due to sperm movement has also been reported.[113] However, this lab-on-a-chip platform can only provide the total number of the sperms in the sample and cannot differentiate motile and immotile sperms from each other, which is an important limitation.

In this chapter, as an alternative approach, I present a compact and light-weight platform to conduct automated semen analysis on a chip. At the core of my technology lies a lensfree holographic on-chip microscope (see Fig. 4-1) which weighs ~46 grams and measures ~ 4.2 × 4.2 × 5.8 cm providing an imaging field-of-view (FOV) of ~24 mm^2 together with an effective numerical aperture (NA) of ~0.2.[67] This imaging FOV is more than 20 fold larger than the FOV of a typical 10X objective-lens, and therefore provides a significant throughput advancement that permits automated monitoring of hundreds to thousands of sperms all in parallel. This lensfree on-chip microscope is based on digital in-line holography, and it utilizes an incoherent or partially coherent light source (such as a light emitting diode - LED) that is filtered by a large aperture of ~0.1mm to illuminate the sample of interest as illustrated in Fig. 4-1. Over a short propagation distance of ~4 cm, this illumination light picks up partial spatial coherence, after which it scatters from each sperm to coherently interfere with the background light, forming lensfree holograms of the sperms over a large FOV (~24 mm^2). These lensfree sperm holograms

can then be rapidly processed (e.g., <1 sec) using a Graphics Processing Unit (GPU) to reconstruct their microscopic images (both amplitude and phase[67]) as illustrated in Fig. 2.

To conduct automated semen analysis using this lensfree holographic microscope (Fig. 4-1), I captured ~20 holographic frames over ~10 seconds for each semen sample. Quite conveniently, digital summation of all these lensfree frames removed the moving sperms out of the picture and enabled the platform to rapidly count only the immobile sperms based on the reconstructed phase images. On the other hand, digital subtraction of these consecutive holographic frames from each other this time removed the immobile sperms out of the picture, leaving behind only the moving ones, which permits automatic quantification of the individual speed and the trajectories of all the motile sperms within an FOV of ~24 mm^2. I also validated the performance of this platform for automated semen analysis by comparing my results against manual analysis of the same samples conducted using a conventional bright-field microscope.

Figure 4-1 | A lensfree holographic on-chip microscope that measures 4.2×4.2×5.8 cm and weighs 46 grams is shown. The embedded light source (an LED filtered by a pinhole) and the CMOS image sensor are both powered through a USB connection from the side. This compact on-chip microscope can provide both

amplitude and phase images of the sperms (loaded within a sliding tray) over a field-of-view of 24 mm2 with an effective numerical aperture of ~0.2.

I believe that such a compact, light-weight and cost-effective automated semen analysis platform running on a wide-field lensfree on-chip microscope would be especially useful for fertility clinics, personal male fertility tests, as well as for field-use in veterinary medicine.

4.2 Experimental Methods

Lensfree holographic on-chip microscope: A self-contained on-chip microscope (see Fig. 4-1) is designed to record the holographic images of the semen samples over a field-of-view of ~24 mm^2 with an effective NA of ~0.2 without utilizing any lenses or scanning mechanical components.[67] This entire lensfree on-chip microscope assembly weighs ~46 grams and measures ~ 4.2 cm × 4.2 cm × 5.8 cm. Inside this on-chip microscope, a simple light-emitting diode (LS E67B, OSRAM Opto Semiconductors, center wavelength: 645 nm, bandwidth: ~15 nm) is filtered by a 0.1 mm pinhole to provide partially coherent illumination over the semen sample that is placed at a distance of ~4 cm from the source. Lensfree holograms of the sperms are recorded by a monochrome CMOS image sensor (MT9P031STM, Aptina Imaging, 2.2 μm pixel size, 5 megapixel, 24 mm^2 active area). This entire imaging system, including the light source and the sensor-chip, is powered and controlled by a laptop computer through a USB 2.0 connection. A smart-phone or a personal digital assistant (PDA) could also be used for the same purpose. The sample of interest is loaded into this microscope using a sliding tray and held at ~1 mm above the active area of the CMOS image sensor.

Sample preparation: Frozen semen specimens were obtained from California Cyrobank and were stored in liquid nitrogen. Before use, the specimen vials were thawed in 37°C water bath for 10 minutes to revive the sperms. A sperm washing medium (9983, Irvine Scientific), pre-

mixed with a small number of 20 μm polystyrene microspheres (4220A, Thermo Scientific, ~40 beads/μL), was used to dilute the semen sample to a desired concentration. The diluted semen was pipetted into a glass sperm counting chamber (DRM-600, Millennium Sciences, chamber depth: 20 μm) and then enclosed with a No. 1 glass cover slip (12-548A, Fisher Scientific) to suppress liquid evaporation. The added microspheres act as mechanical spacers to ensure a constant chamber height and a uniform sperm distribution. For preparing semen samples with immobilized sperms, the diluent was replaced by a bicarbonate-formalin diluting fluid (6710-4, Ricca Chemical) while the rest of the procedures remained the same.

Hologram recording and automated sperm analysis: 20 consecutive lensfree holographic frames for each semen sample of interest were recorded using the on-chip microscope shown in Fig. 4-1 at a frame rate of 2 frames per second (FPS) and an integration time of ~35 milliseconds per frame. Two different processing approaches, digital summation and subtraction of these lensfree holographic frames, were applied to separately identify and quantify the immotile and the motile sperms in the semen sample.

For identification and quantification of the immotile sperms, all the individual holographic images were normalized to their own mean intensity and then were summed up digitally. This summation operation not only increases the digital signal-to-noise ratio (SNR) of the immotile sperms' holograms, but also smears out the lensfree holograms of the motile sperms. As a result, this step creates sufficient contrast and SNR to observe the faint images of the sperms' tails, which enables automated identification of their signatures from the background (see e.g., Fig. 4-2).

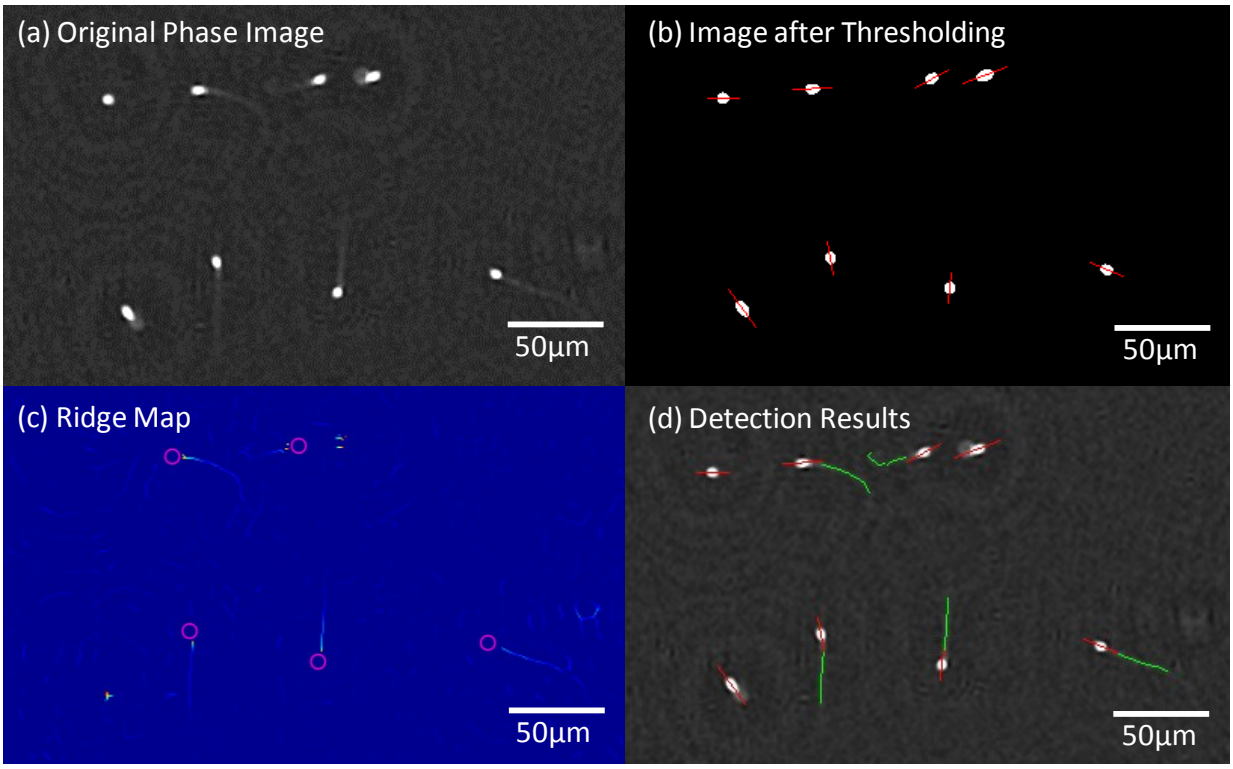

Figure 4-2 | (a) The reconstructed phase image contains 8 sperms with different morphologies and orientations. (b) A new image was digitally generated by thresholding the intensity of the image shown in (a) to highlight the position and the orientation of each sperm head. The red lines indicate the orientations (i.e., the major axis) of the elliptical sperm heads. (c) A ridge map of the original phase image shown in (a) was generated using a determinant-of-Hessian filter. Positions of the sperm heads in this image are marked with red circles. (d) By matching the orientation of each sperm head (red lines in (b)) with the orientation of the sperm tails (labeled by green curves in (d)), viable sperms within the sample were automatically identified.

Next, an iterative holographic reconstruction algorithm[67] was used to process this summation hologram and reconstruct the microscopic images (containing both amplitude and phase information, see e.g., Figs. 4-3(c-d) and 4-4(b-c)) of the immotile sperms. Towards automated counting of immotile sperms, candidate objects were initially screened by their distinct and bright elliptical heads in the reconstructed phase images (see e.g., Fig. 4-2(d)). These immotile sperm candidates were isolated from the background through a threshold operation, where pixels

above a certain intensity value were grouped together. After this thresholding step, several digital properties of each connected region were calculated such as its pixel area, orientation, and a coefficient indicating the object circularity.[57] Thresholded regions of invalid size or shape were discarded, and a line was fitted to match the orientation and the length of the fitted ellipse to each sperm head (shown with red colored lines in Fig. 4-2(b)). Following this initial screening step, the tail of each sperm must also be identified and matched to its corresponding sperm head orientation. The condition for a viable sperm is the presence of a healthy tail (in accordance with the WHO laboratory manual[79]); and therefore for a positive count, the tail must have an adequate length that is also aligned with the orientation of the sperm head. Towards this end, for digital enhancement of the contrast of each tail in the reconstructed phase image, a determinant-of-Hessian filter[114] was applied to extract the ridge-like features of each individual sperm tail (see Fig. 4-2(c)). A threshold was then applied to the resulting image after which the tails were identified by searching for the remaining ridges in the neighborhood of the endpoints of each head orientation line (i.e., by matching the green and red lines as shown in Fig. 4-2(d)). If a ridge is absent from this sperm head neighborhood, or if the tail is not long enough, or has an abnormal shape it was discarded. All the valid sperms were then automatically counted and marked in the image for further comparison, if necessary.

Quantification of the motile sperms in semen is a relatively easier task for my technique since the only moving objects within the sample are the motile sperms. For this purpose, consecutive lensfree holographic frames were digitally subtracted from each other to create new digital holograms (see e.g., Fig. 4-3(a)) that represent differential motion of the sperms. The same iterative algorithm[67] discussed above was then used to reconstruct the differential motion of the motile sperms as shown in Fig. 4-3(b). In these reconstructed holographic images, the

motion of each sperm generates one negative (dark) and one positive (bright) spot, which indicate the start and the end positions of the sperm's motion, respectively. Therefore, by quantifying the relative distance between these bright and dark spots I can simultaneously infer the speed and the trajectories of all the motile sperms within my imaging field-of-view (~24 mm^2). For this purpose, the locations of these spots were identified by simple thresholding followed by calculation of their centroid positions.[115] As a result of this, the displacements of individual sperms between consecutive holographic frames can be easily calculated by using the shortest distance between the centroid positions of each dark-bright spot pair (see e.g., Fig. 4-3(b)). These displacements of motile sperms in all consecutive frames were then linked to each other to plot the dynamic trajectories of the sperms within my FOV (see e.g., Fig. 4-4(a)). The average speed of each motile sperm was calculated by summing up the magnitudes of its displacements in all frames and dividing this sum with the total duration of the frame acquisition.

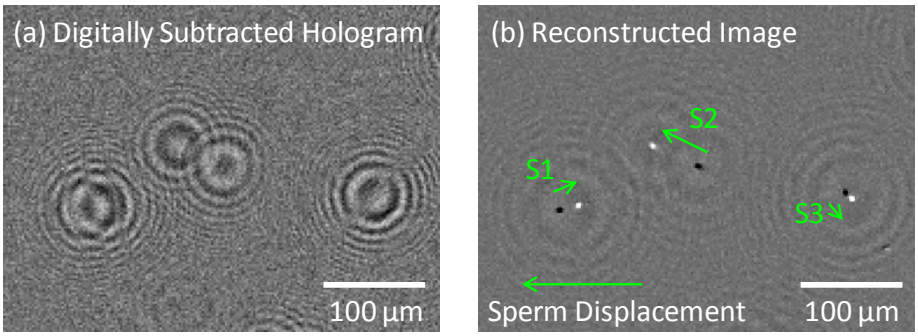

Figure 4-3 | (a) A digitally subtracted lensfree hologram of three moving sperms is generated from two successive frames (500 milliseconds apart) (b) A microscopic image, that is digitally reconstructed from the lensfree differential hologram shown in (a), illustrates the positions of three sperms in two successive frames (white spots show the sperms' end positions and black spots show their starting positions). The displacement vectors of these sperms are labeled as S1, S2, and S3.

Digital processing of the acquired lensfree holographic images, including both immotile sperm detection and motile sperm tracking, were implemented in Matlab. The computation time for each semen sample was ~15 min for ~24mm^2 FOV using a PC with an Intel Core2Duo E8400 3.00 GHz CPU. By moving these image processing routines to a GPU (e.g., NVIDIA GeForce GTX 285), the time required to analyze each semen samples can be significantly reduced (by e.g., >10X).

Microscope comparisons to validate lensfree on-chip imaging: To verify my automatic characterization results made with this holographic on-chip microscope, videos of the same semen samples were also recorded using a conventional bright-field microscope (ME300TZ-2L-5M, AmScope). For each semen sample, these videos were recorded across ≥ 9 adjacent FOVs (~0.20 mm^2 each) using a 20X objective-lens (NT38-339, Edmund Optics, NA = 0.4). Motile and immotile sperms were then separately counted on the recorded video by visual inspection, following the WHO guidelines.[79] For samples that had less than 0.5 million motile sperms per mL, videos were also recorded with a 10X objective-lens (NA = 0.25) that had a relatively larger field-of-view than a 20X objective-lens. However, these lower resolution videos were used for counting of motile sperms only, and were not used to quantify immotile sperm densities. The conventional bright-field microscope videos were always recorded right before the semen samples were imaged by the holographic on-chip microscope. The delay between these two imaging modalities was kept below 30 seconds to minimize the error from the change of semen status. CASA systems were not used for validating my automatic counting results because they are commonly believed to be less reliable than the manual method – which is still considered as the gold standard right now.

4.3 Results and Discussion

To demonstrate the capabilities of my platform shown in Fig. 4-1 for automated detection of sperms from their lensfree holograms, I initially worked with semen samples that had immobilized sperms. In these experiments, lensfree holograms of the immobilized sperms were digitally reconstructed as detailed in the Methods Section to yield both an amplitude and a phase image of each sperm over an imaging FOV covering ~24 mm^2. As examples, Figs. 4-4 and 4-5 digitally focus on smaller regions of this FOV to illustrate some of these raw lensfree holograms, and their corresponding reconstruction results.

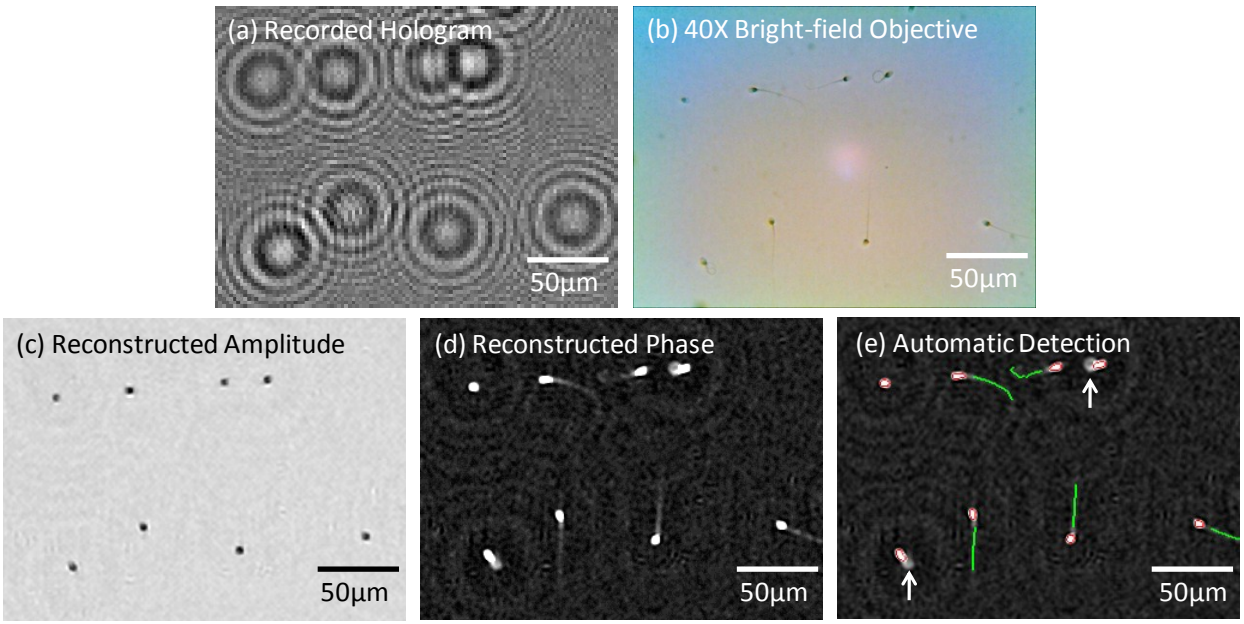

Figure 4-4 | (a) A digitally cropped lensfree hologram of an immobilized semen sample (6.05 million sperms per mL) that is acquired with the unit in Fig. 1(a) is shown. (b) For comparison purposes, a bright-field microscope image of the same FOV as in (a) is acquired with a 40X objective-lens (NA=0.65). (c) The amplitude image reconstructed from the raw hologram shown in (a) for the same FOV indicates the locations of the heads of the sperms. (d) The phase image reconstructed from the raw hologram shown in (a) for the same FOV illustrates both the heads and the tails of the sperms. (e) Automatic characterization results that are generated based on the reconstructed phase image in (d) are illustrated. The elliptical areas corresponding to sperm heads are enclosed by red circles while the tails are labeled with green lines.

Defective sperms with missing or unusually curved tails (marked with the white arrows in (e)) are not reported towards positive sperm counts.

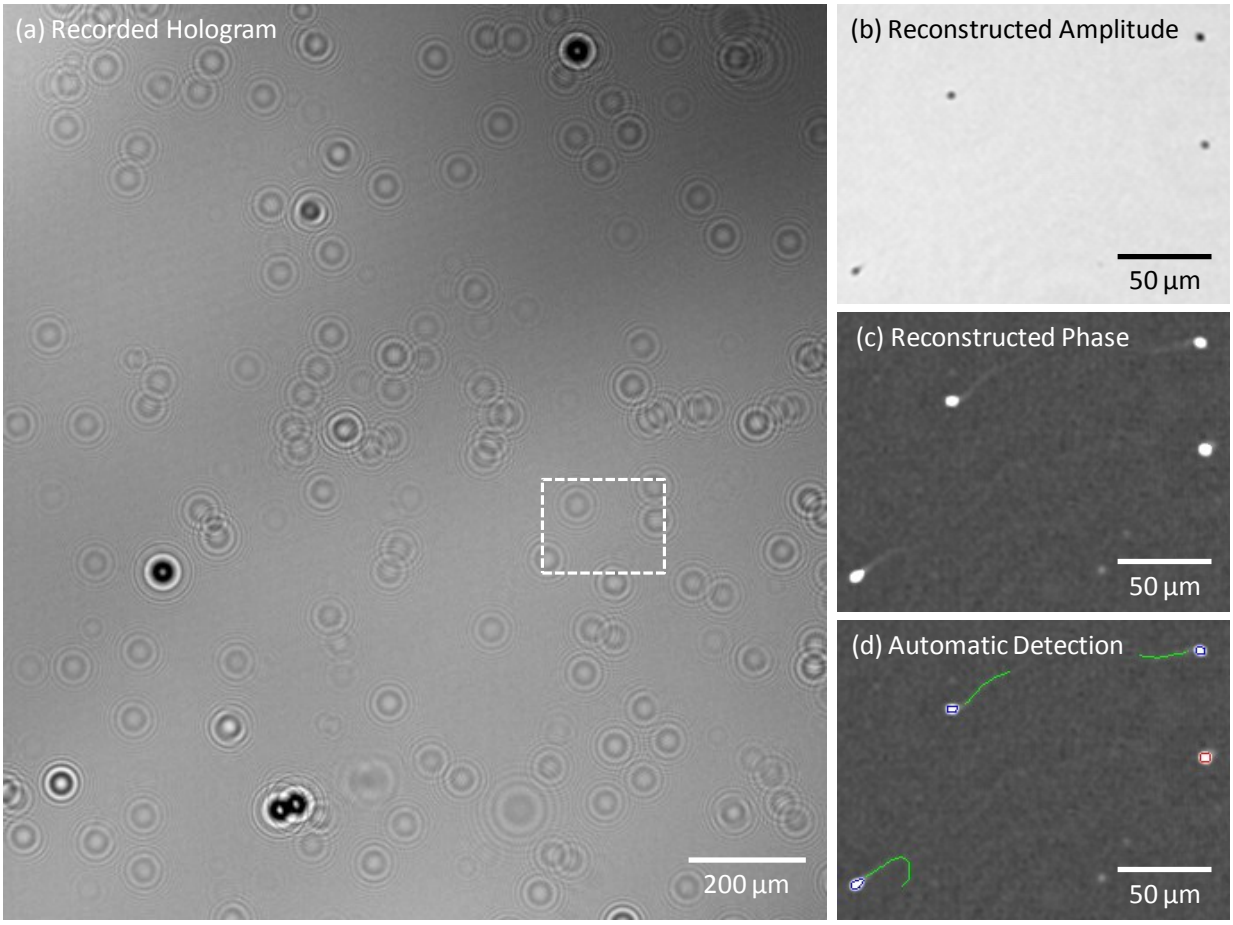

Figure 4-5 | (a) A digitally zoomed lensfree hologram of an immobilized semen sample (1.63 million sperms per mL) is shown. The darker holograms correspond to 20µm beads that were used as mechanical support (see the Methods section), whereas the rest of the lensfree holograms correspond to sperms. The region labeled by a white dashed box stands for the corresponding FOVs of (b), (c), and (d). (b) The amplitude image reconstructed from the raw hologram shown in (a) indicates the locations of the sperm heads over a zoomed FOV. (c) The phase image reconstructed from the raw hologram shown in (a) illustrates both the heads and the tails of the sperms over a zoomed FOV. (d) Automatic characterization results are generated based on the phase image shown in (c). The heads of the sperms are marked by circles and the tails are labeled with green lines. Defective sperms with missing or unusually curved tails are not reported towards positive counts.

An interesting observation based on these images is that the sperm tails can only be observed in the reconstructed phase images, while the heads of the sperms are clearly visible in both the amplitude and the phase images (see e.g., Figs. 4-4(c-d) or 4-5(b-c)). The main reason behind this behavior is that the tail of a sperm is a sub-micron structure which generates a rather weak scattering signal. Therefore, with the limited NA and SNR of my wide-field lensfree microscope, such a small feature does not contribute enough scattering signal to be reconstructed in the amplitude image. On the other hand, the refractive index difference between the tail and the surrounding medium still creates a sufficient contrast in the reconstructed phase image, permitting observation and automated detection of the sperm tails as described in the Methods Section. In these results presented in Figs. 4-2, 4-4(d-e), and 4-5, the tail of each sperm was automatically identified and matched to its corresponding sperm head orientation. In this process, some of the sperms were disqualified from a positive count because of unusually curved tails (refer to the Methods Section for details). To further validate my analysis, these automatic detection results were also compared against a regular microscope image taken on the same field-of-view as shown in Fig. 4-4(b) and 4-4(d-e).

To demonstrate the performance of my platform on quantification of motile sperms, I characterized several semen samples with varying sperm concentrations. Figs. 4-3, 4-6, and 4-7 show the differential imaging and automated tracking results of some of these semen samples. As detailed in the Methods Section, digital subtraction of consecutive frames from each other removes all the stationary holograms and leaves behind only the differential holograms of the motile sperms, as also illustrated in Figs. 4-3(a) and 4-7(a). Therefore, each motile sperm has a distinctive signature on the new differential hologram that represents the magnitude and the direction of the sperm displacement between these two consecutive frames. Performing

holographic reconstruction on these differential holograms reveal two spots for each motile sperm: one dark spot indicating its start position and another bright one indicating its end position (see e.g., Fig. 4-3(b) or 4-7(b)). Based on these reconstructed differential images, I have quantified the dynamic trajectories of the motile sperms over my entire imaging FOV (~24 mm^2) as illustrated in Fig. 4-6(a) or 4-7(c). For further quantification of the sperms shown in Fig. 4-6(a), the displacements of all these motile sperms were linked across all the 20 lensfree frames acquired over ~10 seconds, which enabled us to determine the speed histogram of the sperms as shown in Fig. 4-6(b). Similar results were also obtained at different sperm concentrations as illustrated in Fig. 4-7 for 2.36 million sperms per mL. This average speed histogram calculated by my system is essentially equivalent to the distribution of Straight-line Velocity (also known as VSL) of the sperms, which is reported to highly correlate with fertilization rate,[104] suggesting that the average sperm speed provided by my platform could be an effective indicator of male fertility.

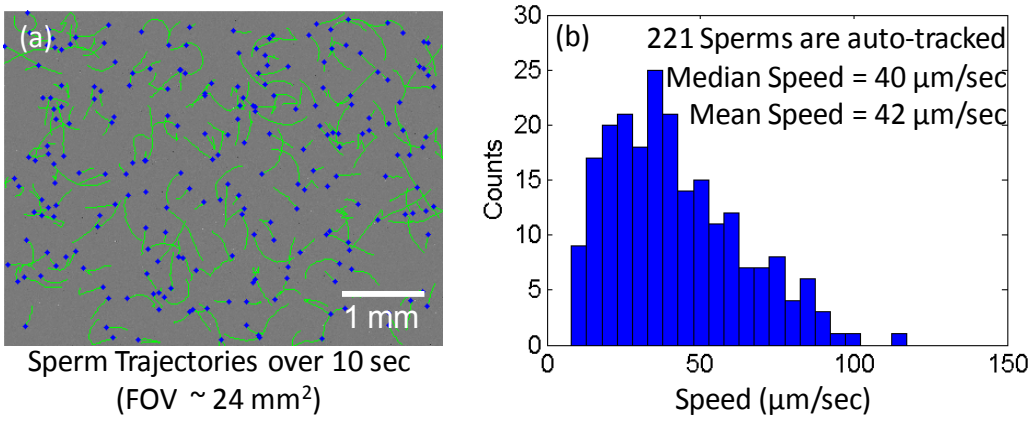

Figure 4-6 | (a) Dynamic trajectories of 221 sperms within a field-of-view of ~24 mm^2 are automatically tracked over a time-span of 10 seconds. The blue spots mark the end positions of the tracked sperms, while the green lines refer to their trajectories. (b) The speed histogram of these motile sperms is calculated using

the information in (a) by summing the sperm displacements from all the consecutive frames and then dividing this sum by the total image acquisition duration.

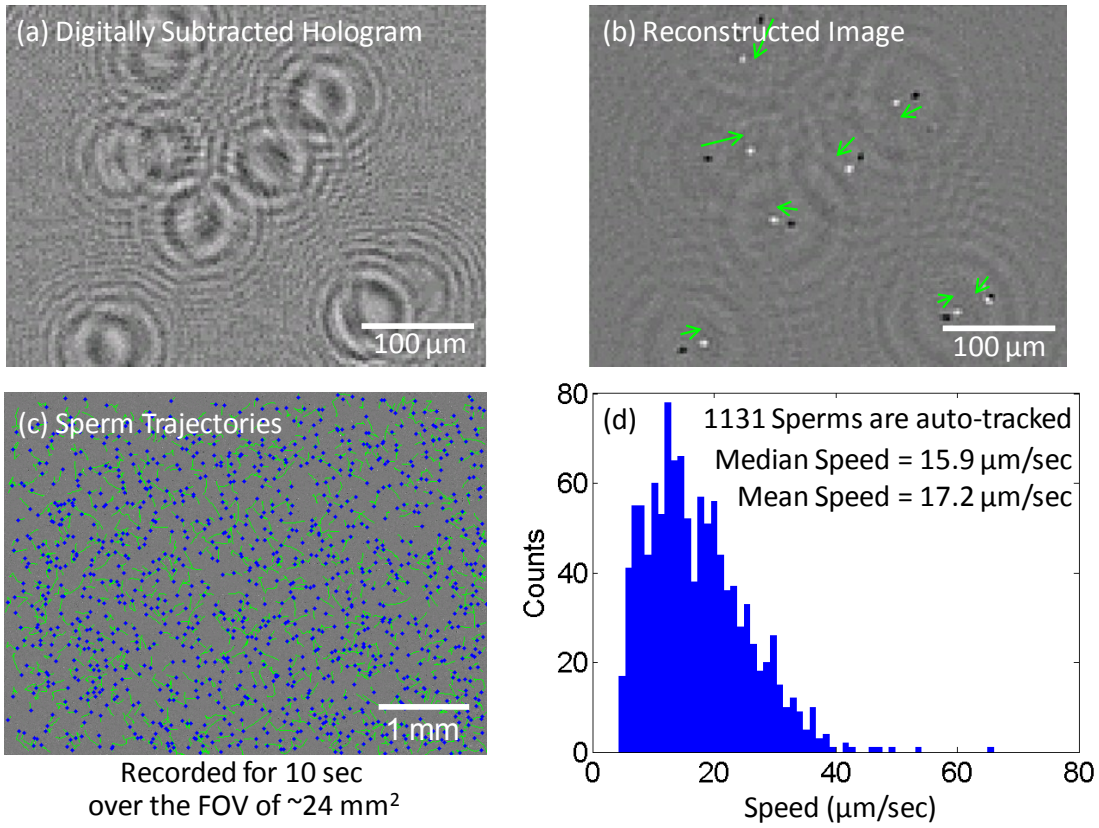

Figure 4-7 | Same analysis as in Figs. 4-3 and 4-6, this time for a more dense semen sample (2.36 million sperms per mL) is illustrated. The dynamic trajectories (green lines in (c)) of 1131 sperms within a field-of-view of ~24 mm^2 are automatically tracked over a time-span of 10 seconds. From these measurements, the speed histogram of these motile sperms is calculated as shown in (d).

Finally, using my on-chip imaging platform, I characterized 12 semen samples containing both immotile and motile sperms at varying concentrations to validate the automated counting accuracy of my system. In Fig. 4-8, my automatic counting results were compared against manual counting results achieved using a bright-field microscope (see the Methods Section). This comparison confirmed that my automated analysis can accurately quantify the concentration

of both immotile and motile sperms up to a density of 8.3 and 6.8 Million/mL, respectively. Such a working range allowed my system to reliably analyze human semen samples that were diluted by 10 folds. In addition to this, Fig. 4-8 also revealed my automated platform's superior ability to analyze semen samples with very low sperm concentrations. For example, the lowest concentration reported in Fig. 4-8 (b), 87,500 sperms/mL, corresponds to ~42 sperms tracked by my system over its 24 mm^2 field-of-view. To achieve the same level of statistical characterization accuracy for such a low density semen sample, a conventional microscope equipped with a 20X objective-lens would need to look at close to 100 different field-of-views, making it quite inconvenient. Therefore, the large field-of-view of my lensfree on-chip imaging platform is also quite valuable for providing quantitative results at extremely low sperm densities such as observed in post-vasectomy.[116,117]

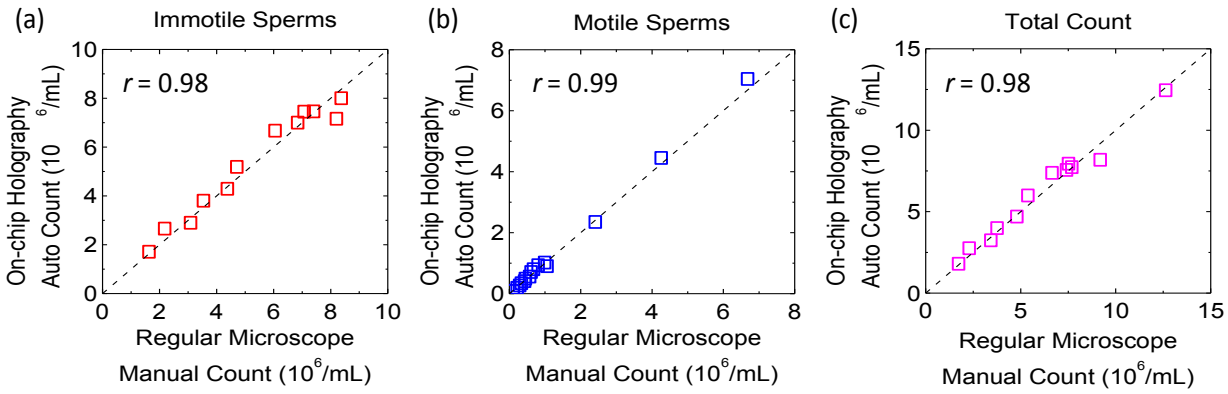

Figure 4-8 | Counting accuracy of the presented automated semen analysis platform for (a) immotile sperms; (b) motile sperms; and (c) both the motile and immotile sperms is illustrated at various sperm concentrations up to 12.5×10^6/mL. The x-axes are the sperm concentrations that are manually counted using a conventional bright-field microscope. The y-axes are the sperm concentrations that are automatically counted for the same semen samples using lensfree holographic images acquired with the on-chip microscope shown in Fig. 1(a). The total counts in (c) are the summed up concentrations of the immotile sperms in (a) and the motile sperms

in (b). Correlation coefficients (*r*) of these characterization results shown in (a), (b), and (c) (0.98, 0.99, and 0.98, respectively) further validate the accuracy of this compact and light-weight holographic lensfree microscope as a semen analysis platform.

The potential applications of this semen analysis platform include automated sperm counting in fertility clinics, semen quality evaluation in sperm banks, personal male fertility test at home, post-vasectomy follow-up check either at home or in clinic, stud performance assessment at animal breeding centers, and stud health monitoring in the stud farms. By using a larger-area image sensor, this platform can be transformed into a high-throughput multi-tasking test platform that can measure sperm's response to different drugs or chemicals of different concentration in parallel.

4.4 Conclusion

In this chapter, I demonstrated a compact and light-weight platform to conduct automated semen analysis using a lensfree on-chip microscope, which weighs ~46 grams and measures ~ 4.2 cm × 4.2 cm × 5.8 cm.[118] Therefore, it fills up an important gap between simple qualitative male fertility test kits and sophisticated quantitative characterization systems based on e.g., CASA. In a very compact and light-weight format, this platform can provide quantitative semen analysis including the measurements of the absolute concentrations of both motile and immotile sperms, as well as the trajectories and the speed distributions of motile sperms. Since several different factors other than the sperm concentration are now being used to predict fertility,[119] such a compact and versatile semen analysis tool could be very useful for fertility clinics, personal male fertility test kits, as well as for field-use in veterinary medicine.

Chapter 5 High-Throughput Lensfree 3D Tracking of Human Sperms Reveals Rare Statistics of Helical Trajectories

5.1 Introduction

Observing three-dimensional (3D) trajectories of sperms is in general a challenging task. This is partially due to limited imaging volume of optical microscopes that are based on conventional lenses. For human sperms this becomes even more challenging since the sperm head is small (e.g., 3-4 μm) demanding a relatively high-magnification objective-lens, and moves rather fast (e.g., 20-100 μm/sec) which makes it difficult to track their 3D swimming patterns as they quickly move out of the observation volume of an objective-lens. Partly due to this low throughput and the limited spatial and temporal sampling windows that conventional microscopes provide, natural 3D swimming patterns of human sperms and their statistics could not be reported so far. Earlier results[120–125,99,126–135] that were obtained using lens-based conventional microscopes either measured the 2D trajectories of the human sperms along a focal plane, or reported on sperms of other species such as sea urchin, which were significantly easier to resolve under a microscope since their 3D rotation diameter is larger (e.g., >13 μm) together with a lower rotation frequency compared to human sperms.

Here I report a new technique that is based on lensfree holographic imaging on a chip to dynamically track the 3D trajectories of human sperms across a large volume of e.g., 8-17 mm^3 (see Fig. 5-1) with sub-micron positioning accuracy. This platform can track >1,500 individual human sperms over several hours, obtaining massive statistics about their 3D swimming patterns across 10-20 seconds for each continuous pattern. The large statistics provided by this lensfree computational imaging platform enabled me to observe, for the first time, the helical trajectories

of human sperms, exhibiting a tight helix radius of 0.5-3 μm, a helical rotation speed of 3-20 rotations/sec and a linear speed of 20-100 μm/sec. Furthermore, this platform revealed that only 4-5% of the motile human sperms swim along well-defined helices, and that this percentage of helical sperms can be considerably suppressed using seminal plasma. Quite interestingly, I also observed that a significant majority (e.g., ~90%) of these rare helical sperms preferred right-handed helices over left-handed ones, which is an observation that is enabled by the large spatial and temporal measurement windows that my on-chip imaging platform provides.

Compared to earlier reports that also used holographic imaging techniques[19,136–143] to track sperms or other micro-organisms, my approach is lensfree (Fig. 5-1) and therefore exhibits a significantly larger imaging field-of-view of e.g., >17 mm^2 together with unit fringe magnification, while still achieving sub-micron positioning accuracy that is necessary to observe human sperms' tight helical paths. Furthermore, instead of using a laser source with high degree of coherence, I use partially-coherent illumination (both spatially and temporally) at two different wavelengths emanating from two light-emitting-diodes (LEDs) that are placed at 45 degrees with respect to each other. This partially-coherent multi-angle illumination at two different wavelengths (i.e., blue and red) significantly suppresses speckle and multiple-reflection interference noise terms as well as cross-interference among sperms' diffraction patterns which make it feasible to track >1,500 sperms with sub-micron positioning accuracy. My results on human sperms demonstrate the unique capabilities of this high-throughput on-chip imaging platform by resolving the tight and rapidly evolving rare helical trajectories of motile sperms. Finally, the same technique might in general be widely applicable for observing the statistical swimming patterns of various other micro-organisms, leading to new insights in their 3D motion and the underlying bio-physics.

5.2 Methods

Preparing and incubating human sperm suspension. Fresh semen specimens within less than one hour after collection (from anonymous donors) were obtained from California Cryobank (CA, USA) without pre-processing. Only specimens with high sperm concentration (>50×10^6 sperms per mL) and high motility (>70% motile) were used in my experiments. The motile sperms were first separated from seminal plasma by centrifugation with density gradient media (ISolate, Irvine Scientific, CA, USA) and then washed twice with artificial human tubal fluid (HTF, Sperm Washing Medium, Irvine Scientific, CA, USA) to completely remove the residue of seminal plasma. After the second washing step, the sperms were re-suspended with various culture media in centrifuge tubes at a concentration of ~10×10^6 sperms per mL and incubated at 37°C with pH buffer HEPES until my imaging measurements. Three different culture media were used in this work: *(i)* Baseline medium, which only contained artificial HTF; *(ii)* suppressing medium I, which was prepared by mixing seminal plasma with HTF by a ratio of 1 to 9; and *(iii)* suppressing medium II, which was prepared by mixing seminal plasma with HTF by a higher ratio of 2 to 8. For all my imaging experiments except the time-traced ones (e.g., Fig. 5), the sperm suspensions were incubated for 2-3 hours. Right before lensfree imaging experiments, 50-150 μL of the sperm suspension was put into a disposable observation chamber prepared by taping a laser-cut Acetal film (0.1-0.5 mm thick) between two pieces of No. 1 cover slips.

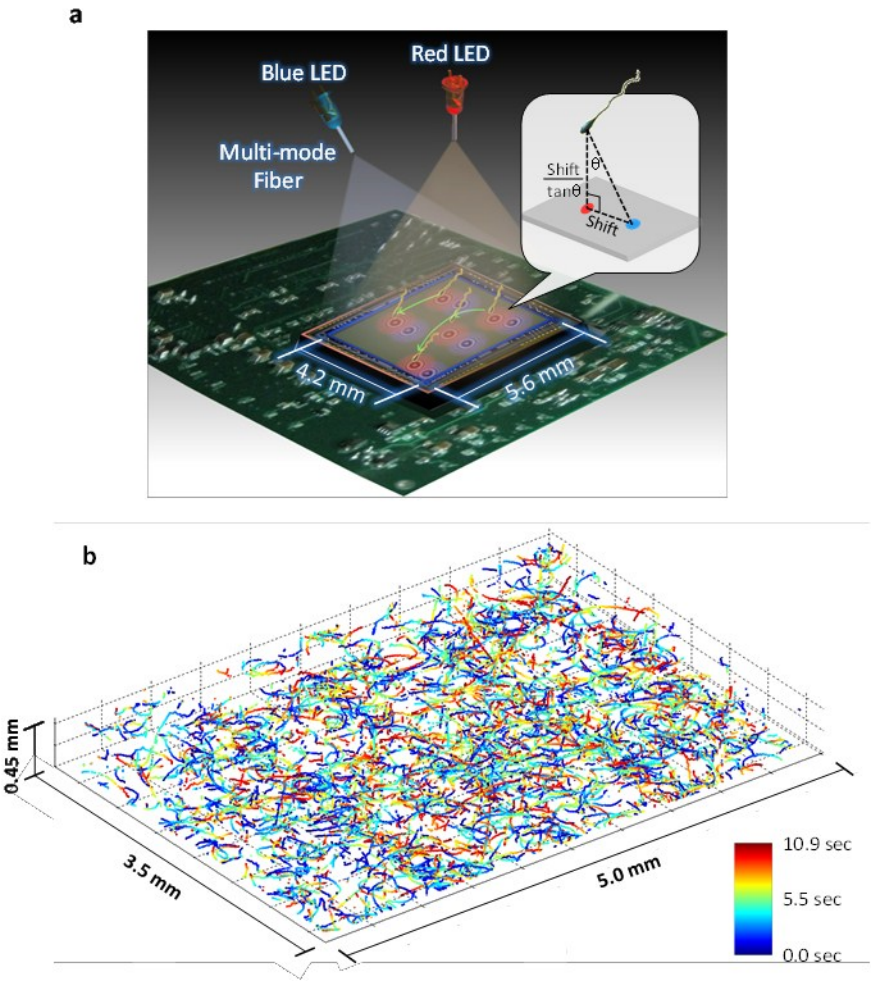

Figure 5-1 | Dual-view lensfree 3D tracking of human sperms. (a) The schematic diagram of the imaging system. Two partially-coherent light sources (i.e., red and blue LEDs at 625 nm and 470 nm, respectively) are butt-coupled to multi-mode fibers (0.4 mm core diameter each) to simultaneously illuminate the sperms at two different angles (red at 0° and blue at 45°). A CMOS sensor chip records the dual-view lensfree holograms that encode the position information of each sperm. The 3D location of each sperm is determined by the centroids of its head images reconstructed in the vertical (red) and oblique (blue) channels. This schematic diagram is not drawn to scale. (b) The reconstructed 3D sperm trajectories. 1,575 human sperms inside a volume of 7.9 μL were tracked at a frame rate of 92 FPS. The time position of each track point is encoded by its color (see the color-bar).

Dual-view and multi-color lensfree holographic imaging set-up. The configuration of my imaging set-up is illustrated in Fig. 5-1(a). The observation chamber containing the sperm suspension is placed directly on top of the protective glass of a CMOS image sensor (Aptina MT9P031STC, 5 megapixels, 2.2 μm pixel size, monochrome) creating a physical distance of ~0.8 mm between the bottom of the chamber and the top surface of the CMOS sensor active area. The sample suspension is simultaneously illuminated by two partially-coherent light sources with different central wavelengths placed at 45 degrees with respect to each other (vertical one: 625 nm; oblique one at 45 degrees: 470 nm). Both light sources were composed of light-emitting-diodes (LEDs, bandwidth ~20 nm) that were simply butt-coupled to multi-mode optical fibers (core size: 0.4 mm) with the fiber tips placed at a distance of ~10 cm from the sample chamber. Such a system, without utilizing any lenses or mechanical-scanners, can *simultaneously* record in-line holograms of the sperms from two different viewing angles over a large field-of-view of e.g., >20 mm^2, while also significantly reducing unwanted noise terms such as speckle patterns, multiple reflection interference noise or cross-interference among sperms' holograms.[67,144]

To capture the dynamics of the sperms with minimum motion blur, the electronic shutter of the CMOS image sensor was set to 5 ms for defining the integration time of each pixel. The FOV of the CMOS imaging platform (i.e., 24 mm^2) was digitally programmed into 16 regions-of-interest (ROIs), which were sequentially recorded at a frame rate of 92 frames per second (FPS) for continuous intervals of 1-20 seconds each. The resulting video data were transmitted to a PC in real time through a gigabit Ethernet connection. To avoid the heating of the image sensor between tracking experiments, which might damage the sperms inside the observation chamber, a programmable power relay (connected to the PC through a USB interface) was used to cut-off

the power of the image sensor between video acquisitions. The ON-OFF cycle of the image sensor was carefully configured to maintain the observation chamber at 36-37°C for several hours. A custom-designed LabVIEW program was used to coordinate the image sensor and the power relay for maintaining the temperature as well as to digitally scan over the 16 ROIs of the observation chamber. Scanning over 16 ROIs (with >1,600 lensfree holograms) and recording the trajectories of >1,500 sperms takes ~10 minutes for each semen sample. However, this acquisition time can be significantly reduced to ~30 seconds if external cooling is provided to prevent the overheating of the observation chamber.

3D tracking of human sperms. The lensfree holographic frames recorded by the CMOS image sensor were first individually reconstructed on all the possible object planes (with 25 μm vertical spacing) within the observation chamber, for both the vertical red illumination and the oblique blue illumination. This digital reconstruction process for each illumination angle follows the iterative phase recovery method that is detailed in a previous publication.[145] Because the spatial information of each sperm was encoded with different wavelengths at two viewing angles, only the reconstruction that is performed with the correct combination of distance (i.e., depth), angle, and wavelength can generate clear images of the sperms (see Fig. 5-2). Since incorrectly reconstructed projection holograms of the sperms would only show up as weak background noise, the sperm head images projected in two different viewing angles at two different wavelengths can be isolated from each other although they were recorded at the same lensfree holographic frame. This provides an important solution to avoid confusing different projections of different sperms with each other, especially at high sperm densities, making my 3D tracking algorithm quite robust. Furthermore, without the need to record different viewing angles separately, this

multi-color approach also simplifies my system, eliminating the use of e.g., pulsed light sources, high-speed digital cameras, and the synchronization between them.

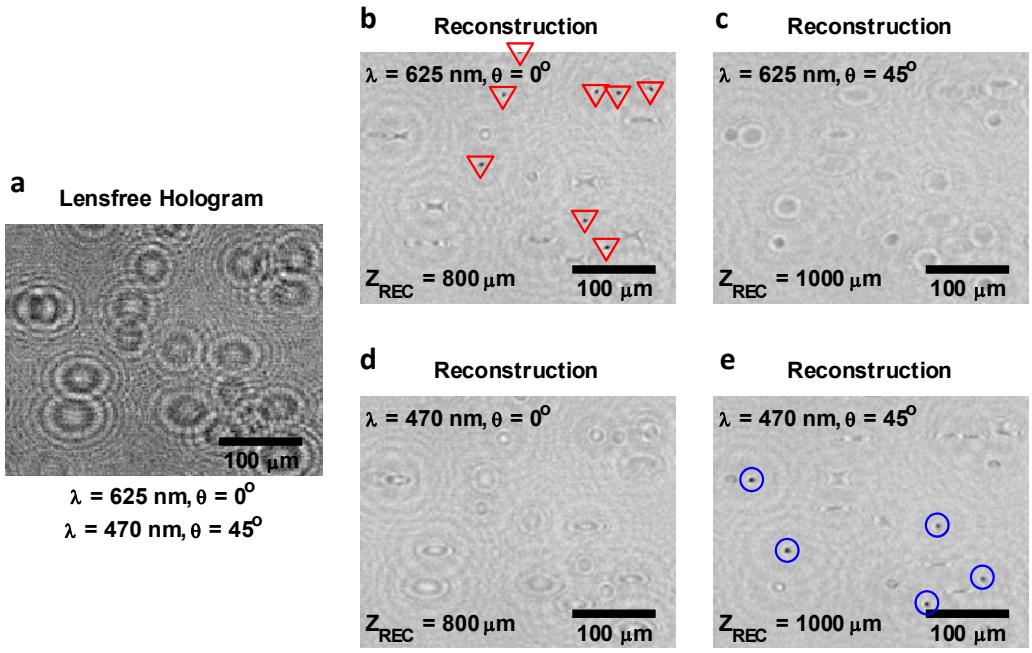

Figure 5-2 | Digital separation of the sperms' vertical and oblique lensfree projections through dual-angle and dual-color partially-coherent illumination. (a) A lensfree image showing several sperm holograms recorded with a red LED at the vertical angle and a blue LED at the oblique angle *simultaneously* illuminating the sample. (b)-(e) Lensfree amplitude images that were digitally reconstructed from the same region of interest shown in (a), but each with the conditions specified in its legends. The red triangles in (b) mark the successful detection of the vertical projections of the sperms, whereas the blue circles in (e) label the successful detection of oblique projections. Reconstruction with parameters that are not matched to the original illumination conditions would only create weak noise at the background as illustrated in (c-d).

In each reconstructed lensfree frame, possible sperm candidates were segmented by thresholding the amplitude image for both color channels. Detection artifacts were filtered out with a series of morphological criteria, such as peak value, area, and eccentricity.[115] Once

confirmed as the projection of a sperm, the 2D centroid position of each sperm projection in both color channels was calculated by its center-of-gravity[115] based on the square of its reconstructed amplitude profile. At the same time, the focal distance of each vertical projection (which was estimated as the distance with the highest contrast in its reconstructed 2D image stack) was taken as the 'coarse' vertical (i.e., z) distance of the sperm from the CMOS sensor chip. This initial estimate has a lower depth accuracy of 5-10 μm and is just used to search for the corresponding projection of each sperm in the oblique illumination channel. The 2D centroid position of the sperm head projection in the vertical channel was directly used as the sperm's x-y coordinate. The precise z coordinate of the sperm was then calculated by dividing the distance between its vertical and oblique projection centroids with the tangent of the oblique illumination angle in water (see Fig. 5-1(a)).

Since the centroid coordinates of the vertical and oblique projections can be determined with an accuracy much better than the 2.2-μm CMOS pixel size,[115] this approach can localize individual sperms in 3D with sub-micron accuracy. To shed more light on this, I conducted characterization experiments with 3 μm particles that are spread across flat glass surfaces, and the results of these experiments confirmed that this platform can provide a 3D localization accuracy of 0.3-0.5 μm across a depth-of-field of ~2.7 mm (see Fig. 5-3). Note that at larger depths (>3 mm) the signal-to-noise ratio of lensfree holograms relatively degrades, reducing my 3D localization accuracy. 3 μm particles were chosen for these characterization experiments since they exhibit a contrast that is matched to human sperms in the reconstructed amplitude images. It should be also emphasized that the swimming sperm tails do *not* constitute a problem in the localization calculations since they are considerably narrower (≤0.6 μm) compared to the sperm head (3-4 μm wide) and exhibit very weak light scattering,[118] which significantly

decreases their holograms' strength compared to the sperm heads' holograms. This behavior is also confirmed by the fact that the swimming sperm tails do not appear in the reconstructed amplitude images of my lensfree system (see e.g., Fig. 5-2).

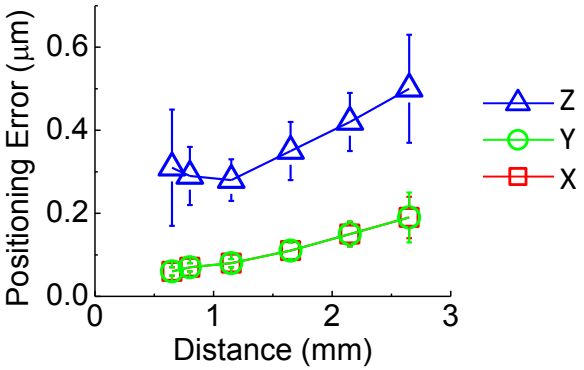

Figure 5-3 | The localization accuracy of the lensfree 3D tracking system as a function of the vertical distance from the sensor surface. The positional error was characterized by tracking micro-particles (diameter: 3 μm) that are spread across flat glass surfaces and by calculating the standard deviation of 3D positions for individual stationary particles. The vertical distance is defined by the separation between the localized object and the imaging plane of the CMOS sensor, which was adjusted by inserting glass slides of different thicknesses. Error bars define s.d..

The same 3D localization procedures outlined above for human sperms were repeated for each recorded lensfree holographic frame to generate a 3D-t (i.e., *space-time*) matrix, which contains the spatial and temporal coordinates of all the sperm head positions detected in the observation volume. The trajectory of each sperm as a function of time was then constructed by linking up the nearest detected points[118] across the reconstructed 3D amplitude frames. To improve the tracking accuracy, a Brownian-statistics-based algorithm[146] is also used for better handling noise in my measurements.

Digital classification of the reconstructed sperm trajectories. The 3D swimming patterns of human sperms were categorized based on several dynamic parameters extracted from their reconstructed 3D-t trajectories, such as curvilinear velocity, linearity, lateral displacement, and number of stable turns (rotations). All the parameter extraction performed in this work was based on either 1.1 sec-long trajectories (~100 frames at 92 FPS) or track segments of such length that were digitally extracted from longer trajectories (e.g., 10-20 sec long).

Before automatically extracting these dynamic parameters for each sperm within the observation volume, the reconstructed 3D trajectory segments need to go through a digital "*straightening*" process to compensate the curvature in their 3D motion. For this end, a 3D parabolic curve model was used to fit the curved moving axis of each segment by minimizing the square of the distance between all the position points and the fitted axis (where the distance was created by the sperm's lateral displacement). All the position points were then reassigned laterally onto a plane moving along the axial direction according to their relative position to the fitted axis (see e.g., Figs. 5-4(a), (b), and (c)). After this digital straightening step, the moving axis of each segment became a straight line and the position points evolved laterally around the fitted axis. The lateral coordinates of the position points (i.e., the X_r and Y_r in Figs. 5-4(b) and (c)) were then used to calculate the instantaneous radius and the angle of the trajectory points (see Figs. 5-4(d) and (e)), where the instantaneous angle was further unwrapped to eliminate possible 2π phase jumps and fitted with a linear function to estimate its rotation speed.

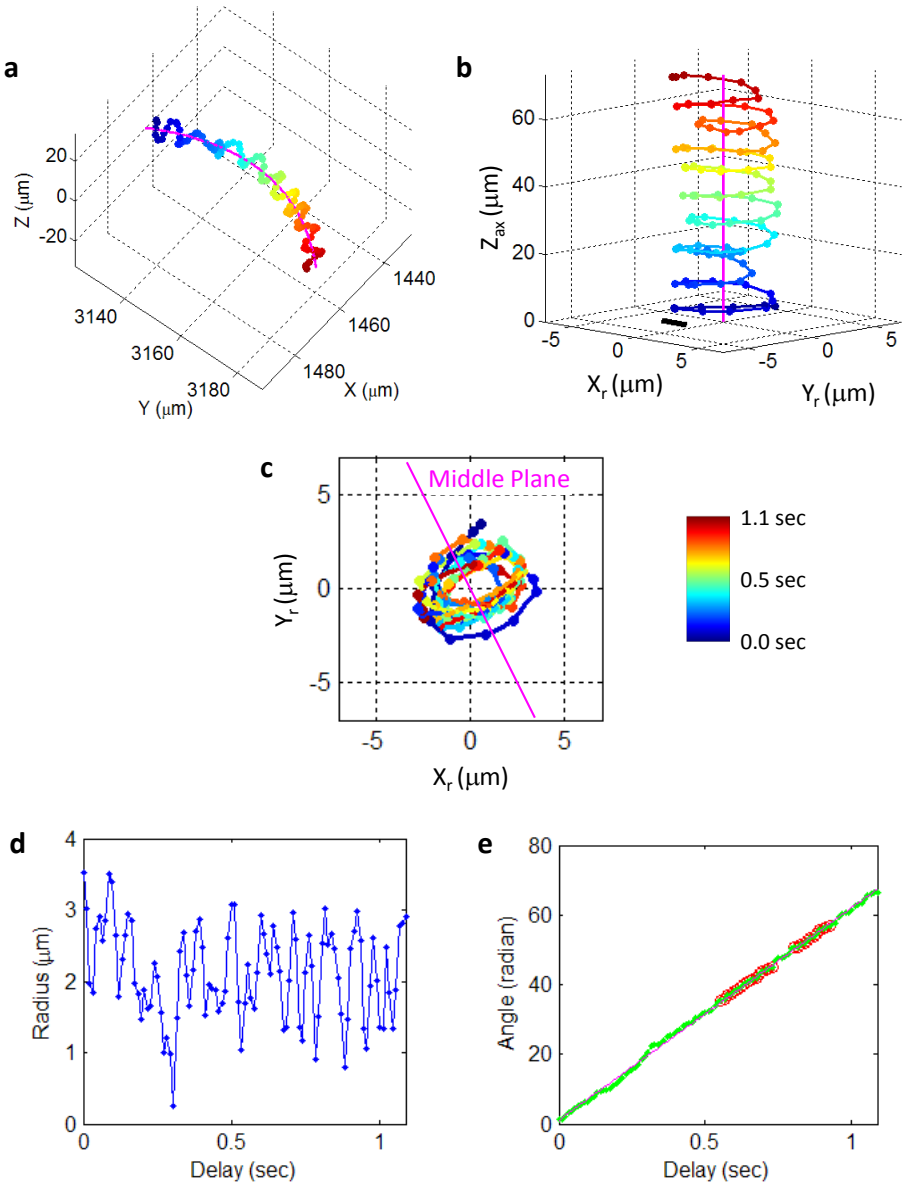

Figure 5-4 | Detection of a helical trajectory for a human sperm. (a) The original human sperm helix fitted with a parabolic line (magenta color) as its curved axis. (b) The same helix is "straightened" by replacing each point along a straight axis according to its relative displacement to the fitted axis (the magenta line). (c) The front-view of the "straightened" helix shown in (b). The magenta line marks the "middle plane" that is used to measure the beat-cross frequency. The instantaneous radius (d) and angle (e) extracted from the lateral coordinates (i.e., Xr and Yr) of the helix shown in (c). The angle in (e) is first unwrapped to eliminate possible 2π phase jumps and then fitted with a linear function (the magenta line) to match a stable rotation.

Red circles on the magenta line in (e) mark the angular data points (the green dots) that lie within ±0.6 radians from the fitted linear function.

To report the 3D dynamic swimming parameters of human sperms in a format that is compatible with the currently existing standards, I appropriately modified the parameters that are used by computer-aided sperm analysis (CASA) systems,[99] which can be summarized as below:

Straight-line velocity (VSL) is defined as the distance between the first and the last position points in the track segment of a sperm trajectory divided by the total duration of the track segment (unit: μm/sec).

Curvilinear velocity (VCL) is defined as the sum of the distances between every two consecutive position points in a track segment divided by the total duration of the track segment (unit: μm/sec).

Linearity is the ratio between straight-line velocity and curvilinear velocity (VSL/VCL) of a track segment (unit: none).

Amplitude of lateral head displacement (ALH) is defined as twice the maximum displacement of a sperm head from its fitted moving axis in a track segment (unit: μm). It is directly related to the level of bending in the proximal region of the tail[125] (i.e., a larger ALH value corresponds to stronger bending).

Beat-cross frequency (BCF) is defined as the frequency that the sperm head moves across the "middle plane" of the "straightened" trajectory (unit: Hz). The "middle plane" is determined as the plane in the X_r-Y_r-Z_{ax} space that contains the central axis Z_{ax} and has the most frequent crossing-over of the sperm head (see Fig. 5-4(c)). The value of BCF is in general sublinearly proportional to the beating frequency of the sperm tail and is roughly double the frequency of head wobbling.[122]

Rotation speed (RPS) is defined as the slope of the linear function that best fits the time evolution of the unwrapped rotation angle of a sperm head projected on the X_r-Y_r plane (unit: revolutions per second, r/sec). It represents how fast a helical track segment revolves around its moving axis and is roughly half of the value of the trajectory's beat–cross frequency.

Number of stable turns (NST) is defined by multiplying the rotation speed of a sperm with the duration that a track segment maintains a small error (≤ 0.6 radians in this study) to the fitted linear function in its unwrapped angle (see Fig. 5-4(e)); unit: none. The segment with a small angle error needs to be longer than one rotation cycle for being counted into the number of stable turns. NST represents how close the track segment is to a bended helix and I chose a value equal to or larger than 2 to qualify this track segment as a helical sperm trajectory.

Note that in this chapter all the human sperm trajectories with a VCL that is smaller than 30 μm/sec are considered as immotile.[147] The motile sperm trajectories that cannot be classified as helical, hyper-activated, or hyper-helical are then classified as "typical" trajectories. For distinguishing helical, hyper-activated and hyper-helical 3D sperm trajectories from 'typical' ones, the following criteria have been used:

Helical trajectory – NST ≥ 2.0 (see Fig. 5-7).

Hyper-activated trajectory – VCL needs to be larger than 150 μm/sec; the linearity needs to be smaller than 0.5; and ALH needs to be larger than 7.0 μm.

Hyper-helical trajectory – All the requirements for both helical and hyper-activated trajectories need to be satisfied.

Because of the fact that the fitting of helices requires more than two stable turns and that the hyper-activated sperms can change their swimming patterns back and forth within a few seconds,[124] longer sperm trajectories are digitally divided into track segments that are each ~1.1

sec long, which is long enough for fitting a helix but short enough for minimizing swimming pattern transitions within each segment.

Automated processing of 3D sperm trajectory data. Data processing procedures including reconstruction of lensfree holographic images, localization of sperms' 3D centroids, tracking sperms' motion, and classification of their 3D swimming patterns were performed fully-automated with custom-designed Matlab programs. The typical computation time for automatic processing of e.g., ~1,600 lensfree images from a single semen sample is ~2.2 hours (using Matlab R2011a running on a PC with an eight-core Intel Core i7-930 2.80GHz processor). Since most of these procedures are highly repetitive and parallelizable, this computation time can be significantly shortened (by e.g., >5-10X)[148] once my algorithms are further optimized for execution on e.g., graphics processing units (GPUs).

5.3 Results

Human sperms exhibit a large variation in their 3D swimming patterns, and therefore using my dual-view lensfree holographic imaging platform (Fig. 5-1) I initially grouped these swimming patterns into four major categories as exemplified in Fig. 5-5 (i.e., typical, helical, hyper-activated, and hyper-helical; refer to the Methods Section for their definitions and see Table 5-1).

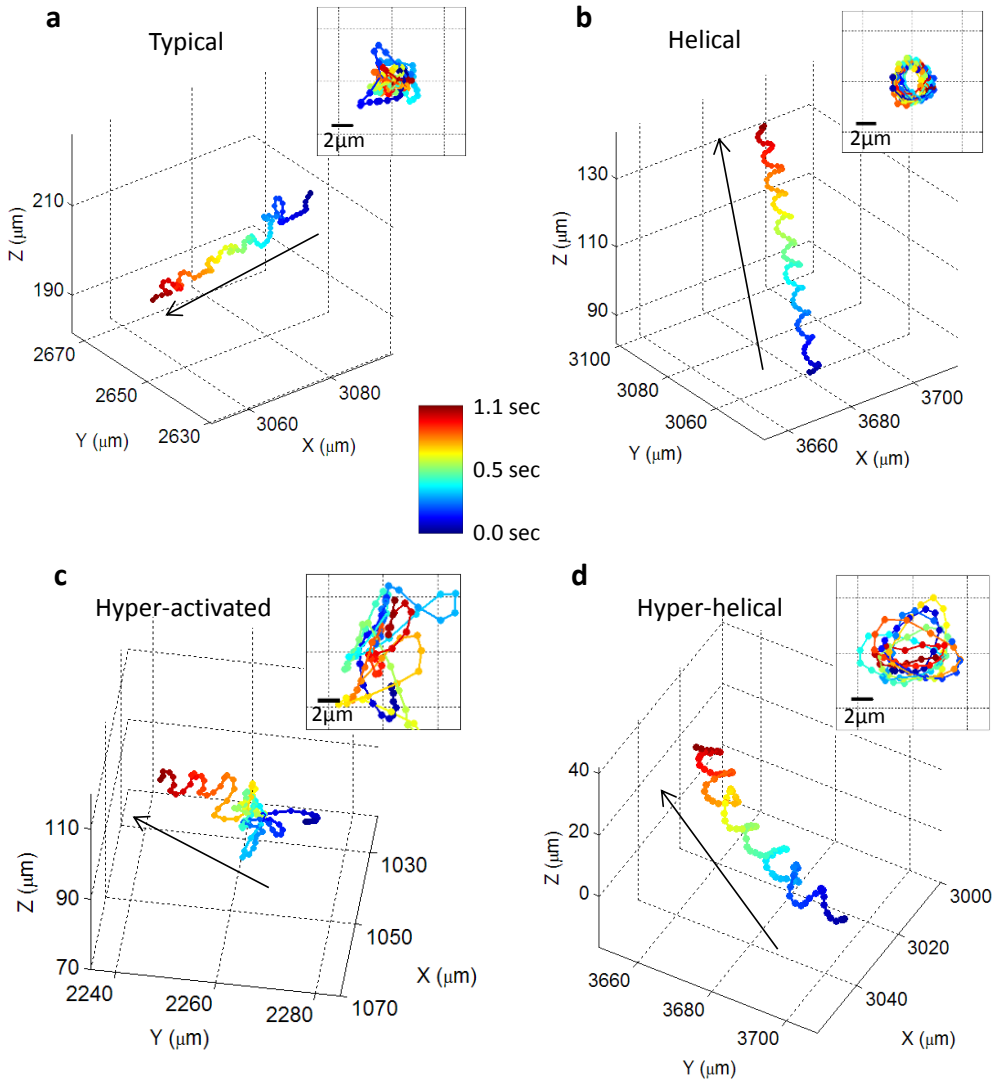

Figure 5-5 | Four major categories of human sperm swimming patterns. (a) The 'typical' pattern. (b) The helical pattern. (c) The hyper-activated pattern. (d) The hyper-helical pattern. The inset in each panel represents the front-view of the "straightened" trajectory of the sperm (see the Methods section for details). The arrows indicate the directions of the sperms' forward movement. The time position of each track point is encoded by its color (see the color-bar). The helices shown in (b) and (d) are both right-handed. Some other examples of human sperm trajectories are also provided in Figs. 5-6, 5-7, and 5-8.

Typical	Helical	Hyper-activated	Hyper-helical
92.9% (±5.3%)	4.4% (±1.5%)	2.5% (±1.3%)	0.2% (±0.2%)

Table 5-1 | The relative ratios of different swimming patterns observed in 28 measurements of 6 semen specimens from different donors, containing 24,090 motile human sperms. The standard deviations listed in parentheses were obtained by calculating the deviation of each ratio observed across all the 28 measurements. These measurements were made in baseline medium (artificial HTF) after >2 hours of incubation as described in the Methods Section.

The 'typical' trajectory shown in Fig. 5-5 (a) is the most prevalent swimming pattern observed among human sperms (>90%, see Table 5-1), in which the sperm head moves forward swiftly (as fast as e.g., 140 μm/sec) along a slightly curved axis with a small lateral displacement (e.g., ~4 μm side-to-side). In this category (i.e., 'typical'), although the lateral displacement exhibits a certain degree of periodicity, the sperm head changes its direction arbitrarily in 3D space (see e.g., Figs. 5-5(a) and 5-6(a), (c), (d)). However, when these typical trajectories are located near the chamber boundaries, some of them also exhibit lateral displacements that are better confined to a two dimensional plane which is not necessarily parallel to the boundary (see e.g., 5-6 (b)).

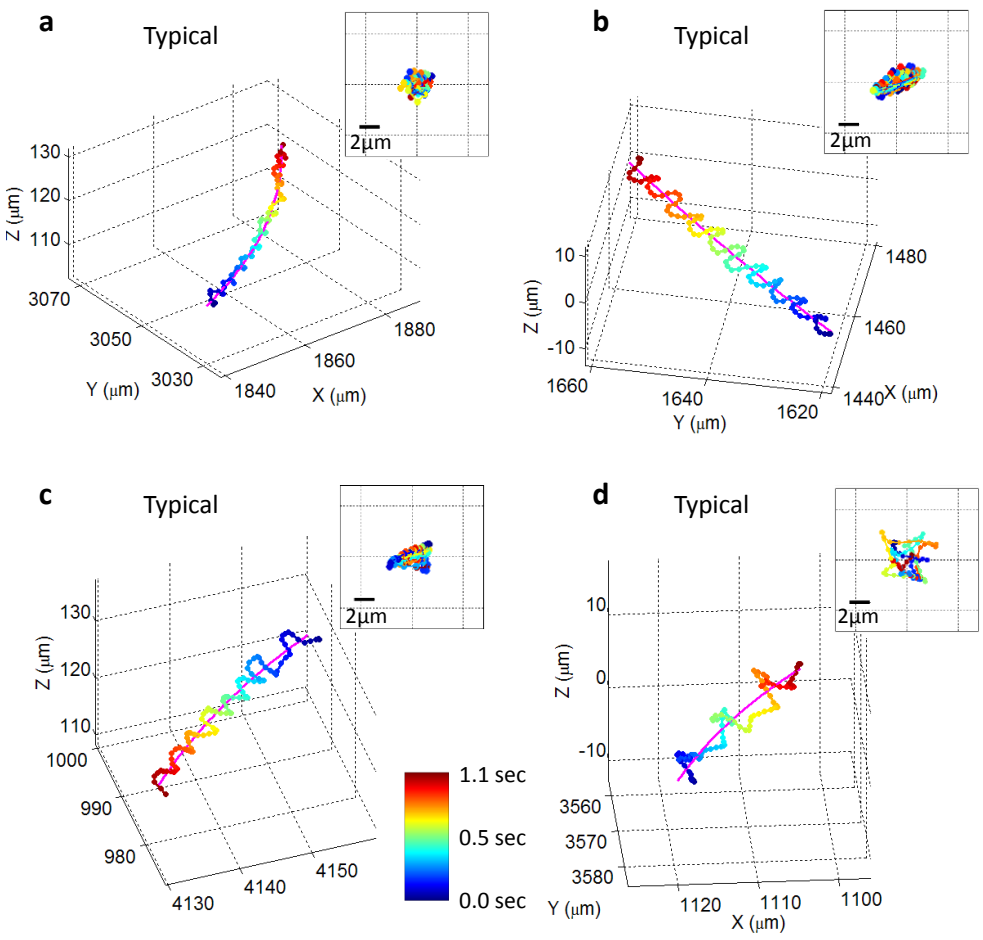

Figure 5-6 | Additional examples of human sperm 'typical' swimming patterns. The inset in each panel is the front-view of the "straightened" trajectory of the sperm. The plane of Z = 0 is roughly aligned with the bottom of the observation chamber. The time position of each track point is encoded by its color (see the color-bar).

In the second category of swimming patterns that human sperms exhibit, I observed helical trajectories (4-5% of motile human sperms, see Table 5-1) as exemplified in Fig. 5-5(b), which show the sperm head moving forward with very stable revolutions around a central axis, creating a well-defined helix. Not only this helical trajectory (e.g., Fig. 5-5(b)) is quite tight with an average helix radius of e.g., ~1.7 μm and a rotation speed of e.g., ~10 rotations/sec, but also it moves rather fast traveling more than e.g., 30-40 μm in depth-of-field (i.e., z direction) within ~1

sec making it rather challenging to observe with a typical objective-lens due to its limited depth-of-field and observation volume. In contrast to 'typical' swimming patterns, I observed that the structure of these helical patterns did not alter much when the sperm head was near the boundaries of the observation chamber (see e.g., Fig. 5-7).

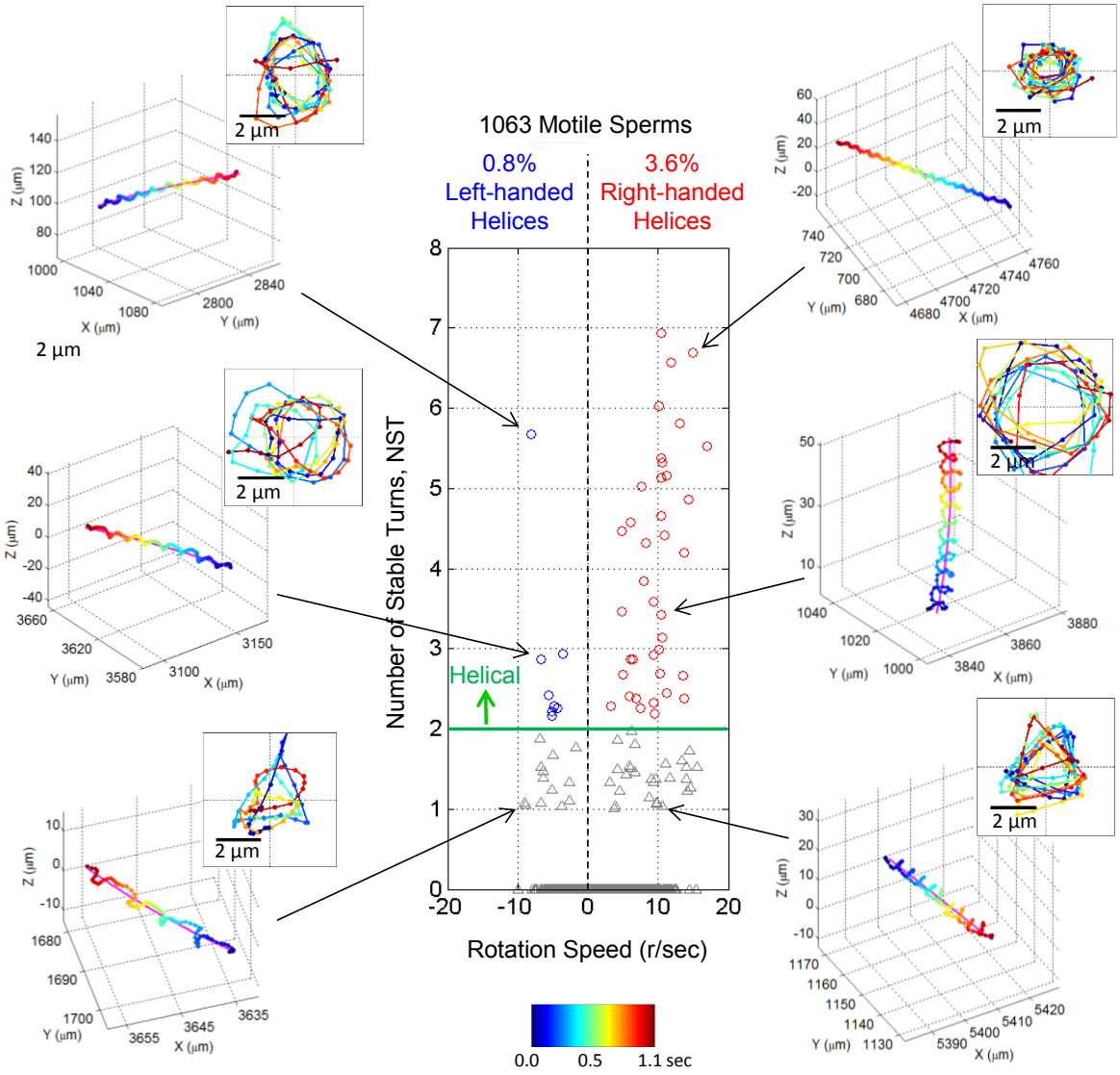

Figure 5-7 | Various examples of human sperm helical trajectories with different NST values. Within a given track period of ~1.1 sec, a trajectory with more than two stable turns (NST ≥ 2.0) is considered as a helical

one (see the Methods section for details). The plane of Z = 0 is roughly aligned with the bottom of the observation chamber. The time position of each track point is encoded by its color (see the color-bar).

In my third category, I observed hyper-activated 3D swimming patterns (<3% of motile human sperms - Table 5-1) that exhibit quite different movement compared to the previous two pattern types (see e.g., Fig. 5-5(c)). The most noticeable change in a hyper-activated pattern is the decrease of its forward movement, despite the fact that the instantaneous speed of hyper-activated sperms (e.g., >150 μm/sec) is usually 2X faster than the instantaneous speed of 'typical' or 'helical' sperms. Most of the track length of a hyper-activated human sperm is consumed by the increased lateral movement, which has a size of >7 μm from one side to the other (see e.g., Fig. 5-5(c)). This hyper-activated swimming pattern can be also divided into two sub-categories, similar to 2D observations:[124] (*i*) transitional hyper-activation, where the sperm still moves forward with a "meander" track (see e.g., Figs. 5-5(c) and 5-8(a), (c)); and (*ii*) "star-spin" hyper-activation (mostly observed near the chamber boundaries), where the sperm bounces around vigorously but totally loses its forward movement as illustrated in e.g., Fig. 5-8(b). Similar to the 'typical' swimming patterns, many of the sperms in transitional hyper-activation category show quasi-2D lateral displacement near the chamber boundaries (compare e.g., Figs. 5-8(a) and (c), where the latter is much better confined to a plane).

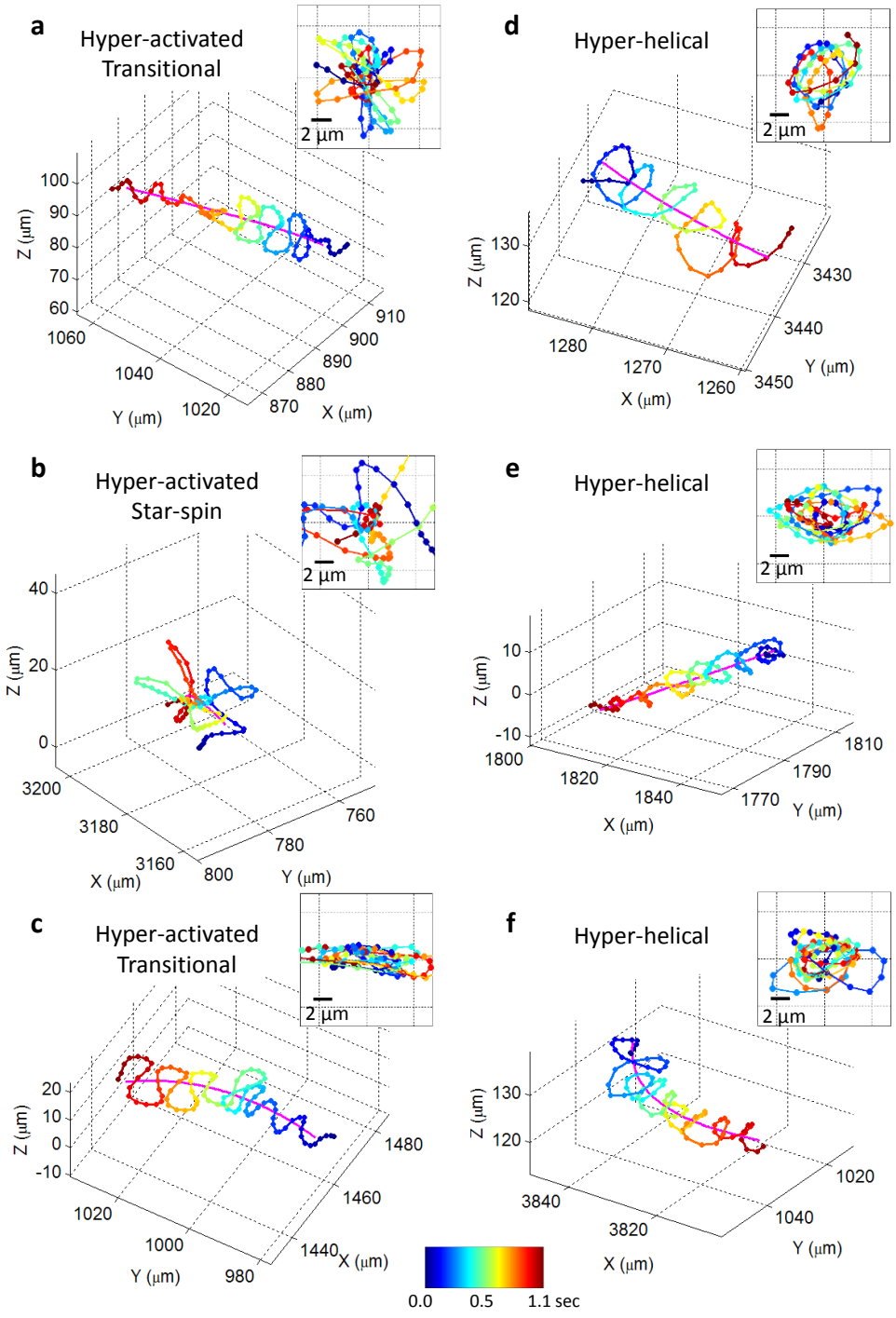

Figure 5-8 | Additional examples of hyper-activated (a-c) and hyper-helical (d-f) trajectories of human sperms. The inset in each panel is the front-view of the "straightened" trajectory of the sperm. The plane of Z = 0 is roughly aligned with the bottom of the observation chamber. The time position of each track point is encoded by its color (see the color-bar).

In the final category of human sperm swimming patterns, I observed hyper-helical patterns (see e.g., Figs. 5-5(d) and. 5-8(d)-(f)) which can be considered as a combination of transitional hyper-activation and regular helical trajectories, exhibiting enlarged and slightly more unstable revolutions around a helix axis with a sustained forward movement. This swimming pattern was significantly rare, constituting only <0.5% of motile human sperms (see Table 5-1). No major difference in swimming patterns was observed between the hyper-helical trajectories located in free 3D volume and the ones located near the chamber boundaries.

An important feature of the presented lensfree on-chip imaging approach is that it can track 3D trajectories of >1,500 human sperms over a large sample volume, which enables me to observe the transitions among different swimming patterns across a time window of 10-20 sec for each continuous sperm trajectory. Figure 5-9 and 5-10 illustrate some examples of such swimming pattern transitions acquired using my lensfree imaging platform. Based on my measurement results, Table 5-2 summarizes the statistics of such transitions among different swimming patterns observed in human semen samples. These results reveal that most of the observed helical and hyper-activated trajectories quickly switch back to 'typical' swimming patterns (e.g., ~64% for helical trajectories and ~58% for hyper-activated trajectories), which indicates that both patterns are temporary behaviors of human sperm with life spans in the range from a few seconds to several tens of seconds.

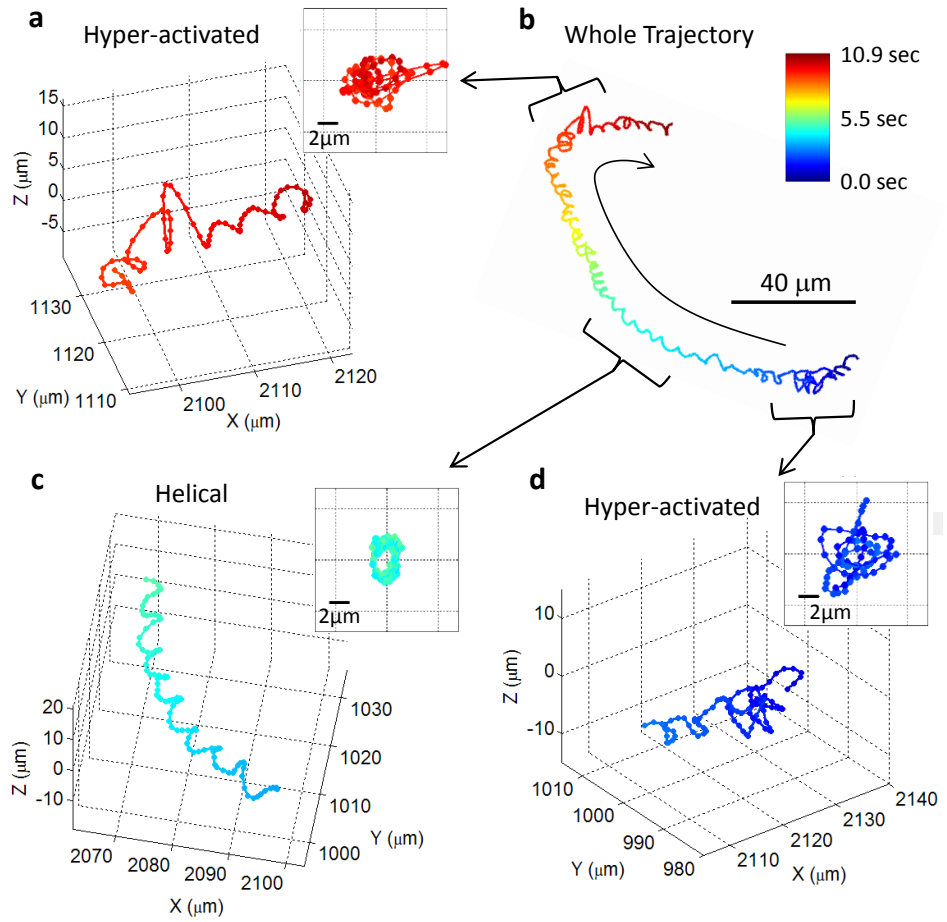

Figure 5-9 | A 10.9-sec long trajectory showing the transitions between different swimming patterns of a human sperm. (a), (c), and (d) illustrate digitally extracted segments (~1-sec long each) of the whole sperm trajectory shown in (b). More sample trajectories with different pattern transitions are also provided in Fig. 5-10. The inset in each panel is the front-view of the "straightened" trajectory of the sperm. The time position of each track point is encoded by its color (see the color-bar).

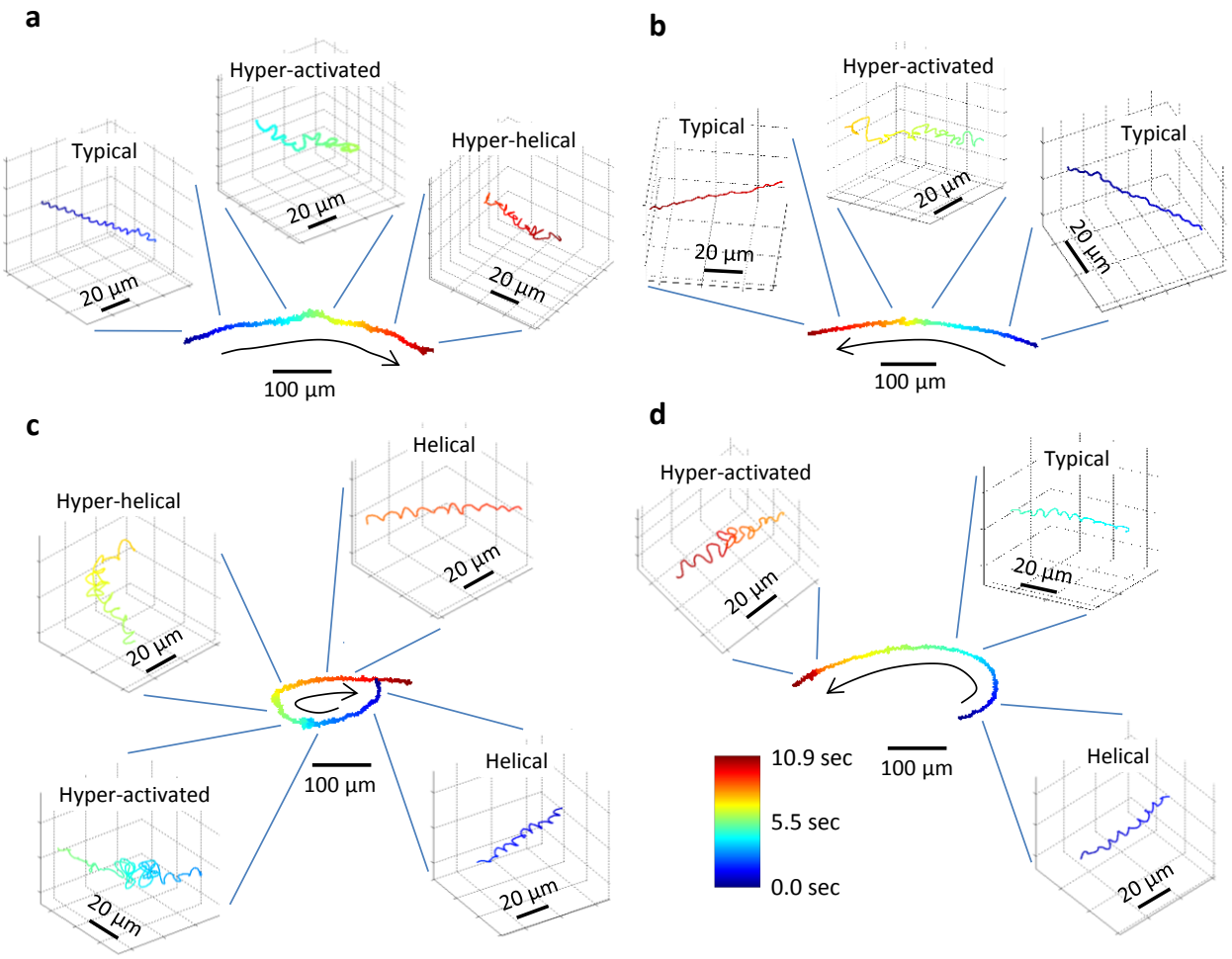

Figure 5-10 | Additional examples of human sperm trajectories showing the transitions among different 3D swimming patterns. The whole trajectories shown in (a), (b), (c), and (d) are each 10.9-sec long, and the insets are digitally extracted segments of ~1.1-sec. The time position of each track point is encoded by its color (see the color-bar).

From \ To	Typical	Helical	Hyper-activated	Hyper-helical
Typical	85.1% (±8.1%)	10.1% (±7.0%)	4.8% (±4.1%)	0.0% (±0.0%)
Helical	63.8% (±25.0%)	30.0% (±22.1%)	5.0% (±10.3%)	1.3% (±3.6%)
Hyper-activated	57.7% (±31.3%)	2.1% (±4.7%)	30.9% (±28.6%)	9.3% (±9.2%)
Hyper-helical	36.7% (±38.5%)	13.3% (±30.7%)	40.0% (±44.9%)	10.0% (±30.3%)

Table 5-2 | The relative percentage of swimming pattern transitions (*From-To*) observed within 3,473 segments (each ~1.1 sec long) of 656 human sperms trajectories (each 5.5-10.9 sec long). The standard deviations in parentheses were obtained by randomly dividing the 656 trajectories into 16 groups and calculating the relative percentage deviation of each transition across these groups.

The human sperm tracking experiments can be further summarized in Fig. 5-11, where I quantify various parameters of 3D swimming patterns, e.g., curvilinear velocity (VCL), straight-line velocity (VSL), amplitude of lateral head displacement (ALH), beat-cross frequency (BCF), linearity (see the Methods Section for details), and compare them to the statistical behavior of only the helical human sperms, which constitute <5% of the motile sperms. The mean values of these swimming parameters and their standard deviations are also listed in Table 5-3. Based on these results, it is rather interesting to note that a significant majority (~90%) of helical human sperms in baseline medium prefer right-handed helixes over left-handed ones (see e.g., Fig. 5-11(f)), exhibiting a tight helix radius of e.g., 0.5-3 μm and a rotation speed of e.g., 3-20 revolutions/sec.

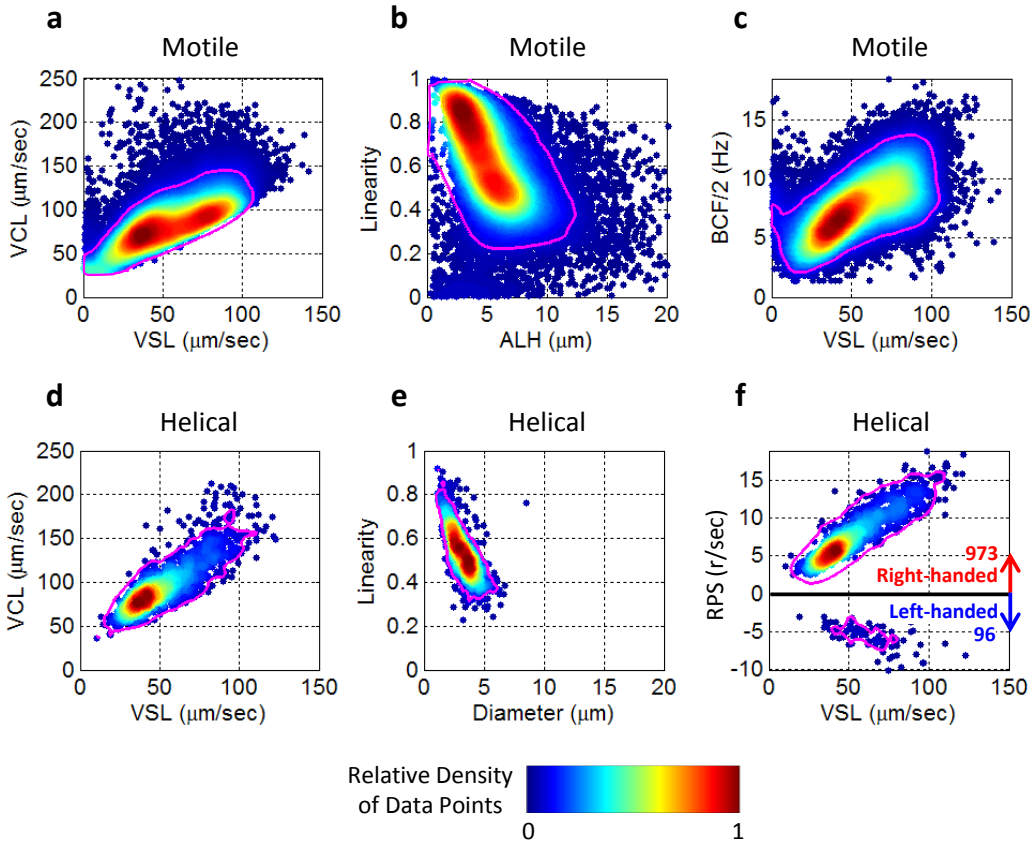

Figure 5-11 | Dynamic swimming parameters of 24,090 motile human sperms and 1,069 helical trajectories. Color-bar represents the relative density of data points in each graph. Magenta lines enclose 90% of the motile/helical tracks presented in each panel. A helix with RPS > 0 (RPS < 0) is defined as right-handed (left-handed). VSL: straight-line velocity. VCL: curvilinear velocity. ALH: amplitude of lateral head displacement. BCF: beat-cross frequency. RPS: rotation speed. r/sec: revolutions per second. These measurements were made in baseline medium (artificial HTF) after >2 hours of incubation as described in the Methods Section.

Straight-line Velocity (VSL) (μm/sec)	Curvilinear Velocity (VCL) (μm/sec)	Linearity (VSL/VCL)	Lateral Head Displacement (ALH) (μm)	Beat-cross Frequency (BCF) (Hz)
55.7 (±24.9)	88.0 (±28.7)	0.61 (±0.21)	5.4 (±2.9)	15.7 (±5.1)

(a) Motile Sperms

Straight-line Velocity (VSL) (μm/sec)	Curvilinear Velocity (VCL) (μm/sec)	Linearity (VSL/VCL)	Helix Diameter (μm)	Helix Pitch (μm)	Frequency of Rotation (RPS) (rev. per sec)
54.1 (±21.0)	99.1 (±30.3)	0.54 (±0.11)	3.2 (±1.0)	7.4 (±2.0)	6.8 (±4.6)

(b) Helical Trajectories

Table 5-3 | Typical values of various dynamic swimming parameters measured for human sperms. This Table shares the same data as in Fig. 5-11. All the error values in parentheses are ±s.d..

To shed more light on this observation (i.e., the preference of right-handed helices), I performed an additional experiment (Fig. 5-12) to measure the percentage of helical trajectories as a function of time after the sperms were removed from seminal plasma and were placed into baseline medium (see the Methods Section). The results of this time-traced experiment revealed that, after removal of the seminal plasma, the percentage of right-handed helical sperms significantly increased within 2-3 hours of incubation in baseline medium, reaching 4-5% of motile human sperms (see Fig. 5-12), which is also consistent with my previous observations in Fig. 5-11 and Table 5-1. On the other hand, the same experiment did not reveal any major changes in the left-handed helical sperm percentage as a function of time, which remained to be <0.5% even after >3 hours of incubation in baseline medium as illustrated in Fig. 5-12.

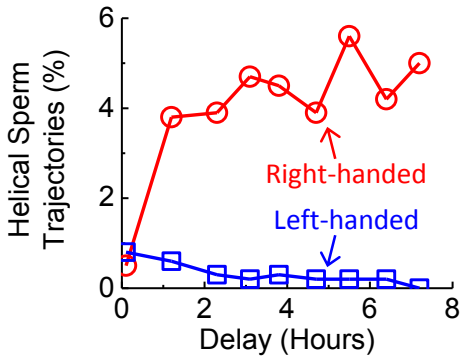

Figure 5-12 | Time evolution of helical sperm trajectories after re-suspension in artificial human tubal fluid (HTF). After 2-3 hours of incubation in HTF, the percentage of right-handed helical trajectories significantly increased to 4-5% of motile human sperms, while the percentage of left-handed ones did not show a major change, remaining to be <0.5% of motile sperms.

These results also suggest that seminal plasma significantly suppresses helical trajectories of human sperms, while human tubal fluid initiates them. An experimental comparison of how different concentrations of seminal plasma affect the 3D swimming patterns of human sperms (in specific helical and hyper-activated trajectories) is also provided in Fig. 5-13, which once again confirmed the suppressing effect of seminal plasma on helical trajectories (after >2 hours of incubation time - see the Methods Section for details). Another important observation is that the helical trajectories, compared to the hyper-activated ones, were more difficult to suppress by increasing the percentage of seminal plasma in medium (see Fig. 5-13), suggesting that these two swimming patterns might be regulated through different biochemical mechanisms.

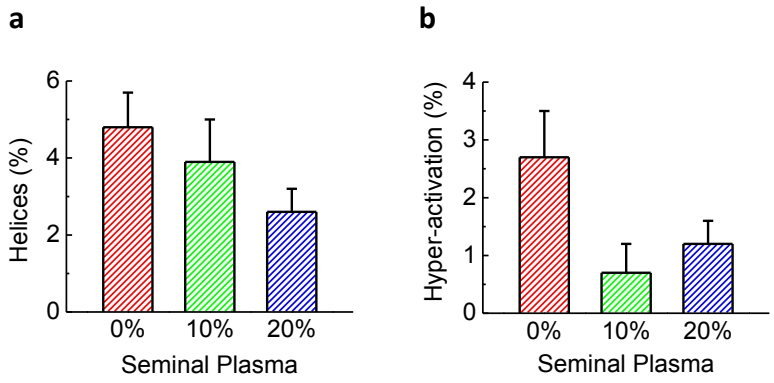

Figure 5-13 | Quenching of human sperms' helical (a) and hyper-activated (b) trajectories as a function of increased seminal plasma concentration in culture media. Each of the mean±s.d. bars in (a) and (b) was based on 14 measurements of 2 specimens (7 with each) obtained from different anonymous donors.

5.4 Discussion

It should be emphasized that to obtain large statistics regarding the swimming patterns of human sperms one would need a high-throughput imaging platform with sub-micron 3D tracking accuracy and sub-12-ms temporal resolution to clearly resolve different patterns, especially the helical patterns, which exhibit a tight helix radius of e.g., 0.5-3 μm with a fast rotation speed that might reach e.g., 15-20 rotations/sec. Conventional microscopes equipped with e.g., high-magnification objective lenses and high-frame-rate cameras can only meet these requirements for imaging sperms along a 2D plane, which can infer limited information on their natural 3D motion.[120–125,99,126–132] More advanced microscopy configurations[133–135] or holographic imaging schemes[136–143] have also been used to resolve 3D trajectories of sperms of *other* species. However, these previous approaches have not reported sub-micron 3D localization accuracy throughout a large observation volume of e.g., ≥1 μL. The dual-view partially-coherent holographic on-chip imaging technique described in this chapter uses a lensfree hologram recording configuration to image a large field-of-view of e.g., 17 mm^2 and utilizes a dual-angle illumination scheme to

achieve sub-micron localization accuracy for tracking human sperms within a volume of e.g., 8-17 μL. This high-throughput platform provides unique opportunities to observe the swimming patterns of human sperms and reveal their rare statistics for e.g., helical or hyper-helical trajectories, as summarized in the Results Section.

Surface accumulation of sperms inside an observation chamber is a common phenomenon that is observed when the chamber's depth is larger than the sperm's body length and has been the focus of several studies.[127,149–152] This was also observed in my results, happening on both the top and the bottom surfaces for all four swimming patterns (see Fig. 5-14). As described in the Results Section, the presence of the surface boundaries only modifies the typical and hyper-activated patterns but not the helical ones. Note that in my experiments, I used plain glass surfaces without siliconization to prevent electrostatic adherence of sperms. With different surface treatment methods, my platform can also be used to study how the surface properties can affect the statistics of sperm movement. Along the same lines, this lensfree sperm imaging platform can also provide a high-throughput tool to rapidly quantify the impact of e.g., various stimuli and drugs on the 3D swimming patterns of sperms.

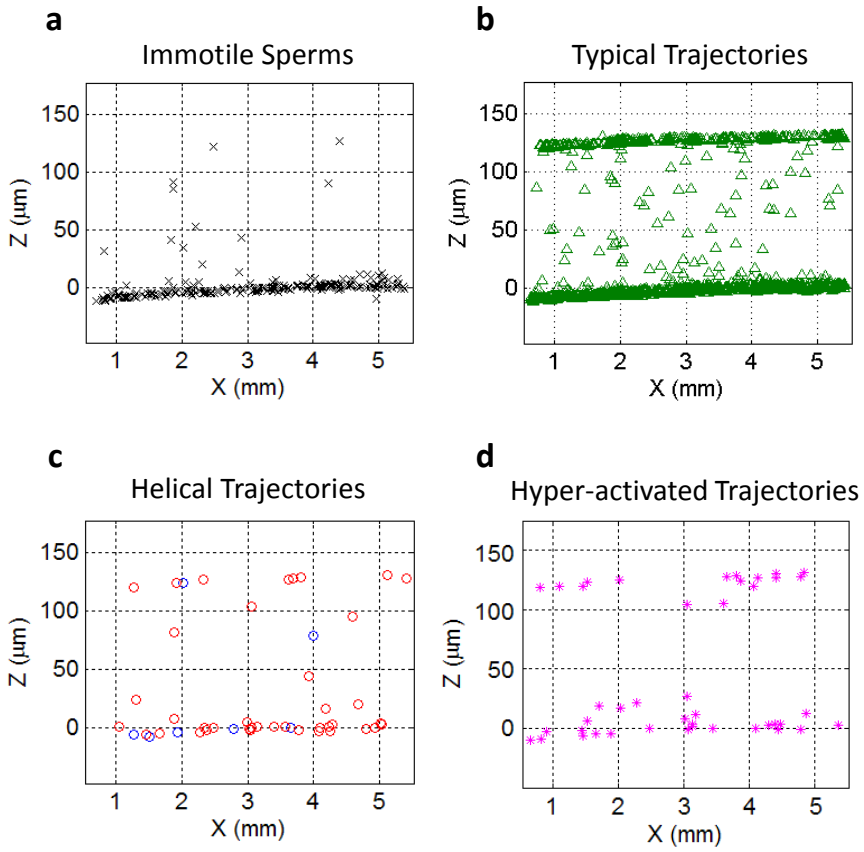

Figure 5-14 | Surface accumulation of human sperms in an observation chamber. The end positions of (a) immotile sperms, and the sperms with (b) typical swimming patterns, (c) helical swimming patterns (blue for left-handed ones and red for right-handed), (d) hyper-activated swimming patterns show that sperms of different swimming patterns all accumulate on either the top or bottom surfaces of the chamber. The Z = 0 reference plane of the imaging system was arbitrarily assigned to the center of the slightly tilted bottom surface of the observation chamber, whose position was verified by the distribution of the immotile sperms shown in (a).

5.5 Conclusion

Dynamic tracking of human sperms across a large volume is a challenging task. To provide a high-throughput solution to this important need, I developed a lensfree on-chip imaging platform which can track the three-dimensional (3D) trajectories of >1,500 individual human sperms within an observation volume of 8-17 mm^3. This computational imaging platform relies on

holographic lensfree shadows of sperms that are simultaneously acquired at two different wavelengths, emanating from two partially-coherent sources that are placed at 45 degrees with respect to each other. This dual-angle and dual-color illumination scheme permits dynamically tracking the 3D motion of human sperms across a field-of-view of >17 mm^2 and depth-of-field of 0.5-1 mm with sub-micron positioning accuracy. The large statistics provided by this lensfree imaging platform revealed that only 4-5% of the motile human sperms swim along well-defined helices and that this percentage can be significantly suppressed under seminal plasma. Furthermore, among these observed helical human sperms, a significant majority (~90%) preferred right-handed helices over left-handed ones, with a helix radius of 0.5-3 μm, a helical rotation speed of 3-20 rotations/sec and a linear speed of 20-100 μm/sec. This high-throughput 3D imaging platform could in general be quite valuable for observing the statistical swimming patterns of various other micro-organisms, leading to new insights in their 3D motion and the underlying bio-physics.

Chapter 6 Lensfree On-Chip Microscopy over a Wide Field-of-View using Pixel Super-Resolution

6.1 Introduction

Despite of its various advantages over the conventional Digital In-Line Holographic Microscopy (DIHM),[19,22,51] such as incoherent light source, large field-of-view, and easy alignment, the achievable numerical aperture (NA) of the lensfree holographic on-chip microscopy technique (LUCAS) presented in the previous chapters is significantly lower than the conventional DIHM technique (0.1-0.2 vs. ~0.5).

To achieve such a high numerical aperture in their reconstructed images, conventional DIHM systems utilize a coherent source (e.g., a laser) that is filtered by a small aperture (e.g., <1-2 μm); and typically operate at a fringe magnification of F > 5-10, where $F = (z_a+z_s)/z_a$; z_a and z_s define the aperture-to-object and object-to-sensor vertical distances, respectively. On the other hand, my LUCAS systems use an unusually large aperture (50-100μm diameter) and unit fringe magnification (F~1) to convert the whole active area of image sensors into the imaging field-of-view (FOV) for my holographic microscopes (see Chapter 3 for detailed discussion). However, the pixel size now starts to be a limiting factor for spatial resolution of my LUCAS technique since the recorded holographic fringes are no longer magnified. Because the object plane is now much closer to the detector plane (e.g., z_s ~1mm), the detection NA approaches ~1. However, the finite pixel size at the sensor chip can unfortunately record holographic oscillations corresponding to only an effective NA of 0.1-0.2, which limits the spatial resolution to <2μm.

In this chapter, I remove this limitation due to the pixel size to report lensfree holographic reconstruction of microscopic objects on a chip with a numerical aperture of ~0.5 achieving ~0.6

μm spatial resolution at 600 nm wavelength over an imaging FOV of ~24 mm^2. It should be emphasized that this large FOV can scale up without a trade-off in spatial resolution by using a larger format sensor chip since in my scheme the FOV equals to the active area of the detector array. To achieve such a performance jump while still using a partially coherent illumination from a large aperture (~50 μm) with unit fringe magnification, I capture multiple lower-resolution (LR) holograms while the aperture is scanned with a step size of ~0.1mm (see Fig. 6-1). The knowledge of this scanning step size is not required at all since I numerically determine the shift amount without any external input, using solely the recorded raw holograms, which makes my approach quite convenient and robust as it automatically calibrates itself in each digital reconstruction process. Because of the effective demagnification in my hologram recording geometry (z_a/z_s >100), such discrete steps in the aperture plane result in sub-pixel shifts of the object holograms at the sensor plane.

Therefore, by using a sub-pixel shifting based super-resolution algorithm I effectively recover much higher resolution digital holograms of the objects that are no longer limited by the finite pixel size at the detector array. Due to the low spatial and temporal coherence of the illumination source, together with its large aperture diameter, speckle noise and the undesired multiple reflection interference effects are also significantly reduced in this approach when compared to conventional high-resolution DIHM systems providing another important advantage.

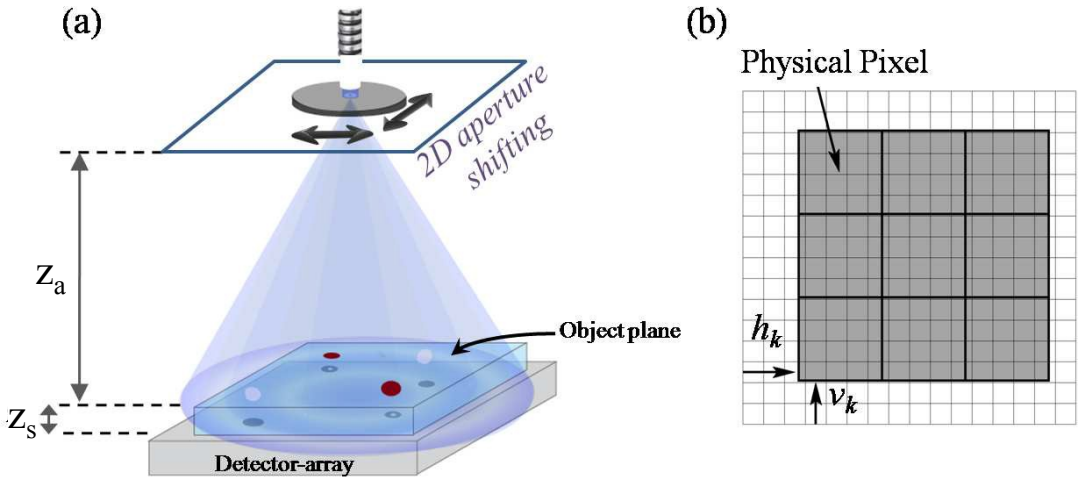

Figure 6-1 | (a) Schematic diagram of my experimental setup. The aperture to object distance is much larger than the object to detector distance (z_a~10 cm, z_s<1mm). A shift of the aperture causes a de-magnified shift of the object hologram formed at the detector plane, allowing sub-pixel hologram shifting. (b) Physical pixels captured in a single frame, here marked by bold borders, over imposed on the high-resolution pixel grid. This frame is shifted a distance of h_k horizontally and v_k vertically with respect to a reference frame.

6.2 Pixel super-resolution in lensfree digital in-line holography

As discussed in the introduction, with unit fringe magnification and low coherence illumination, my spatial resolution is limited by the pixel size, rather than the detection NA. Therefore, a higher spatial density of pixels is desirable to represent each hologram for reconstruction of higher resolution images. This can in principle be achieved by physically reducing the pixel size at the sensor to e.g., <1μm, which has obvious technological challenges to claim a large FOV. Therefore, in this manuscript I demonstrate the use of a pixel super-resolution approach to digitally claim 6 fold smaller pixel size for representation of each object hologram to significantly improve my spatial resolution over a large FOV achieving an NA of ~0.5.

Specifically, here I increase the spatial sampling rate of the lensfree holograms, and hence improve my spatial resolution by capturing and processing multiple lower-resolution holograms,

that are spatially shifted with respect to each other by sub-pixel pitch distances. As an example, I take a 5 megapixel image sensor that is used to record lensfree digital holograms with a pixel size of ~2.2μm, and effectively convert that to a 180 megapixel sensor with a 6 fold smaller pixel size (~0.37μm), that essentially has the same active area (i.e., the same imaging FOV). I term this technique as ***Pixel Super-Resolution*** (***Pixel SR***), to avoid confusion with the recent use of the term "super-resolution" describing imaging techniques capable of overcoming the diffraction limit.[2–4] Various Pixel SR approaches have been previously used in the image processing community to digitally convert low-resolution imaging systems into higher resolution ones, including magnetic resonance imaging (MRI), satellite and other remote sensing platforms, and even X-Ray computed tomography.[153–155]

The idea behind Pixel SR is to use multiple lower-resolution images, which are shifted with respect to each other by fractions of the low-resolution grid constant, to better approximate the image sampling on a higher resolution grid. In Fig. 6-1(b), the physical pixels are shown, bordered by thick lines, as well as the virtual higher resolution grid. For each horizontal shift h_k and vertical shift v_k of the lower-resolution image, the output of each physical pixel is simply a linear combination of the underlying high-resolution pixel values.

To better formulate Pixel SR, let us denote the lower-resolution (***LR***) images by $X_k(n1,n2)$, $k = 1,\ldots,p$, each with horizontal and vertical shifts h_k and v_k, respectively, and each of size $M = N1 \times N2$. The high-resolution (***HR***) image $Y(n_1,n_2)$ is of the size $N = LN_1 \times LN_2$, where L is a positive integer. The goal of the Pixel SR algorithm is to find the HR image $Y(n_1,n_2)$ which best recovers all the measured frames $X_k(n_1,n_2)$. The metric for the quality of this recovery is described below. For brevity in my notation, I order all the measured pixels of a captured frame in a single vector $\boldsymbol{X_k} = [x_{k,1}, x_{k,2}, \ldots, x_{k,M}]$, and all the HR pixels in a vector $\boldsymbol{Y} = [y_1,y_2,\ldots,y_N]$. A

given HR image $\boldsymbol{Y}$ implies a set of LR pixel values determined by a weighted super-position of the appropriate HR pixels, such that:

$$\tilde{x}_{k,i} = \sum_{j=1,\ldots,N} W_{k,i,j}(h_k, v_k) \cdot y_j \tag{6-1}$$

where $\tilde{x}_{k,i}$ denotes the calculated LR pixel value for a given $\boldsymbol{Y}$, $i = 1,\ldots,M$; $k = 1,\ldots p$ and $W_{k,i,j}$ is a physical weighting coefficient. I round all the frame shifts (h_k and v_k) to the nearest multiple of the HR pixel size. Therefore, a given LR pixel value can be determined from a linear combination of L^2 HR pixels (see Fig. 6-1). I further assume that the weighting coefficients $W_{k,i,j}$ (for a given k and i) are determined by the 2D light sensitivity map of the sensor chip active area and can be approximated by a Gaussian distribution over the area corresponding to the L^2 HR pixels.

In my Pixel SR implementation, the high-resolution image ($\boldsymbol{Y}$) is recovered/reconstructed by minimizing the following cost function, $C(\boldsymbol{Y})$:

$$C(\boldsymbol{Y}) = \frac{1}{2}\sum_{\substack{k=1,\ldots,p \\ i=1,\ldots,M}} \left(x_{k,i} - \tilde{x}_{k,i}\right)^2 + \frac{\alpha}{2}\left(\boldsymbol{Y}_{fil}^T \cdot \boldsymbol{Y}_{fil}\right). \tag{6-2}$$

The first term on the right hand side of Eq. (6-2 is simply the squared error between the measured low-resolution pixel values and the ones recovered from the virtual high-resolution image (see Eq. (6-1)). Minimizing this term by itself is equivalent to the maximum-likelihood estimation under the assumption of uniform Gaussian noise.[153] This optimization problem is known to be ill-defined and susceptible to high frequency noise. The last term of Eq. (6-2) is meant to regularize the optimization problem by penalizing high frequency components of the high-resolution image, where $\boldsymbol{Y}_{fil}$ is a high-pass filtration of the high-resolution image $\boldsymbol{Y}$, and α is the weight given to those high frequencies. For large α, the final high-resolution image would be smoother and more blurred, while for small α, the resulting image would contain fine details in

addition to high frequency noise. In this work, I used $\alpha = 1$ and a Laplacian kernel for high-pass filtering of $\boldsymbol{Y}$.[154]

As will be detailed in the following sections, my experimental setup handles sub-pixel shifting of lensfree holograms and the above described super-resolution hologram recovery algorithm over a large imaging FOV with ease and robustness due to the large demagnification inherent in its recording geometry.

6.3 Experimental setup

A schematic diagram of my setup is shown in Fig. 6-1, I use a spatially incoherent light source (Xenon lamp attached to a monochromator, wavelength: 500-600 nm, spectral bandwidth: ~5nm) coupled to an optical fiber with a core size of ~50μm, which also acts as a large pinhole/aperture. The distance between the fiber end and the object plane (z_a ~ 10cm) is much larger than the distance between the object and the detector planes (z_s ~ 0.75mm). My detector is a CMOS sensor with 2.2μm×2.2μm pixel size, and a total active area of ~24.4 mm^2.

The large z_a/z_s ratio, which enables wide-field lensfree holography and the use of a large aperture size, also makes sub-pixel hologram shifting possible without the need for submicron resolution mechanical movement. In other words, the requirements on the precision and accuracy of the mechanical scanning stage are greatly reduced in my scheme. Simple geometrical optics approximations can show that the object hologram at the detector plane can be shifted sub-pixel by translating the illumination aperture parallel to the detector plane. The ratio between the shift of the hologram at the detector plane and the shift of the aperture can be approximated as:

$$\frac{S_{hologram}}{S_{aperture}} = \frac{z_2}{z_1} \times \frac{n_1}{n_2}, \tag{6-3}$$

where $n_1 = 1$ is the refractive index of air, and $n_2 = 1.5$ is the refractive index of the cover glass before the detector array. For z_a = 10cm and z_s = 0.75mm, the ratio between these two shifts

become $S_{hologram}/S_{aperture} \sim 1/200$, which implies that to achieve e.g., 0.5 μm shift of the object hologram at the detector plane, the source aperture can be shifted by 200×0.5 = 100 μm. In the experiments reported here, I have used an automated mechanical-scanning stage to shift the fiber aperture and captured multiple holograms of the same objects with sub pixel hologram shifts. In principle, multiple sources separated by ~0.1 mm from each other that can be switched on-off sequentially could also be used to replace the mechanical scanning.

Using Eq. (6-3), the required aperture shift for a desired sub-pixel hologram shift can be calculated. Since the parameters in Eq. (6-3) may not be known exactly, and as a consistency check, I independently compute the hologram shifts directly from the captured lower resolution holograms, using an iterative gradient algorithm.[154] Therefore, quite importantly hologram shifts to be used in Eq. (6-2) and Eq. (6-3) are computed from the raw data rather than external input, which makes my approach quite convenient and robust as it automatically calibrates itself in each digital reconstruction process, without relying on the precision or accuracy of the mechanical scanning stage.

6.4 Experimental results

To quantify the spatial resolution improvement due to Pixel SR, I have imaged a calibration object consisting of 1μm wide lines etched into a glass cover slide (using focused ion beam milling), with 1μm separation between the lines (see Fig. 6-3(a)). This object is a finite size grating, and ideally it is a phase-only object, except the scattering at the walls of the etched regions.

Initially I used $L = 6$, i.e., the object holograms were shifted by one sixth of a pixel in each direction, for a total of 36 lensfree holograms. Fig. 6-2(a) shows one of these LR holograms captured at the detector. The sub-pixel shift amount of each LR hologram with respect to the first

LR hologram is calculated from the raw data without any additional input as shown in Fig. 6-2(b). The super-resolution hologram (see Fig. 6-2(c)) is generated by minimizing Eq. (6-2) using the Conjugate Gradient method,[156] incorporating all the captured 36 LR holograms. It is evident that the computed high-resolution hologram now captures the interference fringes which could not be normally recorded with a 2.2 μm pixel size. Next, I demonstrate how this super-resolution hologram translates to a high-resolution object reconstruction.

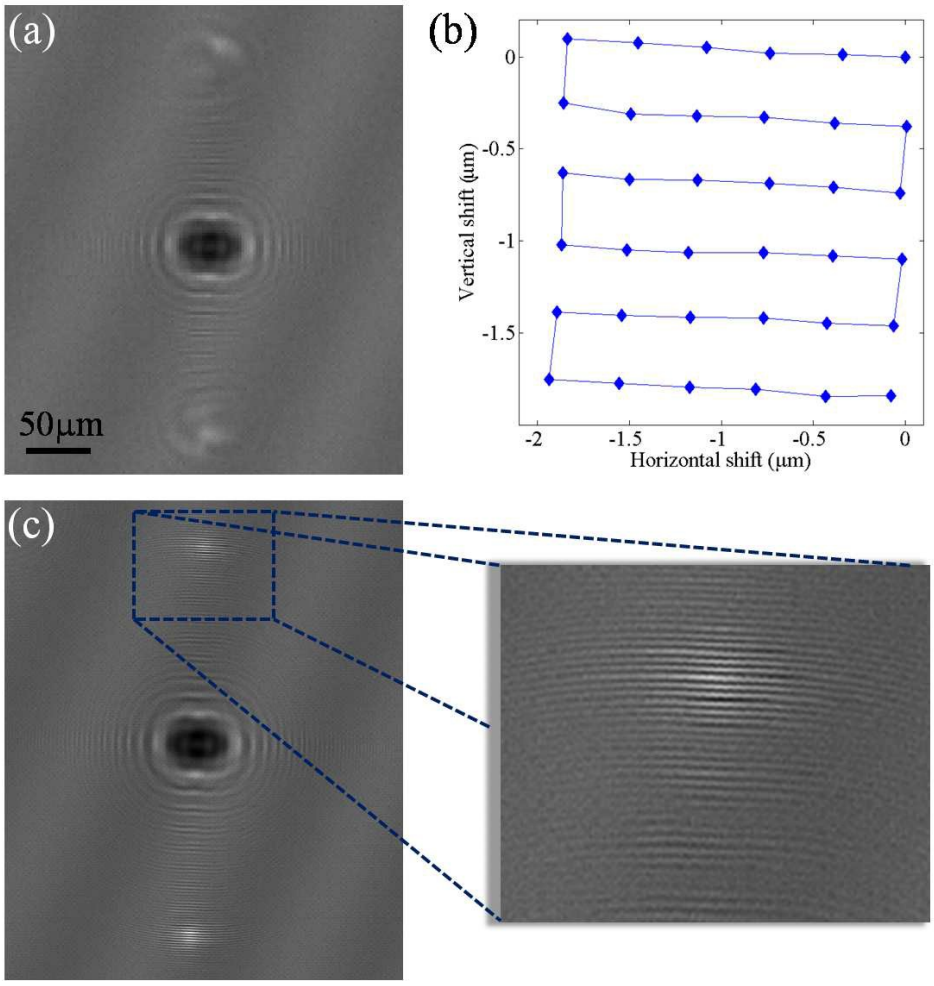

Figure 6-2 | Multiple sub-pixel shifted lower-resolution holograms of the grating object are captured. One such lower-resolution hologram is shown in (a). The sub-pixel shifts between different holograms are automatically computed from the raw data using an iterative gradient method, the results of which are shown

in (b). The Pixel SR algorithm recovers the high-resolution hologram of the object as shown in (c). The magnified portion of this super-resolution hologram shows high frequency fringes which were not captured in the lower-resolution holograms.

Given a lensfree hologram (whether one of the lower-resolution holograms or the super-resolution one), I reconstruct the image of the object, in both amplitude and phase, using an iterative, object-support constrained, phase recovery algorithm.[67] Accordingly, Fig. 6-3(b) shows the amplitude image that I obtain using a single lower-resolution hologram (shown in Fig. 6-2(a)). The inner features of the object are lost, which is expected due to the limited NA of the raw hologram (i.e., <0.2). Fig. 6-3(c) and (d) illustrate the amplitude and the phase images, respectively, recovered from the high-resolution hologram obtained from the Pixel SR algorithm (already shown in Fig. 6-2(c)). With the SR hologram, fine features of the object are clearly visible, and the object distinctly resembles the 40X microscope image shown in Fig. 6-3(a).

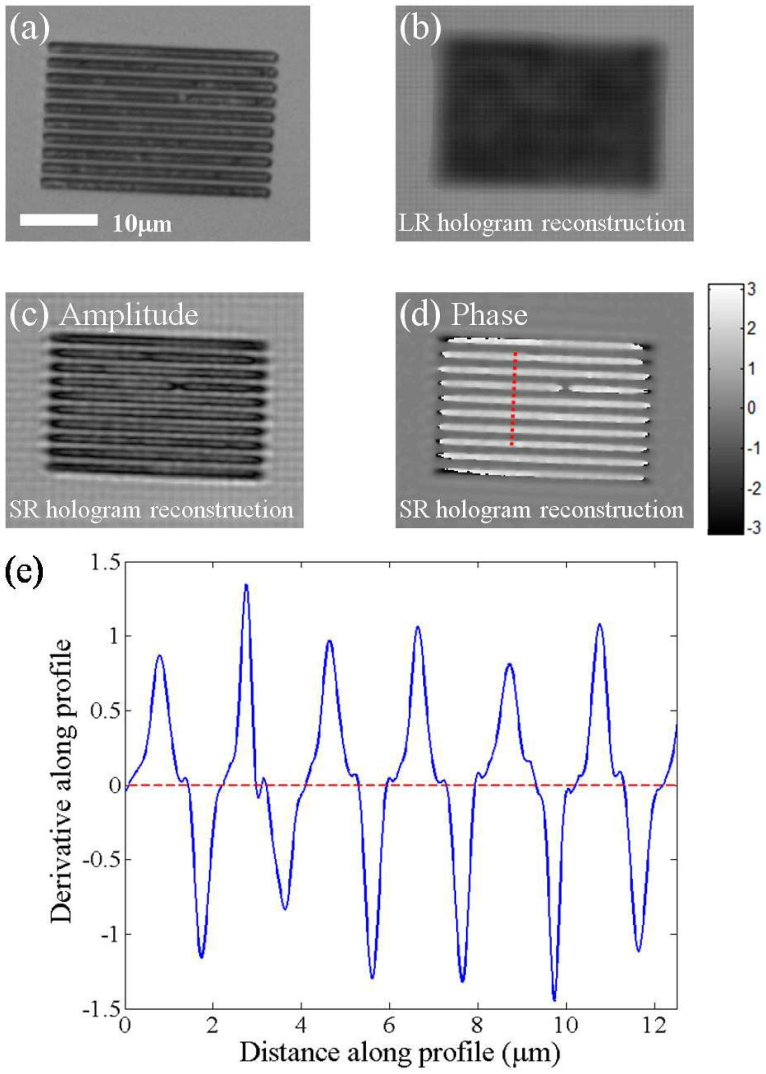

Figure 6-3 | (a) Microscope image of the object captured with a 40X objective lens (NA=0.65). (b) Amplitude reconstruction of the object using a single low-resolution hologram (see Fig. 6-2(a)). (c) Object amplitude reconstruction using the high-resolution hologram (see Fig. 6-2(c)) obtained from Pixel SR using 36 LR images. (d) Object phase reconstruction obtained from the same high-resolution hologram using Pixel SR. The object phase appears mostly positive due to phase wrapping. (e) The spatial derivative of the phase profile along the dashed line in pane (d). As explained in the text, this spatial derivative operation yields a train of delta functions with alternating signs, broadened by the PSF, which sets the resolution.

This grating object was made from indentations filled with air in glass, and therefore should have a negative phase. At the wavelength used in recording the raw holograms (600nm), the

object has a phase that is greater than π. This leads to phase wrapping, and the object's recovered phase appears to be mostly positive. Assuming that this grating object was fabricated with a rather fine resolution (which is a valid assumption since the patterning was done with focused ion beam milling with a spot size of <50 nm), in an ideal image reconstruction, the phase jumps on each line's edges would be infinitely sharp and impossible to unwrap. Therefore, I can use the reconstructed phase image at the edges of the fabricated lines to quantify the resolution limit of my Pixel SR scheme. Note that the recovered phase profile of the grating in a direction perpendicular to the lines, e.g., the dashed line in Fig. 6-3(d), should have sharp jumps with alternating signs. As a result, the spatial derivative of such a profile would consist of delta function with alternating signs. The limited spatial resolution of the imaging platform would broaden these delta functions by its point spread function (PSF). Therefore, if one were to examine the spatial derivative of the phase profile of the images, he would expect to see a series of the PSF with alternating signs. In Fig. 6-3(e), the spatial derivative of the phase profile is shown along the dashed line indicated in panel (d), interpolated for smoothness. The 1/e width of all the peaks shown in Fig. 6-3(e) is ≤ 0.6μm, which leads to the conclusion that the overall imaging resolution is ~0.6μm with an NA of ~0.5.

It is rather interesting to note that a similar performance could also be achieved with much less than 36 lower-resolution holograms (see Fig. 6-4). The pixel SR algorithm that I have implemented is an optimization algorithm, which may also work for underdetermined data sets, i.e., one can attempt to optimize the cost function (Eq. (6-2)) to recover the best high resolution hologram (with the same grid size) using less than $L^2 = 36$ LR holograms. Fig. 6-4 shows a comparison of the reconstructed high-resolution object images obtained by processing 5, 12, and 36 LR holograms. These LR holograms were selected from the full set of 36 sub-pixel shifted

holograms as shown in Fig. 6-4(d). The randomness of this selection process was slightly constricted by enforcing that each sub-set of holograms used by the Pixel SR algorithm would contain both the least shifted and the maximum shifted one in order to have well aligned images for accurate comparison. The super-resolution algorithm would perform equally well with complete randomness, but the comparison between different cases would then be less educative. As shown in Fig. 6-4, the reconstructed HR images are qualitatively the same for different numbers of LR holograms used, though the contrast is enhanced and the distortions are reduced as more LR holograms are used. I have also repeated the process of plotting the spatial derivatives of the recovered phase images perpendicular to the grating lines as shown in Fig. 6-4(e). The width of the derivative peaks (indicative of the spatial resolution in each recovery) did not appear to differ much as fewer number of LR holograms are used, which is quite encouraging since it implies that a small number of LR holograms, with random shifts, can be assigned to an appropriate HR grid to permit high-resolution lensfree image recovery over a large FOV. This should allow for great flexibility in the physical shifting and hologram acquisition process.

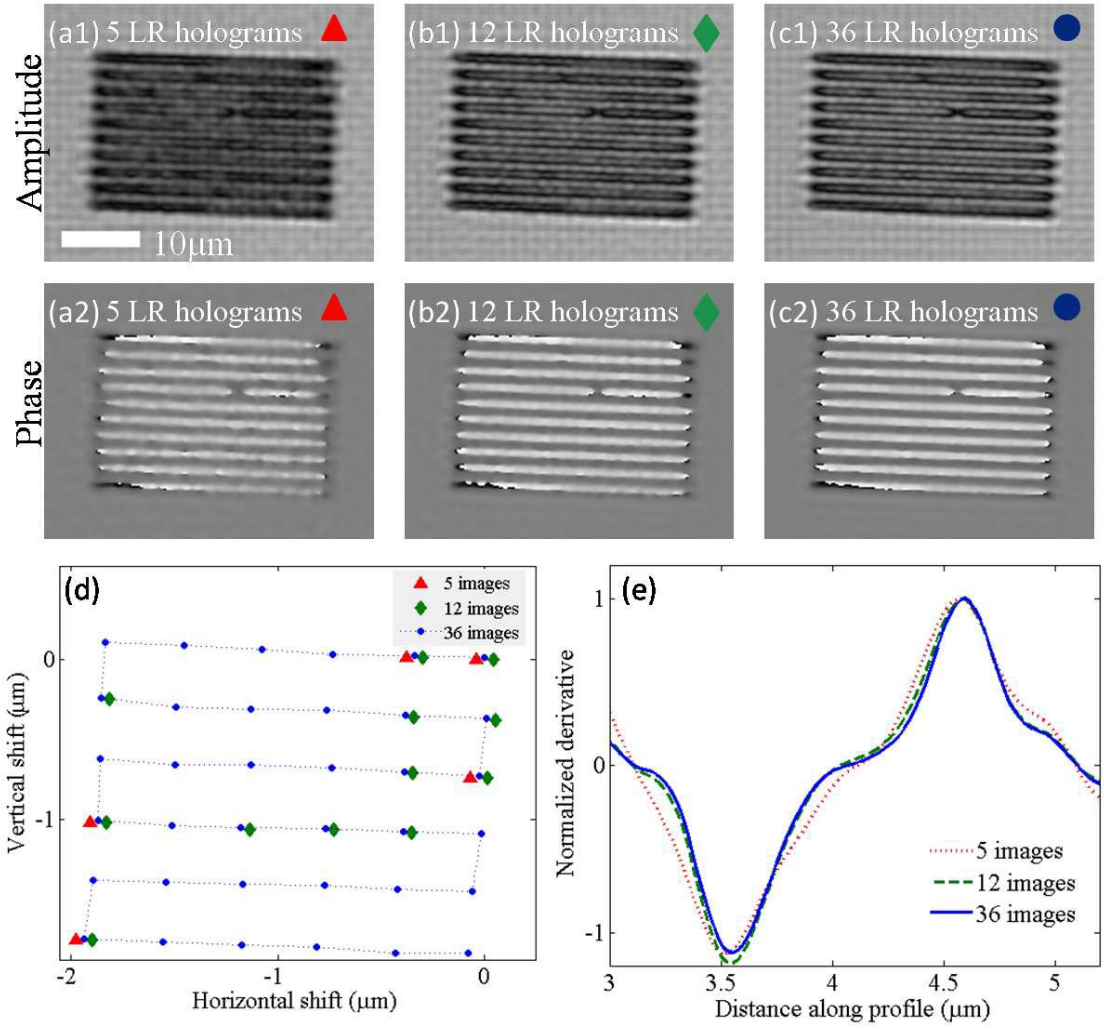

Figure 6-4 | Comparison of pixel SR recovery results using different numbers of LR holograms. Panels (a1-a2), (b1-b2), and (c1-c2) show the reconstructed amplitude and phase images of the same object using 5, 12, and 36 LR holograms, respectively. In (d), the sub-pixel shifts of the randomly chosen subsets of LR holograms are shown. In (e), the normalized spatial derivative profiles of the recovered phase images for each case (a2, b2 and c2) are shown, similar to Fig. 6-3(e).

Next, to demonstrate the wide-field imaging capability of my system, I applied the Pixel SR scheme to image a whole blood smear sample. In this experiment, a blood smear was created by smearing a droplet of whole blood on a cover glass to form a single layer of cells. The entire field-of-view (~24mm^2) is shown in Fig. 6-5 top image. I have used a source wavelength of λ =

500nm, and captured 36 sub-pixel shifted holograms. Different regions of the field-of-view are digitally cropped (see Fig. 6-5 - Regions A, B and C) to show the image improvement due to Pixel SR. The top row of Regions A-B-C is reconstructed using a single LR hologram. The middle row is obtained from processing 36 sub-pixel shifted holograms using my pixel-SR scheme. The images in the bottom row are obtained with a 40X microscope objective (0.65 NA) for comparison purposes. From Fig. 6-5, it is clear that Pixel SR allows resolving cell clusters which would be difficult to resolve from processing a single LR hologram. Also, the sub-cellular features of white blood cells are visibly enhanced as shown in Fig. 6-5, Region B.

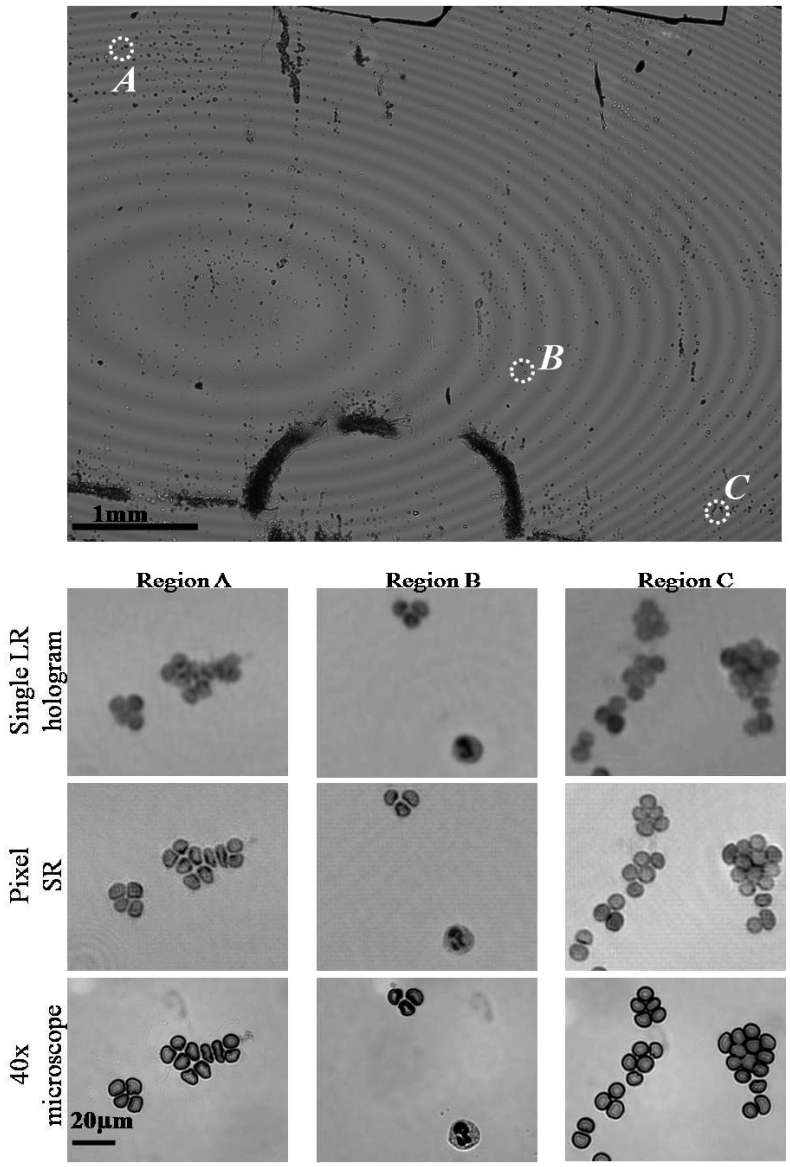

Figure 6-5 | Wide-field (FOV~24 mm2) high-resolution imaging of a whole blood smear sample using Pixel SR. A comparison among the image recovered using a single LR hologram (NA<0.2), the image recovered using Pixel SR (NA~0.5), and a 40X microscope image (NA=0.65) is provided for three regions of interest at different positions within the imaging FOV. Regions A and C show red blood cell clusters that are difficult to resolve using a single LR hologram, which are now clearly resolved using Pixel SR. In region B the sub-cellular features of a white blood cell are also resolved.

To display the capability to this lensfree holographic technique for resolving even more complicated biological samples, Fig. 6-6 shows Pixel SR results for imaging of *Caenorhabditis elegans* (*C. elegans*). These images were obtained by processing 16 sub-pixel shifted LR holograms captured at an illumination wavelength of λ = 500nm. Once again, the resolution improvement due to Pixel SR is clearly visible. Because my imaging system has a poorer axial resolution than a 40X microscope objective (NA=0.65), compared to the microscope image the Pixel SR image effectively shows a thicker z-slice of the *C. elegans* 3D body, which is almost a cylinder of ~25 μm diameter.

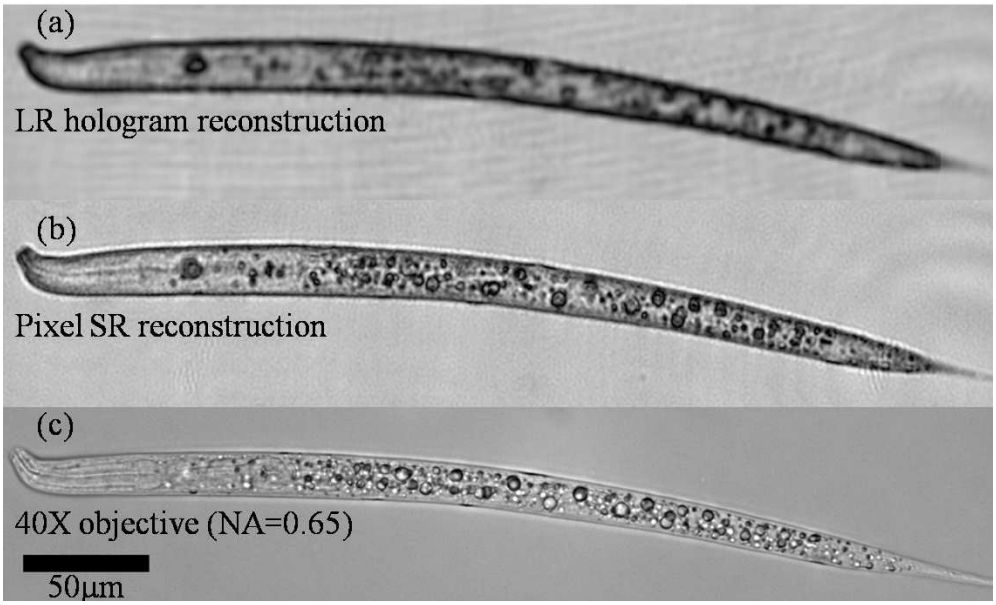

Figure 6-6 | Pixel super-resolution applied to imaging of *C. elegans*. (a) Recovered amplitude image from a single LR hologram. (b) Pixel SR image recovered using 16 sub-pixel shifted holograms. (c) Microscope image of the same worm captured with a 40X objective-lens (NA=0.65).

Such pixel super-resolution technique also permits my lensfree on-chip microscopy technique to generate an extreme space-bandwidth product, corresponding to a reconstructed image with e.g., more than one billion pixels. Using a state-of-the-art CCD image sensor (e.g.,

KAF-39000, Kodak) enables imaging an ultra-wide FOV of ~18 cm^2 with a half-pitch resolution of ~2.19 μm, which contains >1.5 billion effective pixels, assuming 2 pixels define the minimum feature size (see Fig. 6-7). In this case, the monochrome CCD chip itself has ~40 megapixels, where each pixel is physically ~6 μm wide. However, by employing pixel super-resolution, a deeply sub-pixel resolution corresponding to a numerical aperture of ~0.1 can be achieved across the entire active area of the CCD chip (i.e., an FOV of ~18 cm^2 – Fig. 6-7). In comparison, a conventional objective-lens with a similar NA would typically have an FOV that is a few square millimeters. While mechanical scanning of the sample or the objective-lens could be used to enlarge the imaging area, it would be a relatively complicated and costly solution to achieve such a wide imaging area of ~18 cm^2.

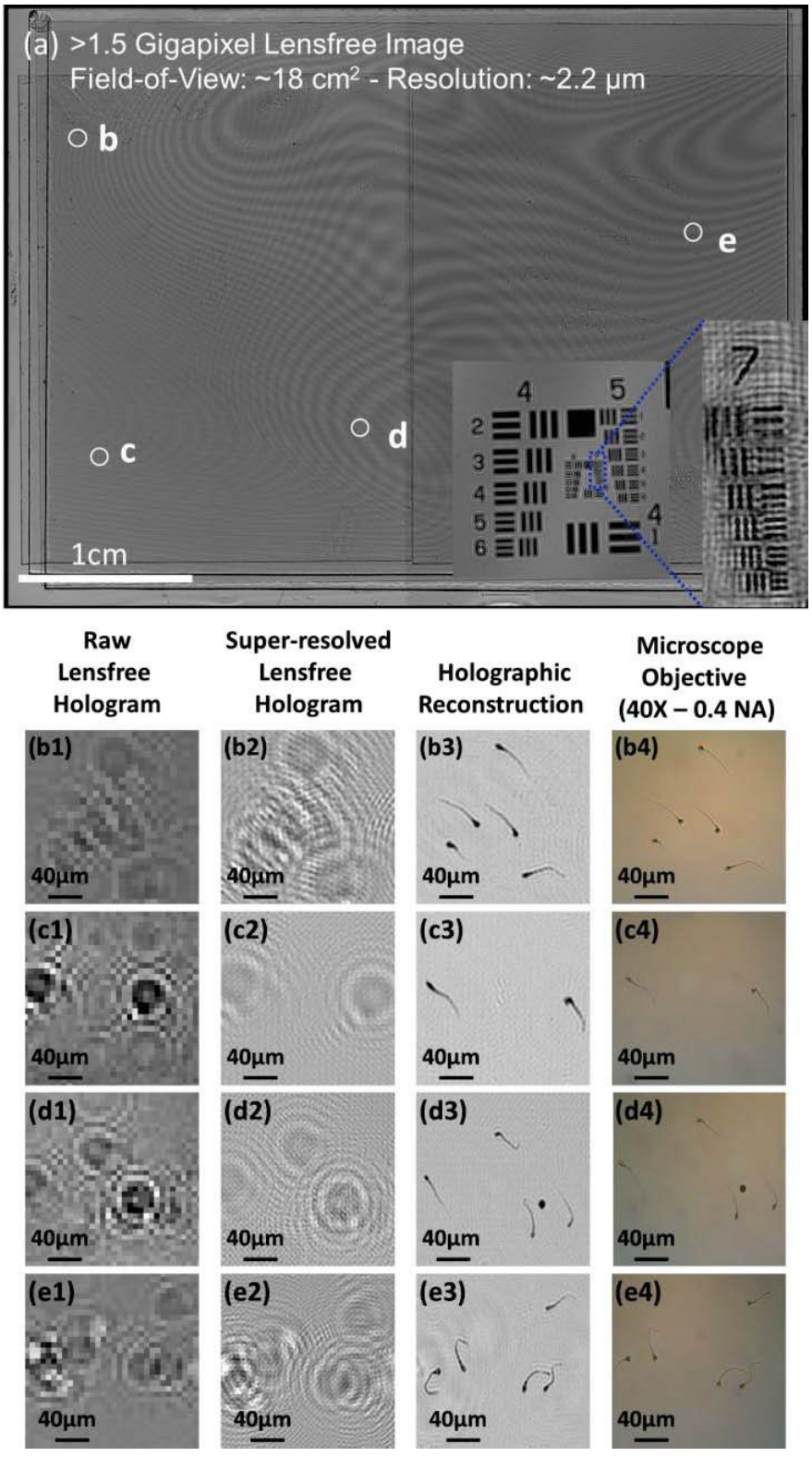

Figure 6-7 | Gigapixel holographic imaging enabled by pixel super-resolution. (a) A super-resolved lensfree image that has ~18 cm2 FOV is illustrated with >1.5 Billion pixels. The inset images in (a) show a USAF 1951

Test Chart to demonstrate a half-pitch resolution of ~2.19 μm across this FOV, corresponding to an NA of ~0.1. (b1-e1) show raw lensfree holograms of human sperms (immobilized on a glass slide) acquired with this partially-coherent lensfree imaging platform. Since the physical pixel size of this monochrome CCD chip is ~6 μm, severe under-sampling of holograms is observed. (b2-e2) show the pixel super-resolved lensfree holograms for the same regions as in (b1-e1), which are digitally synthesized by combining 36 (6x6) sub-pixel shifted raw lensfree holograms. (b3-e3) illustrate the reconstruction results for these pixel super-resolved lensfree holograms, which clearly show the tails of human sperms, providing a decent match to their corresponding conventional microscope images (40X objective lens, 0.4 NA), shown in (b4-e4).

6.5 Conclusion

In conclusion, I demonstrated lensfree holographic microscopy on a chip to achieve ~0.6 μm spatial resolution corresponding to a numerical aperture of ~0.5 over a large field-of-view of ~24 mm^2.[157] By using partially coherent illumination from a large aperture (~50 μm), I acquired lower resolution lensfree in-line holograms of the objects with unit fringe magnification. For each lensfree hologram, the pixel size at the sensor chip limits the spatial resolution of the reconstructed image. To bypass this limitation, I implemented a sub-pixel shifting based super-resolution algorithm to effectively recover much higher resolution digital holograms of the objects, permitting sub-micron spatial resolution to be achieved across the entire sensor chip active area, corresponding to an imaging field-of-view of ~24 mm^2. The success of this pixel super-resolution approach was demonstrated by imaging patterned transparent substrates, blood smear samples, as well as *C. Elegans*. By utilizing state-of-art high-pixel-count image sensors, such lensfree computational approach can further constitute gigapixel holographic imaging systems for biomedical applications with high-throughput requirements.

Chapter 7 Summary

To provide affordable and easy-to-use microscopes for resource-limited settings, here I developed a holographic on-chip imaging technology that utilizes cost-effective and compact optoelectronic components to enable digital recognition and microscopic imaging of cells with sub-cellular resolution over a large field-of-view (FOV) without the need for any lenses, bulky optical components or coherent sources such as lasers. Replacing optical lenses with digital computation, this partially-coherent cell imaging modality is very robust against mechanical misalignments, which eliminates potential imaging artifacts and the need for precision mechanics, making it highly suitable for field use.

Through experiments with whole human blood, I demonstrated that this lensless system can detect holograms of various cell types for digital recognition and automated counting of each cell type based on their 2D holographic signatures, as well as accurately reconstruct their microscopic amplitude and phase images with a resolution of 1-2 μm over a large FOV of 24 mm^2 even at cell densities up to 0.4 million cells/μL. With resolution and sensitivity that can differentiate between various white blood cell sub-types such as granulocytes, monocytes and lymphocytes, this lensless on-chip holography technology will be especially useful for point-of-care cytometry and diagnostics applications involving global health problems such as HIV, malaria, or infectious diarrhea.

Based on this technology, I also constructed an automated semen analysis platform based on a lensfree field-portable microscope that measures ~4×4×6 cm and weighs only 46 grams. With digital subtraction of consecutive frames quantifying the motion of motile sperms and summation of the same frames counting the density of immotile sperms, this computational

imaging platform can analyze >2,000 sperms over its 24 mm^2 FOV with an effective numerical aperture (NA) of ~0.2. Such a field-portable automated semen analysis platform has a great potential in personal male fertility test and animal breeding applications.

To analyze the three-dimensional (3D) motion of human sperms, I devised a dual-angle dual-color lensfree imaging scheme to achieve sub-micron accuracy and sub-12-minisecond resolution for tracking >1,500 sperms in a field-of-view of >17 mm^2 and a depth-of-field of >0.5 mm. The high accuracy and high throughput of this lensfree imaging platform enabled the first observation of human sperms' helical trajectories. The large statistics provided by this platform revealed that only 4-5% of the motile sperms swim along well-defined helices and that this percentage can be significantly suppressed by seminal plasma. Furthermore, a significant majority (~90%) of helical human sperms prefers right-handed helices with a helix radius of 0.5-3 μm and a helical rotation speed of 3-20 rotations/sec. Such a high-throughput 3D tracking platform can also a valuable tool for observing the statistical swimming patterns of various micro-organisms, leading to new insights in their 3D dynamics.

For the further improvement of the spatial resolution with this lensfree imaging technology, I acquired multiple stationary frames with various sub-pixel shifts and used a pixel super-resolution algorithm to synthesize a high-resolution holographic image. With digital reconstruction of images recorded with different image sensors, this technique can either achieve a spatial resolution of ~0.6 μm (NA~0.5) over a 24 mm^2 FOV for imaging fine sub-cellular structures, or provide ~1.5 billion effective pixels with ~2.2 μm resolution (NA~0.5) over a FOV of 18 cm^2 for high-throughput biomedical applications.

One of the most unique aspects of lensfree computational imaging is the fact that these quoted numbers will immediately improve as new sensor arrays become available on the market.

This rapid advancement that we experience in sensor array technologies is driven mostly by the cellphone and digital camera manufacturers, who produce more than 1 billion new camera modules every year, placing lensfree on-chip microscopy on a sweet spot to follow a rapid trend that is qualitatively similar to the Moore's Law in terms of its performance.

To conclude, the lensfree holographic on-chip imaging technology that I developed in this dissertation, as being compact, light-weight, cost-effective, high-throughput, and highly sensitive, can provide a powerful toolset for fighting against global health problems as well as advancing statistical studies in cell biology.

Appendix Multi-Angle Lensless Digital Holography for Depth Resolved Imaging on a Chip

A.1 Introduction

In this appendix, I review a multi-angle lensfree digital holography platform that can measure, with sub-micron accuracy, both the axial and the lateral position of any given cell/particle within an imaging field of view (FOV) of 20-60 mm^2.[115] The key to this high-throughput and accurate performance in a lensfree configuration is the use of multiple angles of illumination combined with a novel digital processing scheme.

Unlike conventional lensless in-line holography approaches, here I utilize spatially incoherent light sources emanating from large apertures (e.g., 50-100μm) with a unit fringe magnification, which enables an imaging field of view that is equivalent to the sensor chip active area.[57,67] In my hologram recording geometry, due to the use of incoherent sources and large apertures, the spatial coherence diameter at the sample plane is much smaller than the imaging field of view, but on the other hand is sufficiently large to record holograms of each cell/particle individually.[67] Under this condition, the vertical illumination creates lensless in-line holograms of the cells on the sensor chip. These digitally sampled cell holograms start to shift laterally on the sensor plane as the illumination angle of the source is tilted – for instance the cells at higher heights will shift laterally more than the cells located at lower heights (see e.g., Fig. A-1(a)). In the presented approach, the exact amount of this lateral shift of each lensfree cell hologram is calculated with an accuracy that beats the diffraction limit of light and therefore, by quantifying the amount of this lateral shift on the sensor array as a function of the illumination angle, I can determine the height of each cell from the substrate over a large field of view *without* the use of

any lenses. Such an accurate depth resolving capability when combined with the wide field of view of the presented approach may especially be significant for monitoring multi-layered microfluidic devices to improve the imaging throughput or for conducting micro-array imaging experiments to quantify e.g., on-chip DNA hybridization over a large field of view.[158]

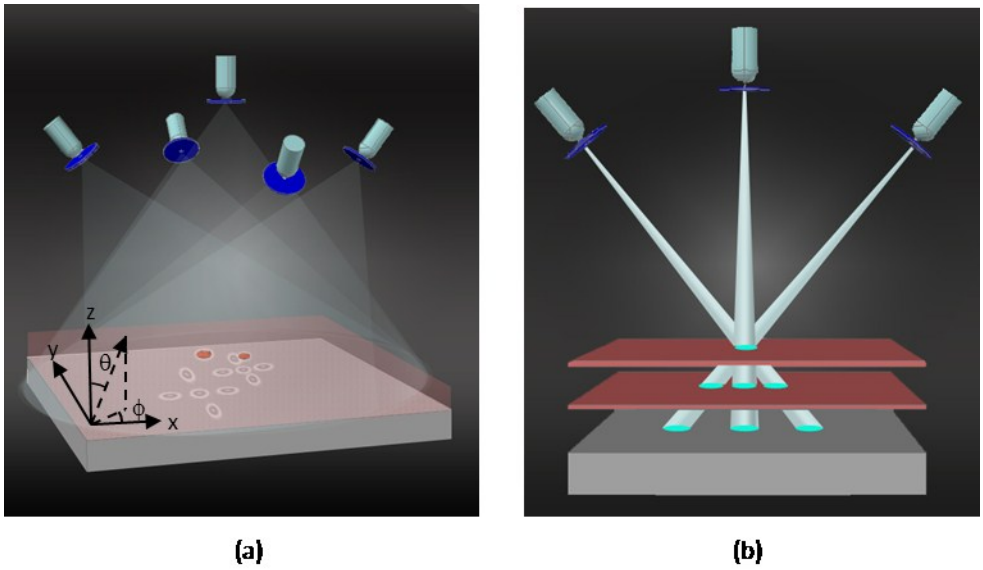

Figure A-1 | The schematic diagram illustrating the principles of multi-angle lensfree holographic imaging. For each illumination angle, a spatially incoherent source such as a light emitting diode is filtered by a large aperture (0.05-0.1mm diameter), which is placed ~6 cm away from the object plane. Note that unlike conventional in-line holography approaches, the sample plane is much closer to the detector plane with a vertical distance of ~1mm, such that the entire active area of the sensor becomes the imaging FOV. (a) The shadow of each cell shifts laterally on the sensor plane as a function of the illumination angle of the incoherent source, encoding its axial position. (b) Matching of the cells' shadows acquired at different illumination angles can be achieved by forming imaginary rays between each cell shadow and the corresponding source.

When compared to lens-based or coherent holographic imaging approaches[159–161] that also have a high localization accuracy, the overall hardware complexity of this multi-angle lensfree imaging platform is considerably simplified. Not only that there is no use of lenses or any other wavefront shaping elements involved in the presented approach, but also the source requirement is greatly simplified permitting the use of spatially incoherent light sources that are emitting through rather large apertures.

In this appendix, I will describe this multi-angle platform's hardware configuration, data processing procedures, and how its localization performance is compared to its theoretical limitation.

A.2 Depth resolved imaging using multi-angle lensless holography

The details of the depth resolved imaging process using multi-angle lensfree holography is summarized in Fig. A-2 After the capture of the multi-angle lensfree holographic images of the sample volume as illustrated in Fig. A-1(a), each one of these raw holograms is then processed using an iterative twin image elimination and phase recovery technique,[67,70,72] which can reconstruct amplitude and phase images of different cross sections of the sample volume. As a result of this numerical reconstruction process, this platform can distinguish overlapping lensfree holograms of the cells from each other and therefore increase the workable density of the cells compared to the earlier reported lensfree imaging technique[67] (see also Chapter 2).

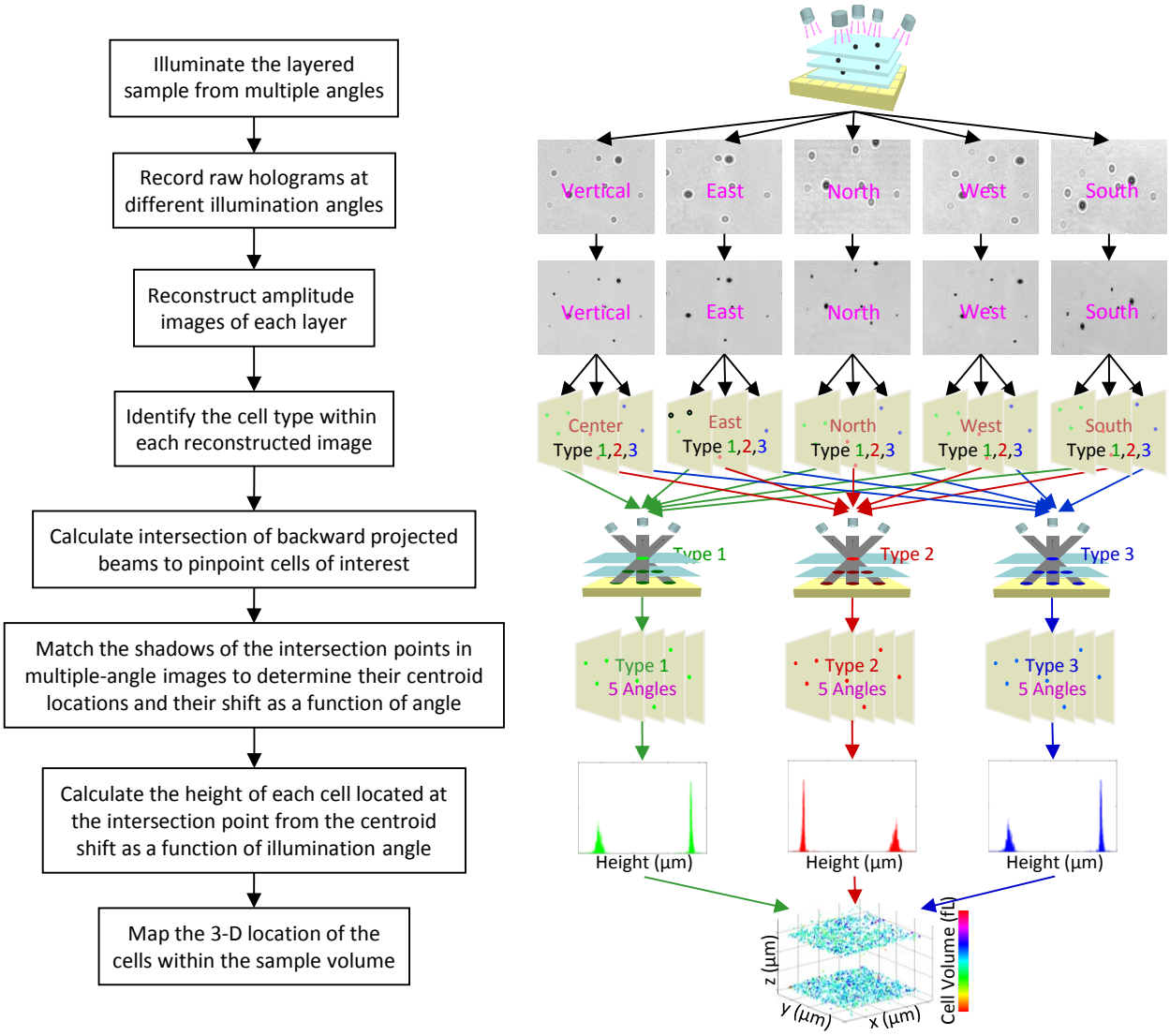

Figure A-2 | The detail of the depth resolved imaging process using multi-angle lensfree holography.

Before calculating the 3D location of each micro-object within the sample volume of interest, the coarse locations and the types of the objects need to be identified in each lensfree image. For this purpose, automated pattern matching algorithms[57] are used to identify the target objects within each lensfree image yielding the relative x-y coordinates of each object of interest. Repeating this automated identification with a statistical image library of different target cell types, this platform digitally sorts out the cell mixture by cell types without extra manipulation

measures. This initial screening step ensures that the depth calculations can be limited to *only* the cells of interest and the rest of the undesired micro-objects can simply be ignored. For this purpose the raw holograms and/or the reconstructed amplitude images of the cells can be used as long as the individual patterns are not severely overlapping.

Following this pre-screening process, imaginary rays (with a finite cross-section for each ray) are digitally formed by connecting the light source position to the rough x-y coordinate of the shadow or the reconstructed image of each target cell within the imaging field of view (see Fig. A-1(b)). These solid rays, which are calculated for all the illumination angles (including the vertical one), are then combined to find their intersection points in 3D, where the total count of the intersecting rays at any given point is also recorded. To provide a rough estimate for the position of each target cell type within the 3D sample volume, a threshold is applied to this ray count – for instance under 5 different illumination angles a ray threshold of 3 implies that at least 3 rays can define a positive count towards a target cell type. More discussion on the effect of this threshold factor on characterization accuracy is provided in section A.6. The localization accuracy of this initial interception algorithm is determined by the cross-sectional width of the rays that are used for back-projection of each shadow (Fig. A-1 (b)), and is practically on the order of ~5 μm. To achieve a much better depth accuracy (<1 μm) for each target micro-object within the sample volume, an additional calculation step is required, which will be discussed next.

At the end of the above discussed calculation step, for each one of the intersection points (that have a sufficient ray count above the threshold), all the shadows of the same cell at different illumination angles become digitally connected to each other. In some cases, if there is severe overlap between different shadows, some of these lensfree multi-angle images cannot be used.

This, however, does not pose a limitation for my depth localization algorithm since 2 independent angles in principle would be sufficient to localize the depth of the micro-object with submicron accuracy, i.e., there is redundancy in the system to better handle dense cell solutions. This also implies that for a less dense solution of interest, fewer angles (for instance 2-3) would also be sufficient. More discussion on the effect of the cell density on characterization accuracy is provided in section A.6.

Following these initial steps, the fine axial position of each target object needs to be calculated all across the sample volume. Considering the fact that there is no fringe magnification or a lens involved in the presented approach and that the pixel size at the sensor chip is relatively large (i.e., a few microns), this task seems rather challenging. The key to achieve sub-micron depth localization accuracy over a large field of view is to accurately calculate the lateral shift of each one of the multi-angle shadows/holograms corresponding to the same cell. Since the earlier numerical steps already connected the multi-angle holograms of the same cell to each other, all one needs to do next is to accurately calculate the lateral shift amount of the cell hologram as a function of the illumination angle. This step involves calculation of the centroid location of each cell with an accuracy that is much better than the diffraction limit of light. The difference between the centroid locations of at least 2 shadows acquired under different illumination angles is sufficient to accurately estimate the relative heights of all the cells within the sample volume. Next, I will discuss the details of these centroid calculations for each acquired cell shadow.

A.3 Centroid calculations for lensfree depth localization of cells on a chip

Accuracy of depth localization is achieved by calculating the centroid location of each cell's shadow/hologram, and determining the relative shift of the centroid position of the same cell as a

function of the illumination angle. For this approach to work effectively, the cell holograms should exhibit minimum amount of overlap such that their centroid calculations remain accurate. While dealing with high cell densities (such as >10,000 cells/μL) there are two factors that help one maintain a good depth localization accuracy: (*1*) The amplitude reconstruction process enables resolving highly overlapping cell shadows from each other. This permits digital removal of the undesired effects of the other cell shadows on the centroid calculation of each target cell type. And (*2*) there is redundancy in the measurements such that if one illumination angle produces an overlap for certain cell shadows (which cannot be fully resolved by the amplitude reconstruction process), then the other illumination angles can still remain free from overlaps. All one needs is 2 independent illumination angles where the centroid of the same cell shadow can be calculated accurately for achieving depth localization.

Assuming that I_{ij} represents the cell hologram or its reconstructed amplitude image, and (i, j) denotes the pixel numbers, initially I subtract a linearly fitted background image (I_{Bij}) from I_{ij} such that $p_{ij} \equiv I_{ij} - I_{Bij}$ is calculated. This background profile (I_{Bij}) is automatically calculated for each illumination angle through linear regression analysis of I_{ij} and it serves to minimize the undesired effects of (1) non-uniform illumination of the sample volume and (2) the surface curvature and/or tilt of the substrates on the depth localization accuracy of the cells. This step is crucial especially for achieving accurate depth localization over a large FOV as illustrated in Fig. 3. Following this background subtraction step, the centroid coordinates (x_c, y_c) of each cell are calculated as such:

$$\begin{cases} x_c = \dfrac{\sum_{ij} x_{ij} n_{ij}}{\sum_{ij} n_{ij}} \\ y_c = \dfrac{\sum_{ij} y_{ij} n_{ij}}{\sum_{ij} n_{ij}} \end{cases}, \tag{A-1}$$

where $n_{ij} \equiv p_{ij}^2$ is the square of the subtracted intensity.

For each target cell within the imaging field of view, the choice of the region of interest (ROI) to define I_{ij} is made through a fast iterative algorithm such that the centroid coordinates (x_c, y_c) eventually match with the geometric center of the ROI for each cell signature. At each step of this iterative algorithm, the center of the ROI was shifted to the position of the calculated centroid and the same centroid calculation was repeated until their positions matched with each other.

After the calculation of all the centroid coordinates of a target cell type under different illumination angles, the lateral shift of each cell's signature was calculated by taking the difference of the centroid coordinates. This lateral shift was then transferred into a projected height with a known oblique illumination angle, where the angle was already calibrated by a glass substrate with a measured thickness. Due to the non-uniformity of the illumination light and the surface curvature and/or tilt of the substrates, these projected height values needed to be further corrected by a quadratic surface fitting. The same process was performed separately with all the oblique illumination angles, and then these corrected height values from different angles were averaged to accurately determine the axial position (i.e., the z coordinate) of each cell within the sample volume. As for the lateral location (i.e., the x-y coordinates), the centroid coordinates calculated on the lensfree image with the vertical illumination was used without further modification.

A.4 Experimental results

To validate the depth resolving performance of my multi-angle holographic imaging platform over a large field of view of ~60 mm^2, I conducted an experiment with a mixture of 5, 10 and 20 μm diameter polystyrene beads (Monosized microsphere size standards, Thermo Scientific) suspended in DI water. The micro-particle suspension liquid was dispensed on a 0.5 mm thick glass substrate and covered by a No.1 glass cover slip (~150 μm thick) as shown in Fig. A-3(m). To quantify the accuracy of my axial localization results over the entire imaging area of the sensor, before being imaged, the samples were kept still for >10 minutes, allowing the suspended micro-particles to fully settle on the substrates. This ensured that the recovered height (i.e., the axial position) of the particles can be related to the well-controlled radii of the micro-particles, enabling cross validation of my results. During this settlement time period, holograms of the samples were periodically recorded using the vertical illumination to track the trajectories of individual particles. These trajectories were then analyzed to ensure that the displacement had decreased to a stable level (below the Brownian motion limit).

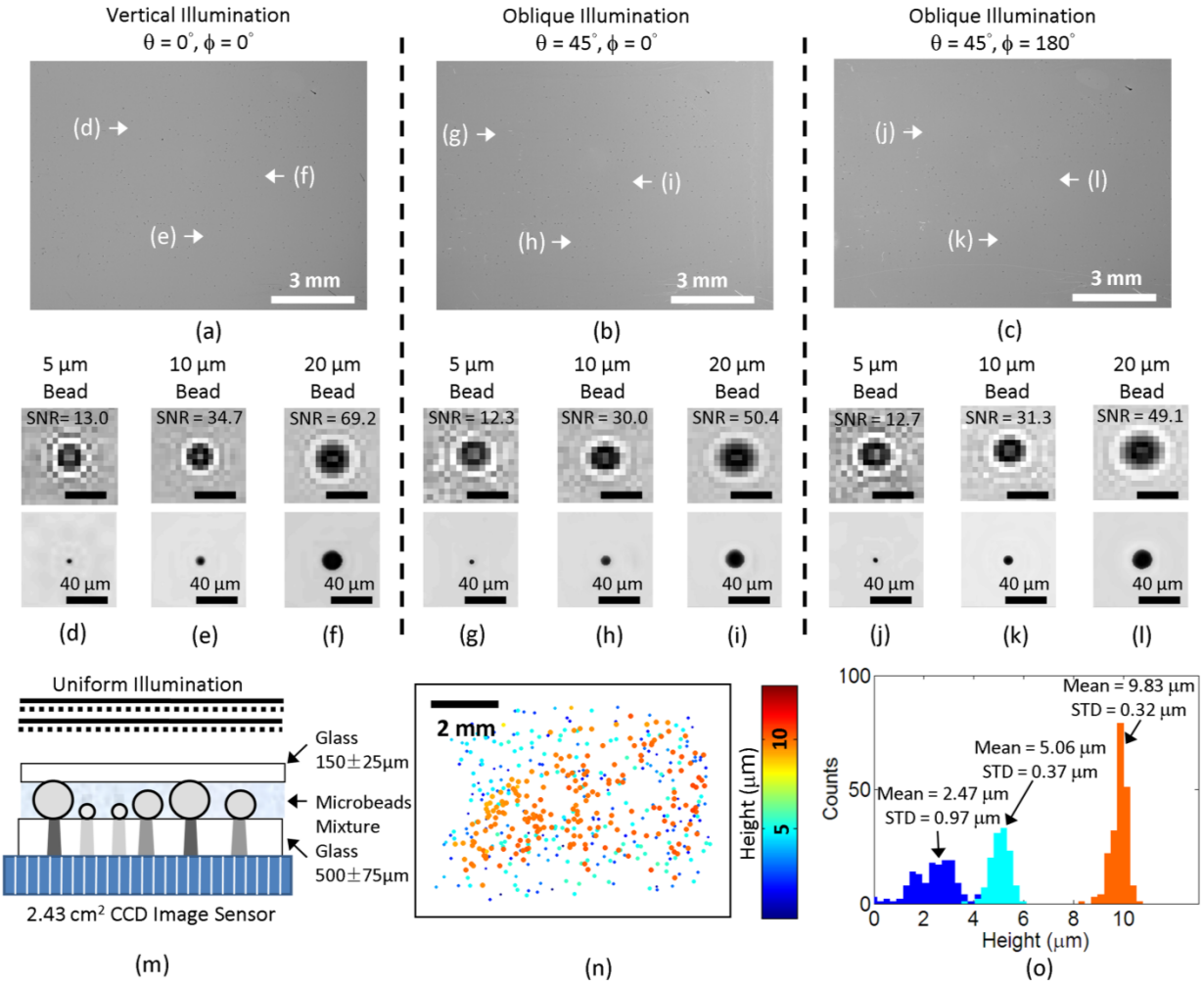

Figure A-3 | The validation of sub-micron localization performance over a large field of view of ~60 mm2. (a-b-c) Lensfree holograms captured with three different illumination angles are illustrated. (d-e-f) Raw hologram signatures (digitally cropped from the vertical illumination hologram shown in (a)) and their corresponding reconstructed amplitude images for (d) 5 µm, (e) 10 µm, and (f) 20 µm microbeads are illustrated. (g-h-i) Raw hologram signatures (digitally cropped from the oblique illumination hologram shown in (b)) and their corresponding reconstructed amplitude images for (g) 5 µm, (h) 10 µm, and (i) 20 µm microbeads are illustrated. (j-k-l) Raw hologram signatures (digitally cropped from the oblique illumination hologram shown in (c)) and their corresponding reconstructed amplitude images for (j) 5 µm, (k) 10 µm, and (l) 20 µm microbeads are also illustrated. The scale bars in (d-l) are 40 µm long. (m) The cross-sectional structure of the imaged sample is shown. (n) The 2-D distribution of the characterized microbeads is illustrated, with their physical size and the relative height coded by the spot size and the colormap,

respectively. (o) The height histogram is calculated from (n) showing three distinct peaks for the 5 μm, 10 μm, 20 μm beads in the mixture. In (n) and (o), the relative height of the substrate surface is arbitrarily assumed to be 0 μm.

To record the digital holograms of the micro particles distributed over ~60 mm^2 field-of-view and their lateral shifts as a function of the illumination angle, three optical fibers with a core diameter of 50 μm each were utilized to illuminate the sample placed on the bare surface of a CCD image sensor chip with a pixel size of 5.4 μm (KAF-8300, Kodak). The protective glass of the sensor chip has been removed to minimize the distance between the sample and the sensor surface and maximize signal-to-noise ratio of the lensfree holograms. The fibers are individually butt-coupled to three cyan light-emitting diodes (LEDs, LXHL-LE3C, Luxeon) and their tips are placed approximately 6 cm away from the sample to provide one vertical and two other tilted illuminations with (ϕ=0°; θ=45°) and (ϕ=180°; θ=45°) as illustrated in Fig. A-1. The center wavelength of the LEDs is 505 nm and the FWHM spectral width is ~30 nm.

Lensfree height characterization results of these particles are summarized in Fig. A-3, in which Figs. A-3(a)~(c) illustrate the raw lensfree holograms that are captured under each illumination angle over an imaging FOV of >1 cm^2. Smaller Figs. A-3(d)~(l) focus on the individual holographic signatures, digitally taken from Figs. A-3(a)~(c); and the reconstructed amplitude images (created by iterative holographic reconstruction[67]) of these representative particle holograms are also shown under different illumination conditions. As expected, in these figures the raw holograms of the tilted illumination conditions show an elongated texture, parallel to the tilt direction. Based on digital processing of these multi-angle lensfree holograms as described in the previous section, I recovered the height distribution of the micro-particles from the substrate surface as illustrated in Fig. A-3(n), where for convenience the relative height

of the substrate surface is assumed to be 0 μm (the physical size and the height of the particles are coded by each spot size and the colormap, respectively). Fig. A-3(o) also reports the height histogram calculated from Fig. A-3(n), which clearly resolves 3 different particle types from each other based on their relative heights (i.e., radii). These results are in close agreement with the height values that one would expect from the radii of these particles, i.e., 10 μm, 5 μm and 2.5 μm, respectively. One could attribute the differences between my characterization results (9.83, 5.06 and 2.47 μm) and the known radii of the particles (10, 5 and 2.5 μm) to the unavoidable surface curvature of the substrate over the large imaging field of view (~60 mm^2) and to the standard deviation of the particle radii, which is reported by the manufacturer (Thermo Scientific) to be ±1% for each particle type. The relatively worse performance (with a standard deviation of 0.97 μm) of the smaller sized particle (5 μm) is related to a reduced hologram signal-to-noise ratio (SNR) (refer to the individual hologram signatures and the SNR values that are provided in Fig. A-3(d-l)). This is also a topic that I will also address in section A.5.

I further validated my multi-angle lensless holography approach by imaging a two-layered micro-channel containing red blood cells (RBCs) (see Fig. A-4(f)). Whole blood samples were mixed with the anticoagulant EDTA at a ratio of 2 mg of EDTA per ml of blood (EDTA tubes, BD). The blood was kept still for ~20 minutes until the RBCs settled. After sedimentation, RBCs were extracted from the bottom of the sediment and diluted with cell culture medium (RPMI 1640, Invitrogen) to a concentration of ~15,000 cells/μL. A small number of polystyrene microbeads with a diameter of 20 μm were then added to the suspension (~40 beads/μL), serving as mechanical spacers in the multi-layer structure shown in Fig. A-4(f).

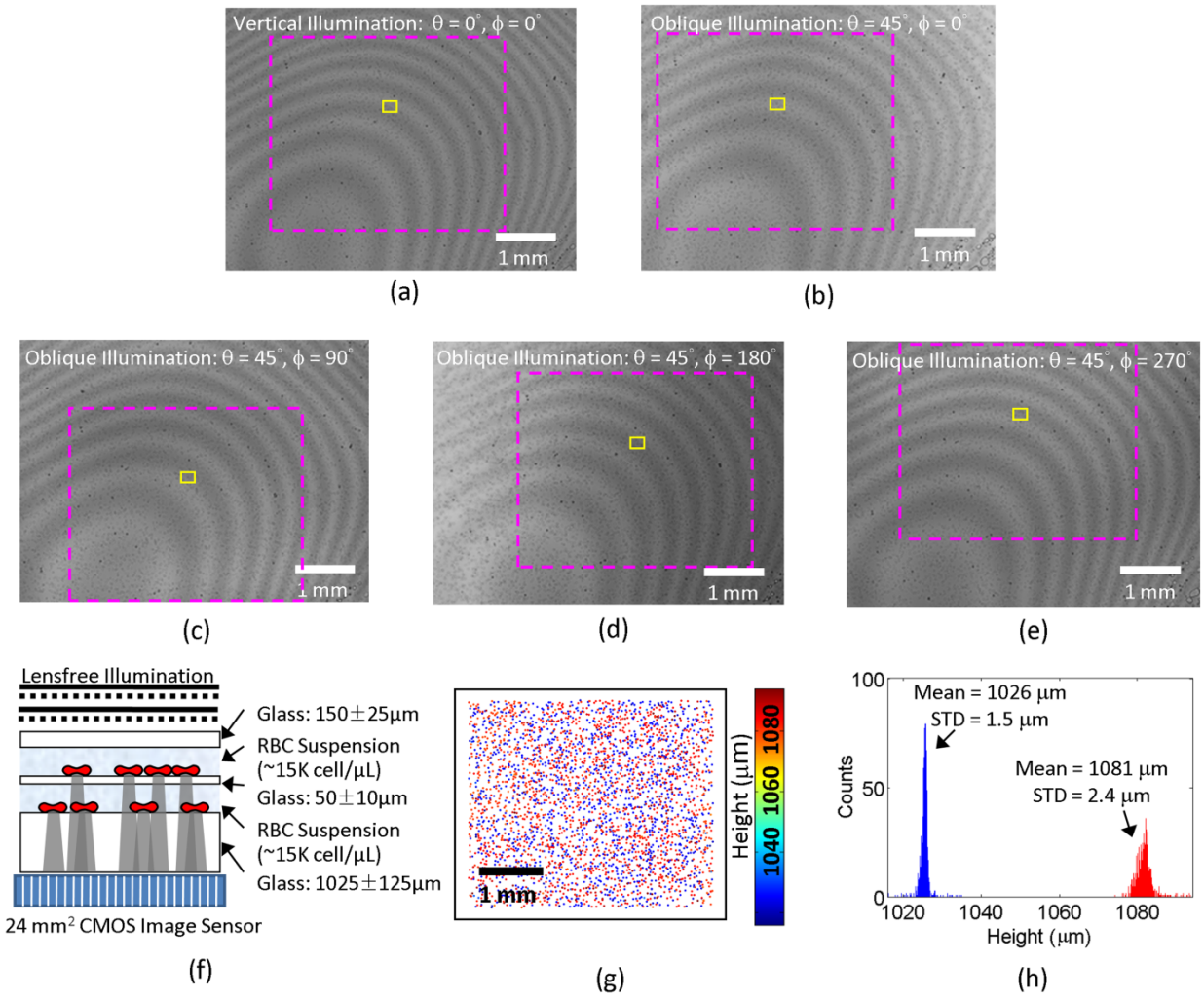

Figure A-4 | Lensless multi-angle characterization of RBCs located within two-layered micro-channels. (a)-(e) Lensfree holograms are captured with five different illumination angles. The magenta dashed rectangles in (a)-(e) are the regions corresponding to the field-of-view shown in (g); and the yellow rectangles define the regions corresponding to the field of view of the images in Fig. A-6. (f) The cross-sectional structure of the 2-layered sample is shown. (g) The 2D distribution of the RBCs located in both vertical channels is calculated with their height coded by the colormap. (h) shows the histogram of the cell heights over the entire field of view, which exhibits a double peaked behavior, as expected, resolving the 2 vertical micro-channels. In (g) and (h), the relative height is arbitrarily assumed to be 0 μm at the surface of the sensor.

The holograms of the cells were recorded by placing the samples directly on the image sensor chip as shown in Fig. A-4(f). A CMOS image sensor with a pixel size of 2.2 μm and an

active area of 24.4 mm^2 (MT9P031, Aptina) was used for imaging the RBC suspension sample. After settlement for >10 minutes, the samples were illuminated from different angles *sequentially* and the lensfree holograms with different illumination angles were recorded separately as illustrated in Fig. A-1. Alternatively, this image acquisition process could also be done in parallel by turning all the multi-angle sources on at the same time rather than sequentially. However the overall density of cells that can be imaged with parallel illumination is lower than sequential imaging, which is further quantified in section A.6.

To generate these lensfree cell holograms with different illumination angles, five optical fibers with a core diameter of 50 μm each were mounted with their tips approximately 6 cm away from the samples. Except the vertical illumination case, the illumination angles were 0°, 90°, 180° and 270° azimuthally and the polar angles were all 45° from the normal direction of the imaging plane, as shown in Fig. A-1.The fibers are connected to a Xenon lamp (6258, Newport Corp.) filtered by a monochromator (Cornerstone T260, Newport Corp.), where the central wavelength of the monochromator was set to ~500 nm and the FWHM spectral width was ~10 nm.

By processing all these raw holograms acquired at different illumination angles as discussed in the previous sections, I recovered the height distribution of the RBCs located at both of the vertical channels as illustrated in Fig. A-4(g). Fig. A-4(h) also shows the histogram of the cell heights over the entire field of view, which exhibits a double peaked behavior, as expected, resolving the 2 vertical micro-channels. Because the cells were permitted to sediment on the surface of each micro-layer, I obtained a very narrow height distribution at each channel as a result of my fine depth resolving power. For the upper micro-channel, the standard deviation of the cell height (2.4 μm) is larger than the lower channel one (1.5 μm), which is due to the surface

curvature of the spacer glass. In other words, because the spacer glass between the vertical channels is much thinner than the substrate of the bottom layer, it exhibits a significantly larger surface curvature over the imaging field of view which increased the height variations as observed in the upper channel cell height histogram (Fig. A-4(h)). Meanwhile, for the lower channel, the substrate was chosen to be >0.5 mm thick and therefore the cell height histogram showed a much better accuracy with a standard deviation of 1.5 μm in relative height of the cells.

Once the axial and lateral locations of the cells are accurately determined within this multi-layered structure (Fig. A-4(f)), I can also characterize other properties of the cells in 3D such as the thickness or the volume of each cell. Figs. A-5(a) and (c) report the thickness and the volume maps, respectively, of each one of the red blood cells that are characterized in Fig. A-4. In these figures the colormaps code the measured thickness (μm) and volume (fL) of each cell. Fig. A-5(b) and (d) also plot the thickness and volume histograms of the red blood cells at each vertical channel, which predict a mean RBC thickness of 1.74 μm and 1.68 μm for the bottom and top channels, respectively; and a mean RBC volume of 95.7 fL and 91.1 fL for the bottom and top channels, respectively. These results are in good agreement with standard values of healthy red blood cells, further validating my results.[162]

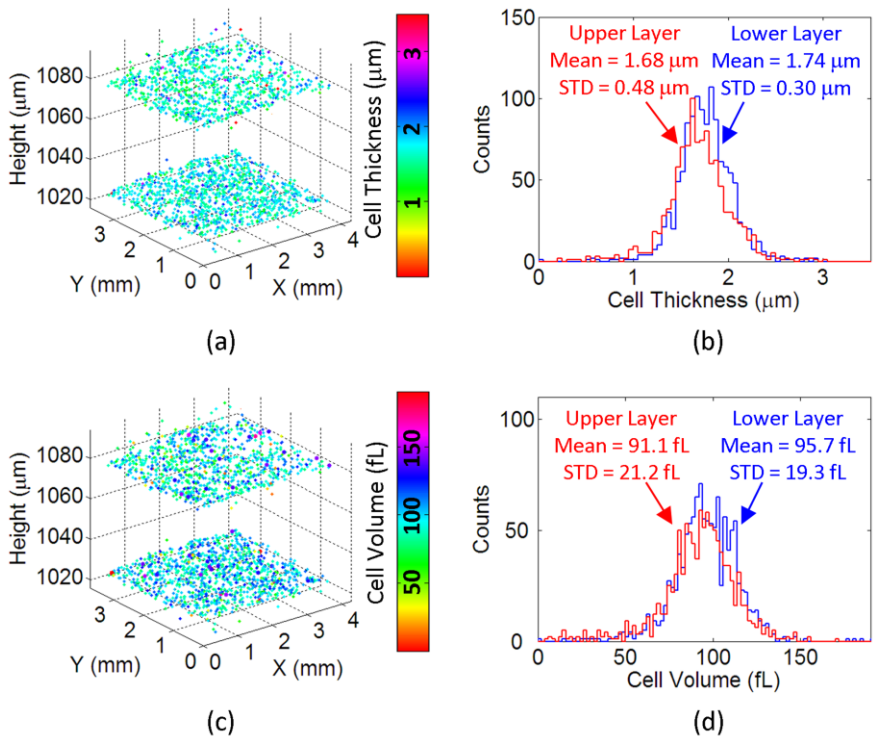

Figure A-5 | Thickness and volume of each cell within the two-layered micro-channels are calculated over a field of view of >15 mm^2. (a) The 3D distribution of the RBCs in both of the vertical channels is illustrated with their cell thickness value coded by the colormap. (b) The thickness histograms of the RBCs in both the upper and lower micro-channels are shown. (c) The 3D distribution of the RBCs in both vertical channels is illustrated with their cell volume coded by the colormap. (d) The volume histograms of the RBCs in both the upper and lower micro-channels are shown.

The key to estimate each cell's thickness and volume properties individually over the entire imaging FOV is the iterative twin image elimination algorithm that permits digital reconstruction of the phase and amplitude images of each cell from its lensfree hologram.[67,73] To relate the recovered optical phase of each cell to a physical thickness, I assumed that red blood cells are phase only objects with an average refractive index of 1.40 in a solution with refractive index 1.33.[163] Under these assumptions the thickness of the RBC is directly proportional to its phase recovered from the iterative twin-image elimination algorithm. The areas of the cells were

estimated by a simple global thresholding of the recovered phase images, and the volume of each cell was estimated by the product of its thickness and area.

For the experiments reported in Figs. A-4~A-5, the cell density at *each* layer was ~15,000 cells/μL. To achieve the reported depth accuracy in 3D for such a high concentration of cells, I made use of two key factors: (1) I used 5 illumination angles (see Fig. A-4) which reduced the likelihood of the events where all the shadows corresponding to a single cell were overlapping with other cells for *all* the illumination angles. And (2) the image reconstruction process enabled resolving densely packed cell shadows from each other. A good example of the success of this digital reconstruction process is illustrated in Fig. A-6, where 3 red blood cells from the top micro-channel overlap at the sensor plane with the holograms of 3 different red blood cells located at the bottom micro-channel (refer to the holograms within the white dashed rectangle of Fig. A-6(a) which correspond to these 6 RBCs at both layers). Fig. A-6(b) and (c) illustrate the reconstructed amplitude images at the bottom and top channel surfaces, respectively. Fig. A-6(d) also illustrates the digital reconstruction results at an intermediate plane between the bottom and the top micro-channels. To independently confirm my reconstruction results, two microscope images of the bottom and top micro-channels (corresponding to the same FOV as in Fig. A-6(a)) are also provided in Figs. A-6(e) and (f), respectively. Here I would like to also emphasize that the lensfree holographic image and its reconstructions that are reported in Figs. A-6(a)~(d) are digitally taken from a much larger field of view shown in Fig. A-4(a), which illustrates ~2 orders of magnitude increased FOV of my approach when compared to conventional optical microscope images (Figs. A-6(e)~(f)).

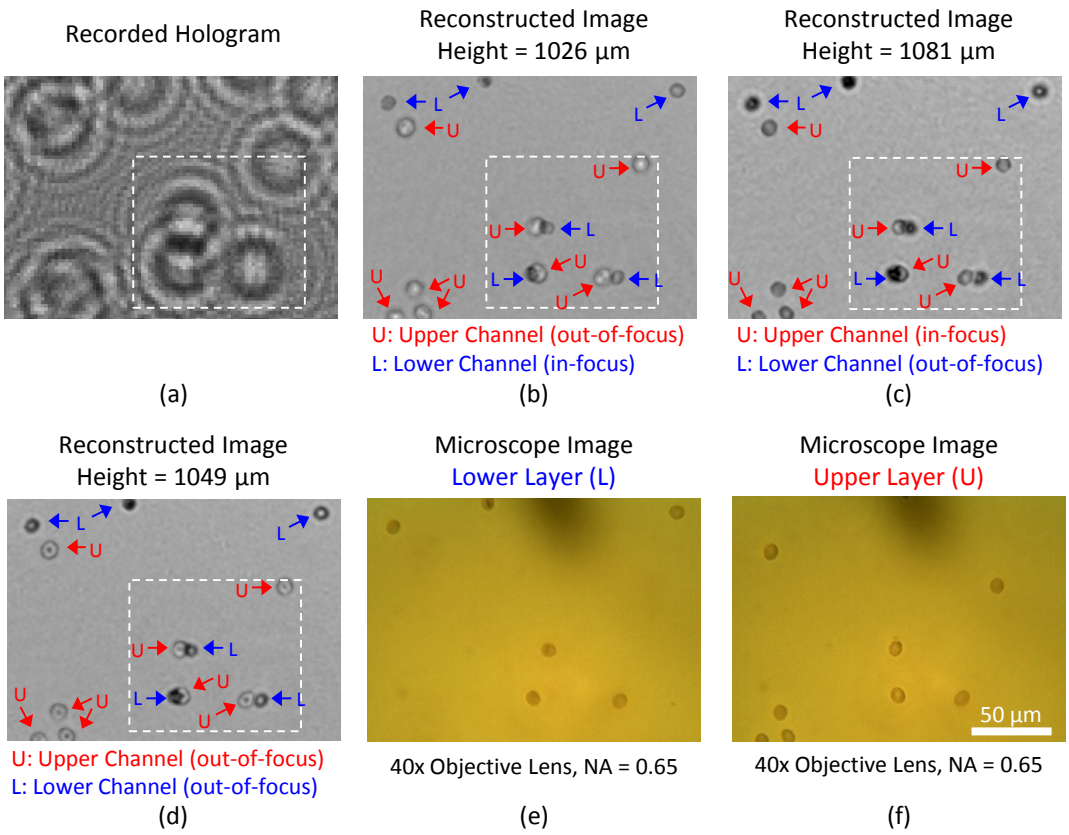

Figure A-6 | Demonstration of overlapping RBCs from two vertical micro-channels being digitally resolved by the holographic reconstruction process. (a) The raw lensfree hologram of the digitally zoomed region specified with the yellow rectangle in Fig. A-4(a) is illustrated. The amplitude images (b), (c), and (d) were reconstructed from (a) at a height of 1026 µm, 1081 µm, and 1049 µm respectively. In these reconstructed images, "L" and "U" refer to the RBCs located at the lower and upper micro-channels, respectively. The same field of view is also imaged using a 40X objective lens (0.65 NA) by focusing on both the lower (e) and the upper (f) micro-channels for comparison purposes. Note that the field of view that is imaged with Fig. A-4 constitutes ~2 orders of magnitude improvement over the 40X microscope images shown in (e-f).

A.5 Quantitative analysis of the depth localization accuracy

The accuracy of the centroid-based localization method described in this appendix has two fundamental limiting factors in a lensfree holographic configuration: the ***detection noise*** and the ***pixelation error***. Brownian motion of particles is a key factor only when the micro-objects are

suspended in the liquid, which can then be handled by reducing the integration time at the sensor chip or by using simultaneous multi-angle imaging where all the illumination angles are used at the same time. Once the micro-objects settle on the substrate surface, the friction between the objects and the surface provides enough anchoring force to significantly limit the Brownian motion.

In this section, I will derive the governing theory to quantify the effects of the detection noise and the pixelation error on the accuracy of my depth localization calculations. Next I start with the quantification of the detection noise.

The effect of the detection noise on the calculation of the centroid coordinates of the particles under the vertical illumination can be analyzed by quantifying the error propagation from the noise at individual pixels to the centroid calculations.[164,165] Following the same notation presented in Section A.4, the centroid coordinates of a particle shadow created by the vertical illumination can be re-written as:

$$\begin{cases} x_c = \dfrac{\sum_{ij} x_{ij} n_{ij}}{\sum_{ij} n_{ij}} = \dfrac{u_x}{v} \\ y_c = \dfrac{\sum_{ij} y_{ij} n_{ij}}{\sum_{ij} n_{ij}} = \dfrac{u_y}{v} \end{cases}, \tag{A-2}$$

where $u_x \equiv \sum_{ij} x_{ij} n_{ij}$, $u_y \equiv \sum_{ij} y_{ij} n_{ij}$, and $v \equiv \sum_{ij} n_{ij}$.

By using the law of error propagation, the variance of x_c and y_c (S_{xc}^2 and S_{yc}^2, respectively) can then be evaluated as:

$$\begin{cases} \dfrac{S_{xc}^2}{x_c^2} = \dfrac{S_{ux}^2}{u_x^2} + \dfrac{S_v^2}{v^2} - \dfrac{2S_{uvx}}{u_x v} \\ \dfrac{S_{yc}^2}{y_c^2} = \dfrac{S_{uy}^2}{u_y^2} + \dfrac{S_v^2}{v^2} - \dfrac{2S_{uvy}}{u_y v} \end{cases}, \tag{A-3}$$

where $S_{ux}^2 \equiv \left\langle u_x^2 \right\rangle - \left\langle u_x \right\rangle^2$ is the variance of u_x, $S_{uy}^2 \equiv \left\langle u_y^2 \right\rangle - \left\langle u_y \right\rangle^2$ is the variance of u_y, $S_v^2 \equiv \left\langle v^2 \right\rangle - \left\langle v \right\rangle^2$ is the variance of v, $S_{uvx} \equiv \langle u_x v \rangle - \langle u_x \rangle \langle v \rangle$ is the covariance of u_x and v, $S_{uvy} \equiv \left\langle u_y v \right\rangle - \left\langle u_y \right\rangle \langle v \rangle$ is the covariance of u_y and v; and $\langle\ \rangle$ denotes the expectation operator. With these definitions of u_x, u_y, and v, their variance and covariance can be expressed as:

$$\begin{cases} S_{ux}^2 = \sum_{ij} S_{ij}^2 x_{ij}^2 + \sum_{\substack{i \neq k \\ j \neq l}} S_{ijkl} x_{ij} x_{kl} \\ S_{uy}^2 = \sum_{ij} S_{ij}^2 y_{ij}^2 + \sum_{\substack{i \neq k \\ j \neq l}} S_{ijkl} y_{ij} y_{kl} \\ S_v^2 = \sum_{ij} S_{ij}^2 + \sum_{\substack{i \neq k \\ j \neq l}} S_{ijkl} \\ S_{uvx} = \sum_{ij} S_{ij}^2 x_{ij} + \sum_{\substack{i \neq k \\ j \neq l}} S_{ijkl} x_{ij} \\ S_{uvy} = \sum_{ij} S_{ij}^2 y_{ij} + \sum_{\substack{i \neq k \\ j \neq l}} S_{ijkl} y_{ij} \end{cases}, \tag{A-4}$$

where $S_{ij}^2 \equiv \left\langle n_{ij}^2 \right\rangle - \left\langle n_{ij} \right\rangle^2$ is the variance of n_{ij} and $S_{ijkl} \equiv \left\langle \left(n_{ij} - \left\langle n_{ij} \right\rangle \right) \left(n_{kl} - \left\langle n_{kl} \right\rangle \right) \right\rangle$ is the covariance of n_{ij} at two pixels. Since the noise on individual pixels can be assumed to be uncorrelated, S_{ijkl} can be dropped and the variance of the centroid coordinates, x_c and y_c, (under the vertical illumination) can be simplified as:

$$\begin{cases} S_{xc}^2 = \dfrac{u_x^2}{v^2} \left(\dfrac{S_{ux0}^2}{u_x^2} + \dfrac{S_{v0}^2}{v^2} - \dfrac{2 S_{uvx0}}{u_x v} \right) \\ S_{yc}^2 = \dfrac{u_y^2}{v^2} \left(\dfrac{S_{uy0}^2}{u_y^2} + \dfrac{S_{v0}^2}{v^2} - \dfrac{2 S_{uvy0}}{u_y v} \right) \end{cases}, \tag{A-5}$$

where $S_{ux0}^2 \equiv \sum_{ij} S_{ij}^2 x_{ij}^2$, $S_{uy0}^2 \equiv \sum_{ij} S_{ij}^2 y_{ij}^2$, $S_{v0}^2 \equiv \sum_{ij} S_{ij}^2$, $S_{uvx0} \equiv \sum_{ij} S_{ij}^2 x_{ij}$, and $S_{uvy0} \equiv \sum_{ij} S_{ij}^2 y_{ij}$.

Since the detection noise, without loss of generality, can be assumed to have a probability density function with normal distribution, the variance of $n_{ij} \equiv p_{ij}^2$ can be evaluated as:

$$
\begin{aligned}
S_{ij}^2 &= \left\langle n_{ij}^2 \right\rangle - \left\langle n_{ij} \right\rangle^2 = \left\langle p_{ij}^4 \right\rangle - \left\langle p_{ij}^2 \right\rangle^2 \\
&= \left(3S_{pij}^4 + 6\left\langle p_{ij} \right\rangle^2 S_{pij}^2 + \left\langle p_{ij} \right\rangle^4 \right) - \left(S_{pij}^2 + \left\langle p_{ij} \right\rangle^2 \right)^2 \\
&= 2S_{pij}^4 + 4\left\langle p_{ij} \right\rangle^2 S_{pij}^2,
\end{aligned}
\tag{A-6}
$$

where S_{pij}^2 is the variance of p_{ij}. As expected, Eq. (A-6) predicts that the noise level of $n_{ij} \equiv p_{ij}^2$ is not only directly linked to the noise level of p_{ij} but also modulated by the 2D profile of p_{ij}. In summary: Eqs. (A-5) and (A-6) determine the effect of the detection noise on the accuracy of the lateral centroid calculations for a measured pattern of I_{ij} under the vertical lensfree illumination.

The same analysis can also be applied to calculate the variation of the centroid coordinates for patterns imaged under oblique illumination angles, such that S_{xco}^2 and S_{yco}^2 can also be quantified in a similar fashion. Given (x_{co}, y_{co}) as the centroid coordinates of an oblique shadow, and $Shift \equiv \left[(x_{co} - x_c)^2 + (y_{co} - y_c)^2 \right]^{1/2}$ as the lateral shift along this oblique illumination angle, then the variance of the lateral shift (S_{Shift}^2) and the variance of the projected height (S_{Height}^2) can be estimated by the law of error propagation as such:

$$
\begin{aligned}
S_{Shift}^2 &= \left(\frac{\partial Shift}{\partial dx}\right)^2 S_{dx}^2 + \left(\frac{\partial Shift}{\partial dy}\right)^2 S_{dx}^2 + 2\frac{\partial Shift}{\partial dx}\frac{\partial Shift}{\partial dy} S_{dxdy} \\
&\cong \left(\frac{\partial Shift}{\partial dx}\right)^2 S_{dx}^2 + \left(\frac{\partial Shift}{\partial dy}\right)^2 S_{dy}^2 \\
&= \left(\frac{dx}{Shift}\right)^2 (S_{xc}^2 + S_{xco}^2) + \left(\frac{dy}{Shift}\right)^2 (S_{yc}^2 + S_{yco}^2)
\end{aligned}
\tag{A-7}
$$

and

$$
S_{Height}^2 = S_{Shift}^2 \cot\theta_g,
\tag{A-8}
$$

where $dx \equiv (x_{co} - x_c)$, $dy \equiv (y_{co} - y_c)$, S_{dxdy} is the covariance of dx and dy with its value close to zero, θ_g is the oblique illumination's refractive angle within the substrate, and S_{dx}^2, S_{dy}^2, S_{xc}^2, S_{yc}^2, S_{xco}^2, S_{yco}^2 are the variances of dx, dy, x_c, y_c, x_{co}, y_{co}, respectively.

After calculating the variance values of the projected height from all the oblique illumination angles with Eqs. (A-7) and (A-8), the standard deviation of the averaged particle height is estimated by:

$$S_{Height,AVG} = \frac{1}{n_a}\sqrt{\sum_{a=1}^{n_a} S_{Height,a}^2}, \tag{A-9}$$

where n_a is the number of the oblique illumination angles involved in calculating the particle height and $S_{Height,a}^2$ is the variance of the projected height for an individual oblique illumination angle. Therefore Eqs. (A-5)-(A-9) quantify the contribution of the **detection noise** to the final depth resolution of the proposed multi-angle lensfree holography platform.

Next I will investigate the impact of the second major source of error in my depth localization calculations, such that the effect of the **pixelation error** at the sensor array will now be quantified. For the vertical lensfree illumination case, the effect of pixelation error on determining the lateral centroid coordinates of the particle can be estimated by analyzing its spatial pattern sampled at the sensor array.[166] Assuming that $e(x, y)$ is the 2D continuous profile of the vertical projection pattern without noise (i.e., it represents the optical intensity profile of the particle's holographic shadow on the image sensor before being sampled); and that $f_e(x, y)$ represents the convolution of $e(x, y)$ with a square function whose width is the pixel size (Δ) of the image sensor, then the centroid coordinates x_c and y_c of the sampled pattern of the vertical illumination case can be calculated as:

$$\begin{cases} x_c = \dfrac{\iint xe(x,y)\,dxdy}{\iint e(x,y)\,dxdy} = \dfrac{\iint xf_e(x,y)\,dxdy}{\iint f_e(x,y)\,dxdy} = \dfrac{\int xf_{ex}(x)\,dx}{\int f_{ex}(x)\,dx} \\ y_c = \dfrac{\iint ye(x,y)\,dxdy}{\iint e(x,y)\,dxdy} = \dfrac{\iint yf_e(x,y)\,dxdy}{\iint f_e(x,y)\,dxdy} = \dfrac{\int yf_{ey}(y)\,dy}{\int f_{ey}(y)\,dy} \end{cases}, \tag{A-10}$$

where $f_{ex}(x) \equiv \int f_e(x,y)\,dy$ and $f_{ey}(y) \equiv \int f_e(x,y)\,dx$. Assuming that η_x and η_y define the offset of the centroid position from the center of a pixel along the x and y directions, respectively, then the centroid coordinate estimation errors $\delta_x(\eta_x)$ and $\delta_y(\eta_y)$ can be expressed as[166]

$$\begin{cases} \delta_x = \dfrac{\sum_{n=1}^{\infty} F_{ex}'(n/\Delta)\sin(2\pi\eta_x n/\Delta)}{\pi\left[F_{ex}(0) + \sum_{n=1}^{\infty} F_{ex}(n/\Delta)\cos(2\pi\eta_x n/\Delta)\right]} \\ \delta_y = \dfrac{\sum_{n=1}^{\infty} F_{ey}'(n/\Delta)\sin(2\pi\eta_y n/\Delta)}{\pi\left[F_{ey}(0) + \sum_{n=1}^{\infty} F_{ey}(n/\Delta)\cos(2\pi\eta_y n/\Delta)\right]} \end{cases}, \tag{A-11}$$

where $F_{ex}(u)$ and $F_{ey}(v)$ represent the Fourier transforms of $f_{ex}(x)$ and $f_{ey}(y)$, respectively; $F_{ex}'(u)$ and $F_{ey}'(v)$ are the first derivatives of $F_{ex}(u)$ and $F_{ey}(v)$, respectively. Without loss of generality, one can confidently assume that η_x and η_y are both uniformly distributed between -Δ/2 and Δ/2. Accordingly, the standard deviation of the 2D localization errors arising from **pixelation noise** can be calculated as such:

$$\begin{cases} S_{xc,px} = \sqrt{\dfrac{1}{\Delta}\int \delta_x{}^2(\eta_x)\,d\eta_x} \\ S_{yc,px} = \sqrt{\dfrac{1}{\Delta}\int \delta_y{}^2(\eta_y)\,d\eta_y} \end{cases}. \tag{A-12}$$

Eq. (A-12) quantifies the impact of pixelation error on the accuracy of the lateral centroid coordinate calculations for a pattern measured under the vertical lensfree illumination. The same procedures that were discussed above for the detection noise analysis can also be used to calculate the variances of the centroid coordinates for all the oblique illumination angles due to

pixelation error. After calculating the variances of all illumination angles, the height deviation contributed by pixelation error can then be evaluated the same way as the height deviation due to the detection noise was calculated above (refer to Eqs. (A-7)~(A-9)).

To better quantify the nature of the detection noise in my set-up, I experimentally characterized the noise statistics of one of my sensors (Kodak, CCD KAF-8300) under the same illumination conditions that are reported in the Experimental Results Section (Fig. A-3). In these characterization experiments, my goal was to estimate the relative strengths of different noise terms in my experimental set-up to permit an accurate comparison of my results against the theoretical limits. Toward this end, Fig. A-7(a) reports the variance values of the pixels of the sensor chip measured with different integration times as a function of the illumination intensity. To quantify the individual contributions of different noise processes, I used a noise model given by

$$S_I^2 = a_2 I^2 + a_1 I + a_t t + a_0,$$

where I is the mean value of the measured pixels; S_I^2 is the variance of the pixel values; t is the integration time; a_2, a_1, a_t, and a_0 are the parameters for Relative Intensity Noise (**RIN**), Shot Noise (**SN**), Dark Leakage Noise (**DLN**), and Readout Noise (**RN**), respectively. Multi-variable fitting results showed that the detection noise at the sensor chip was mostly dominated by RIN and SN (see the Fig. A-7(b) for the decomposition of the noise terms as a function of the pixel intensity). These results enabled me to assess the relative magnitudes of different detection noise terms and their total contribution to the localization error in my lensfree measurements.

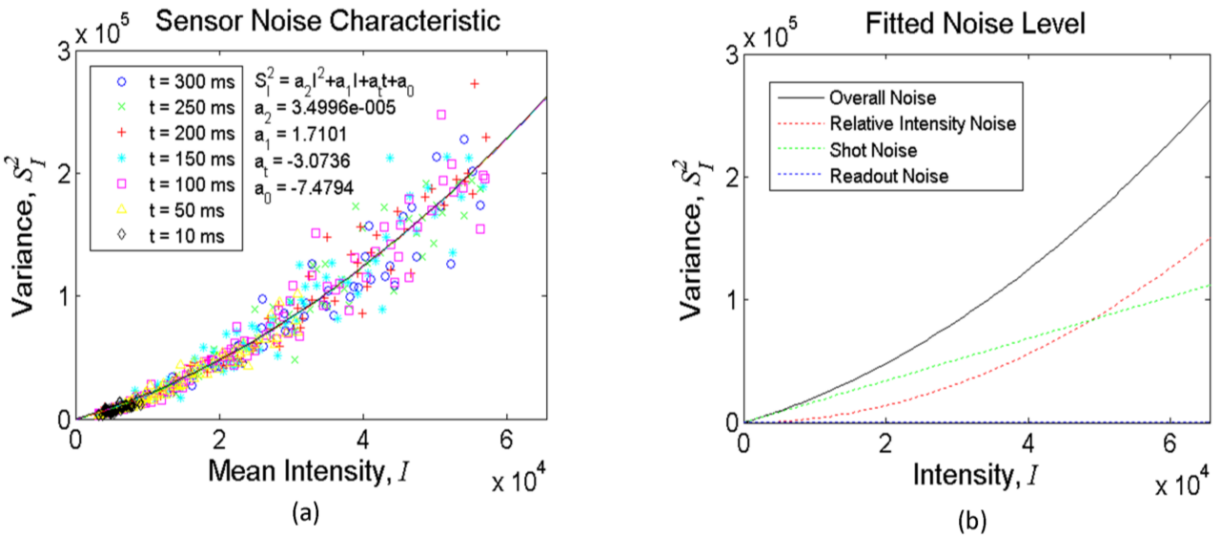

Figure A-7 | Noise characteristics of a typical CCD image sensor, Kodak KAF-8300, are quantified. (a) reports the variance values of the pixels of the sensor chip measured with different integration times as a function of the illumination intensity. (b) quantifies the decomposition of various noise terms as a function of the illumination intensity. The fitted strengths of individual noise terms in (b) were calculated based on the parameter values estimated in (a). The results indicate that dominant detection noise sources were relative intensity noise and shot noise for this image sensor.

After these characterization steps, using Eqs. (A-7)~(A-12), I estimated the individual contributions of both the detection noise and the pixelation error on the accuracy of my centroid calculations for the depth localization experiments reported in Fig. A-3 (see Tables A-1~A-2 for the summarized results). In my experiments, since a total distance of 500-1000 μm has been used between the micro-objects and the sensor plane, the detected holograms are spread out over at least 6-8 pixels, which greatly suppressed the pixelation error. Therefore, the relative weight of the pixelation error on centroid calculation accuracy is much smaller than the detection noise contribution as also quantified in Tables A-1 and A-2. The overall lateral localization errors reported in Table A-1 (*Sxc,all* and *Syc,all*) are purely based on the vertical lensfree illumination

measurements, while the height localization errors reported in Table A-2 are calculated from all the oblique illumination angles together with the vertical one (see Fig. 3(a~c)).

Beads Diameter (um)	Estimated Lateral Localization Error (μm)					
	Det. Noise		Pixelation		Overall	
	Sxc	*Syc*	*Sxc,px*	*Syc,px*	*Sxc,all*	*Syc,all*
5	0.30	0.31	0.13	0.11	0.32	0.33
10	0.09	0.10	0.04	0.02	0.10	0.10
20	0.04	0.04	0.00	0.00	0.04	0.04

Table A-1 | The theoretical breakdown of the lateral localization error. Standard deviation values were evaluated for each micro-particle type using the lensfree holograms of Figs. A-3(a)~(c).

Beads Diameter (um)	Height Deviation (μm)					
	Detection Noise (SN+RIN)	Pixelation Error	Beads Size STD	Theoretical STD	Measured STD	Systematic STD
5	0.66	0.05	0.03	0.67	0.97	0.71
10	0.20	0.01	0.05	0.21	0.37	0.31
20	0.08	0.00	0.14	0.16	0.32	0.28

Table A-2 | The theoretical breakdown of the height localization errors and comparison to the measurement results. Standard deviation values of both the theoretical and experimental results are evaluated with the lensfree holograms of Figs. A-3(a~c). The theoretical standard deviation (STD) in height of each micro-particle type is evaluated by summing the height deviation contributed by detection noise, pixelation error, and bead size deviation.

Table A-2 also indicates that the level of my experimental characterization accuracy is quite close to the theoretical limit that is calculated based on the measured noise characteristics of the set-up. This fairly close comparison between my characterization results and the theoretical values supports the validity of my error analysis as well as the depth localization algorithm. Furthermore, the statement that the decreased depth localization accuracy with smaller micro-

objects (as observed in Fig. A-3) is due to the decrease of the detection signal-to-noise ratio is also validated with this comparison reported in Table A-1.

A.6 Theoretical analysis of multi-angle characterization error rate

Besides the accuracy of cell/particle localization, another important parameter that needs more discussion for the presented multi-angle lensfree imaging platform is its *characterization error rate* (i.e., the overall percentage of false positives and missed cells within the sample volume), which surely is dependent on the density of the objects to be imaged. To better investigate and quantify this dependence, I have performed numerical simulations, the results of which are summarized in Figs. A-8~A-12. In these simulations, I report the density of cells in terms of the density of shadows that they create at the sensor plane under the vertical illumination. Therefore, this density of shadows at the sensor plane is equivalent to the number of independent micro-objects to be imaged per frame, which is a direct measure of the throughput of imaging.

Overlapping shadows at the sensor plane, which can cause both missed (i.e., un-identified) objects as well as false characterized (i.e., false positive) objects, is the major source of the characterization error for this multi-angle imaging platform. Therefore, I would start the quantitative analysis of system characterization error by investigating the overlapping of cell shadows in the single-layer case. The shadow overlapping ratio of a homogeneous cell suspension in such case can be modeled by randomly distributing a large number of identical small circular patterns over the field of view:[167]

The probability of overlapping between any two shadows can be calculated by the probability that the distance between the centers of two shadows in the field of view is smaller than their diameters:

$$P(r < D) = \frac{\pi D^2}{A}$$

where r is the distance between the centers, D is the diameter of the shadows, A is the area of the field of view, and the boundary effect is neglected. For each shadow, the probability of being not overlapping with any of the other N-1 shadows in the field of view will be

$$P_{nov} = \left(1 - \frac{\pi D^2}{A}\right)^{N-1}.$$

With $\frac{\pi D^2}{A} << 1$, $N >> 1$, and $\exp(x) \equiv \lim_{n\to\infty}\left(1 + \frac{x}{n}\right)^n$,

$$\begin{aligned} P_{nov} &= \left(1 - \frac{\pi D^2}{A}\right)^{N}\left(1 - \frac{\pi D^2}{A}\right)^{-1} \approx \left(1 - \frac{\pi D^2}{A}\right)^{N} = \left(1 - \frac{\pi D^2 N}{AN}\right)^{N} \approx \exp\left(-\frac{\pi D^2 N}{A}\right), \\ &= \exp\left(-\pi D^2 \rho\right) \end{aligned} \tag{A-13}$$

where $\rho \equiv N/A$ is the shadow density defined as the number of shadow in unit area.

Assuming that all the non-overlapped shadows will be detected correctly by the pattern matching algorithm, P_{nov} can be considered as the true positive rate for the single-layer case. Since there is no significant source of phantom cells in this detection mechanism, the false positive rate is assumed to be zero. Therefore the total error rate Err for the single-layer case will be simply the sum of false negative rate R_{FN} and false positive rate R_{FP}, i.e.,

$$\begin{aligned} Err &= R_{FN} + R_{FP} = 1 - P_{nov} + 0 \\ &= 1 - \exp\left(-\pi D^2 \rho\right) \end{aligned} \tag{A-14}$$

where false negative rate R_{FN} is the probability of a cell failing to be detected correctly and essentially is the complement of true positive rate R_{TP} (i.e. $R_{FN} = 1 - R_{TP}$); false positive rate R_{FP} is the ratio between the number of phantom cells being incorrectly detected and the number of existing cells that are vertically projected into unit area.

Equation (A-14) provides a convenient method to simulate the relation between characterization error rate and cell density in the single-layer case and how it is affected by the number of illumination angles. According to my simulation results, as the density of shadows at

the sensor chip increases, the overlap probability among cell shadows also increases as illustrated in Fig. A-8. Since illuminating with multiple light sources simultaneously is in effect multiplying the density of cell shadows by the number of illumination angles, as one would expect, sequential imaging with different illumination angles copes much better with increasing shadow density when compared to parallel (i.e., simultaneous) imaging with all the angles (see Fig. A-8). The cost of this improvement that comes with sequential lensfree imaging is a reduction in the speed of data capture since more frames need to be captured to characterize the same volume of interest.

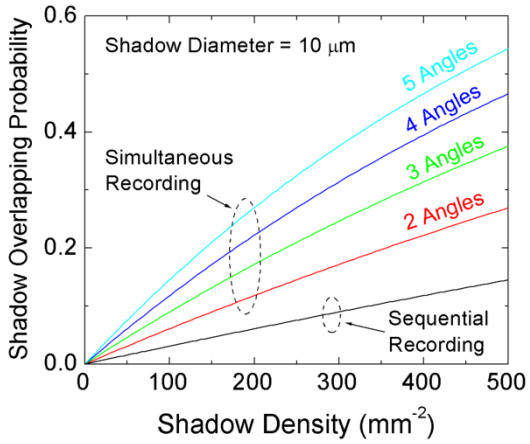

Figure A-8 | The shadow overlap probability plotted as a function of both the shadow density (i.e., the throughput) and the multi-angle hologram recording method (parallel vs. sequential). The diameter of the holographic shadows for all the angles and all the vertical layers is assumed to be 10 μm.

Next, I are going to use Eq. (A-13) to analyze the characterization error rate in the multi-layer case, in which the cells are dispensed to several layers, sequentially illuminated by multiple angles, are then located through the process described in section A.2.

Several assumptions are made to simply the analysis of the multi-layer case: *(1)* The shadows of a cell in all illumination angles are all assumed to circles with identical diameters. Since the

holographic reconstruction can provide the cell's projection profile on the plane normal to the illumination beam, the shape of the cell shadow will not be changed much by the projection distortion. *(2)* The same type of cells on different layers will have similar shadow sizes. This is validated by the presumption that the layers are physically close to each other, e.g. three layers are packed in a 200-μm-thick microfluidic device. Both the sizes of the hologram or the reconstruction patterns will not change significantly for this scale of distance. *(3)* The cross-sections of the backward projected beams on each layer have the same shapes and dimensions as their corresponding cells. *(4)* All the cells under investigation have similar shapes and sizes. *(5)* The cells are evenly distributed across all layers. Hence, if the total shadow density across n_L layers is ρ, the cell density in each layer by will be ρ/n_L, with the unit of cells per unit area.

The true positive rate for the multi-layer case is lowered by two situations: The clustering of the cells in the same layer makes the cell shadows overlapped in all angles; the shadow of an isolated cell is overlapped with the shadow of another cell on a different layer in a certain illumination angle. Using Eq. (A-13), the probability for a cell being isolated from any other cells in the same layer can be expressed as

$$P_{iso} = \exp\left(-\pi D^2 \frac{\rho}{n_L}\right). \tag{A-15}$$

Then, the probability of the shadow of an isolated cell in one layer not overlapping with the shadow of any cells on the other $n_L - 1$ layers in one illumination angle is equivalent to the probability of a shadow not overlapping with the other $\frac{n_L - 1}{n_L} N$ imaginary shadows in the same layer, i.e.

$$P_{novl} = \exp\left(-\pi D^2 \frac{n_L - 1}{n_L}\rho\right). \tag{A-16}$$

Accordingly, the probability that the shadow of an isolated cell not overlapping with any other cell shadows in n_i angles but overlapped in the other n_A-n_i angles is

$$P_{novli} = C_{n_a}^{n_i} P_{novl}^{n_i}\left(1 - P_{novl}\right)^{n_A - n_i}, \tag{A-17}$$

where C_n^k is the number of ways of picking k unordered outcomes from n possibilities and n_A is the number of the illumination angles used for matching shadows.

Based on the cell locating process described in section A.2, there are two requirements for a cell to be correctly detected by the shadow matching algorithm: *(1)* The cell can't overlap with any other cell on the same layer. *(2)* The number of the beams projected from the detected shadows and intercepting on the cell's location must be larger than the threshold value n_T. In other words, the cell shadow needs to be isolated from the shadows of other cells in at least n_T angles, i.e. $n_A \geq n_i \geq n_T$.

As a result, the true positive rate for the multi-layer case can be evaluated by combining Eq. (A-15)~(A-17) as

$$R_{TP} = P_{iso} \sum_{n_i = n_T}^{n_A} P_{novli} = P_{iso} \sum_{n_i = n_T}^{n_A} C_{n_A}^{n_i} P_{novl}^{n_i}\left(1 - P_{novl}\right)^{n_A - n_i}. \tag{A-18}$$

If only the vertical illumination is used to characterize multiple layers of cells, both n_A and n_T will equal to one and the true positive rate will degenerate to the single-layer case, i.e.,

$$\begin{aligned} R_{TP} &= P_{iso} C_1^1 P_{novl}^1\left(1 - P_{novl}\right)^{1-1} = P_{iso} P_{novl} = \exp\left(-\pi D^2 \frac{1}{n_L}\rho\right)\exp\left(-\pi D^2 \frac{n_L - 1}{n_L}\rho\right). \\ &= \exp\left(-\pi D^2 \rho\right) = P_{nov} \end{aligned}$$

The second part of the error rate *Err* is contributed by false positives, which results from the coincidental interception of backward projected beams on spots without actual cells and

increases quickly with higher cell densities. First I evaluate the probability of a point on a certain layer not being occupied by the N/n_L cells in that layer as

$$P_{uno} = \left(1 - \frac{\pi r^2}{A}\right)^{\frac{N}{n_L}},$$

where r is the radius of the cell.

With $\frac{\pi r^2}{A} << 1$, $N >> 1$, and $\exp(x) \equiv \lim_{n\to\infty}\left(1 + \frac{x}{n}\right)^n$, one can derive

$$P_{uno} = \left(1 - \frac{\pi r^2 \frac{N}{n_L}}{A\frac{N}{n_L}}\right)^{\frac{N}{n_L}} \approx \exp\left(-\frac{\pi r^2}{A}\frac{N}{n_L}\right) = \exp\left(-\pi r^2 \frac{\rho}{n_L}\right).$$

The probability that an unoccupied point lies within the backward projected beams of any cells on the other $n_L - 1$ layers in one illumination angle can be calculated as the probability of a point being inside any of the other $\frac{n_L - 1}{n_L} N$ imaginary cells in that layer, i.e.,

$$P_{inl} = 1 - \exp\left(-\pi r^2 \frac{n_L - 1}{n_L}\rho\right).$$

Accordingly, the probability that an unoccupied point lies within the backward projected beams of some cell shadows in n_i angles but outside any beams in the other n_A-n_i angles is

$$P_{inli} = C_{n_a}^{n_i} P_{inl}^{n_i} \left(1 - P_{inl}\right)^{n_A - n_i}.$$

The false positive occurs when a point is not occupied by any cell and lies within some backward projected beams in at least n_T angles. Therefore the probability of a point turning into a false positive can be evaluated by

$$P_{FP} = P_{uno} \sum_{n_i = n_T}^{n_A} P_{inli} = P_{uno} \sum_{n_i = n_T}^{n_A} C_{n_A}^{n_i} P_{inl}^{n_i} \left(1 - P_{inl}\right)^{n_A - n_i}.$$

If there is only one single layer of cells, false positive will never occur regardless of the number of illumination angles and the threshold value:

$$P_{FP} = \exp\left(-\pi r^2 \frac{\rho}{1}\right) \sum_{n_i=n_T}^{n_A} C_{n_A}^{n_i} \left(1-\exp\left(-\pi r^2 \frac{1-1}{1}\rho\right)\right)^{n_i} \left(\exp\left(-\pi r^2 \frac{1-1}{1}\rho\right)\right)^{n_A-n_i}$$
$$= \exp\left(-\pi r^2 \rho\right) \sum_{n_i=n_T}^{n_A} C_{n_A}^{n_i} (1-1)^{n_i} (1)^{n_A-n_i} = 0$$

To quantify the false positive in a measurable way, the average shadow spacing is used as the sampling period on all layers for determining the false positive density,

$$D_{FP} \equiv P_{FP} \frac{1}{\pi r^2} n_L ,$$

which is defined by the number of false positives vertically projected on an unit area of the imaging plane. In this way, the false positive rate can be calculated by dividing the false positive density by the shadow density,

$$R_{FP} \equiv \frac{D_{FP}}{\rho} = \frac{n_L}{\rho \pi r^2} P_{uno} \sum_{n_i=n_T}^{n_A} C_{n_A}^{n_i} P_{inl}^{n_i} (1-P_{inl})^{n_A-n_i} . \quad \text{(A-19)}$$

Now, let's check the validity of this false positive model with a special case in which the area density of the shadows is low, i.e., $\rho\pi r^2 << 1$, and the threshold value is set to one:

$$P_{uno} = \exp\left(-\pi r^2 \frac{\rho}{n_L}\right) \approx 1 - \pi r^2 \frac{\rho}{n_L} \approx 1$$

$$P_{inl} = 1 - \exp\left(-\pi r^2 \frac{n_L - 1}{n_L}\rho\right) \approx \pi r^2 \frac{n_L - 1}{n_L}\rho$$

where the approximation of $\exp(x) \approx 1 + x$ is used. Then the false positive rate will become

$$
\begin{aligned}
R_{FP} &= \frac{n_L}{\rho\pi r^2}\sum_{n_i=1}^{n_A} C_{n_A}^{n_i}\left(\pi r^2\frac{n_L-1}{n_L}\rho\right)^{n_i}\left(1-\pi r^2\frac{n_L-1}{n_L}\rho\right)^{n_A-n_i} \\
&\approx \frac{n_L}{\rho\pi r^2}\sum_{n_i=1}^{n_A} C_{n_A}^{n_i}\left(\pi r^2\frac{n_L-1}{n_L}\rho\right)^{n_i}\cdot 1 \\
&= \frac{n_L}{\rho\pi r^2}\left[C_{n_A}^{1}\left(\pi r^2\frac{n_L-1}{n_L}\rho\right)+C_{n_A}^{2}\left(\pi r^2\frac{n_L-1}{n_L}\rho\right)^2+\ldots+C_{n_A}^{n_A}\left(\pi r^2\frac{n_L-1}{n_L}\rho\right)^{n_A}\right] \\
&\approx \frac{n_L}{\rho\pi r^2}\left[n_A\left(\pi r^2\frac{n_L-1}{n_L}\rho\right)\right] = n_A(n_L-1)
\end{aligned}
,
$$

which means that a cell in any layer can generate one false positive on each of the other $n_L - 1$ layers with each of the n_A illumination angles. Since the result meets the expectation, this particular case logically validates the false positive model of equation (A-19).

By combining equation (8) and (17), one can calculate the total error rate in the multi-layer case as

$$Err = R_{FN} + R_{FP} = 1 - R_{TP} + R_{FP}. \tag{A-20}$$

Using Eq. (A-20), I quantified the performance of my algorithm in Fig. A-9 for such characterization errors as a function of the shadow density at the sensor chip, according to the procedures described in section A.2. Fig. A-9(c) concludes that for the same total number of cells to be imaged per FOV (such that for achieving the same characterization throughput) utilizing 3 or 4 vertical micro-channels performs roughly the same in terms of their characterization error rate, whereas 2 vertical micro-channels (although performing much better than a single channel having all the cells) perform worse than either 3 or 4 vertical channels. The same conclusion is also summarized in Fig. A-9(d) in a different format: for a total error rate of 5%, a 3- or 4-layered microfluidic device with this multi-angle imaging platform will have ~2.3 times higher throughput than a single-layered device.

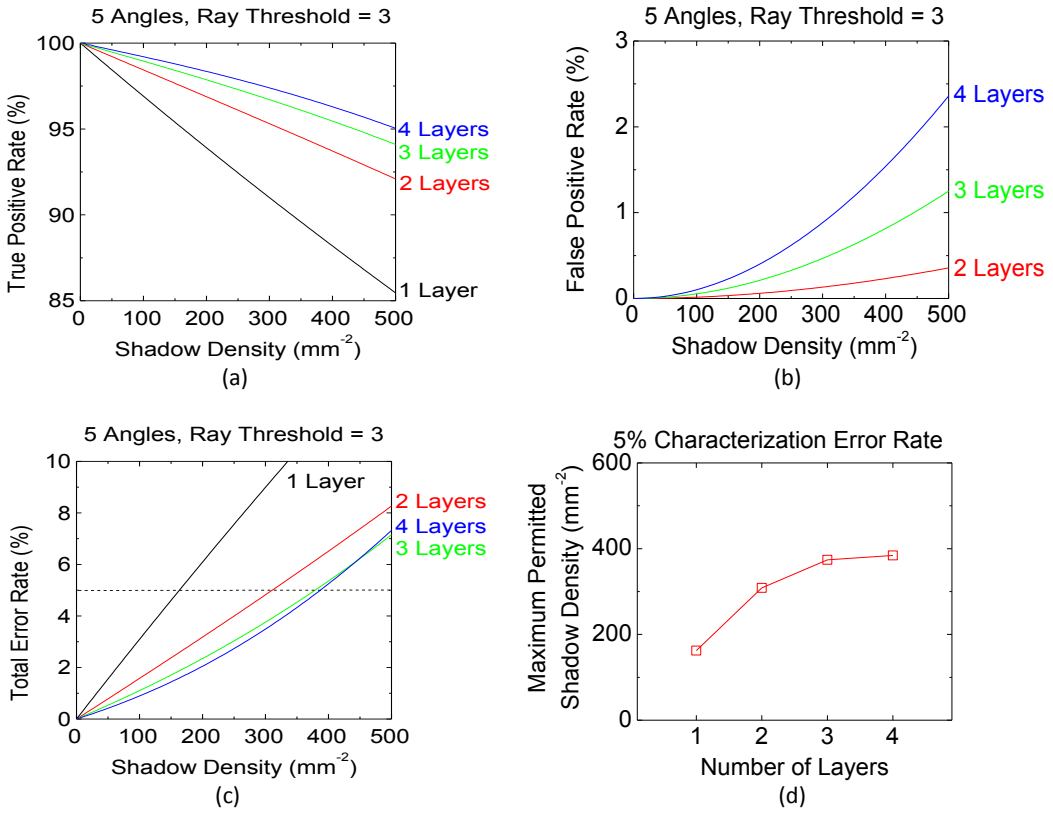

Figure A-9 | Quantified performance comparison of the multi-angle lensfree holographic cell characterization platform as a function of the shadow density and the number of vertical layers on the sensor chip. (a) The true positive rate, (b) the false positive rate, and (c) the total error rate for different cell densities distributed to 1, 2, 3, or 4 vertical layers/channels, where the total error rate includes both the missed cells and the false positives. (d) The maximum permitted shadow density (i.e., the maximum permitted throughput) at the sensor plane is plotted as a function of the number of vertical layers when the total error rate is maintained at a level of 5%. The cells are assumed to be illuminated from 5 different angles as shown in Fig. A-1(a), and the ray threshold value is set to 3 for detecting each cell's 3-D location (based on the simulation results in Figs. A-10~A-12). The shadow width at the sensor plane is assumed to be 10 μm for these numerical simulations.

More detailed investigation of the behavior of 2, 3 and 4 vertical channels for handling increasing shadow densities (i.e., increasing throughput) as a function of the number of illumination angles and ray threshold factor is provided in Figs. A-10, A-11, and A-12,

respectively. These detailed figures also support the conclusions of Fig. A-9, and further shed light on the choice of the optimum conditions for a given number of illumination angles to achieve a desired imaging throughput at an acceptable characterization error rate.

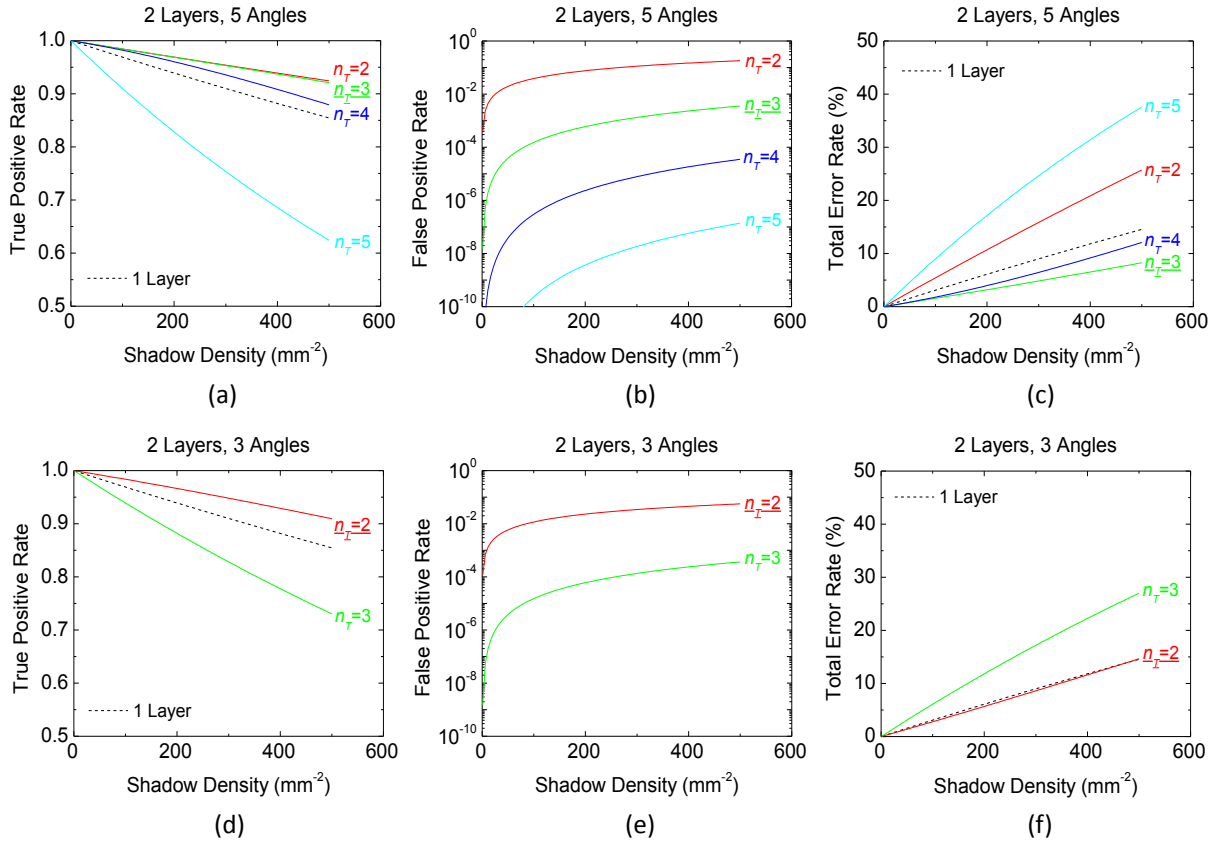

Figure A-10 | Error rate characterization of the reported multi-angle algorithm for analyzing 2 vertical layers of cells with different illumination conditions and ray threshold values. (a) The true positive rate, (b) the false positive rate, and (c) the total error rate as a function of the shadow density at the sensor plane are reported for 5 illumination angles. In each image, the effect of the ray threshold value (denoted by n_T) on my characterization accuracy is also quantified. (d), (e) and (f) report the same error characterization as a function of the imaging throughput for this time 3 illumination angles, rather than 5. The holographic shadow width of the cells at the sensor plane is assumed to be 10 μm for these calculations.

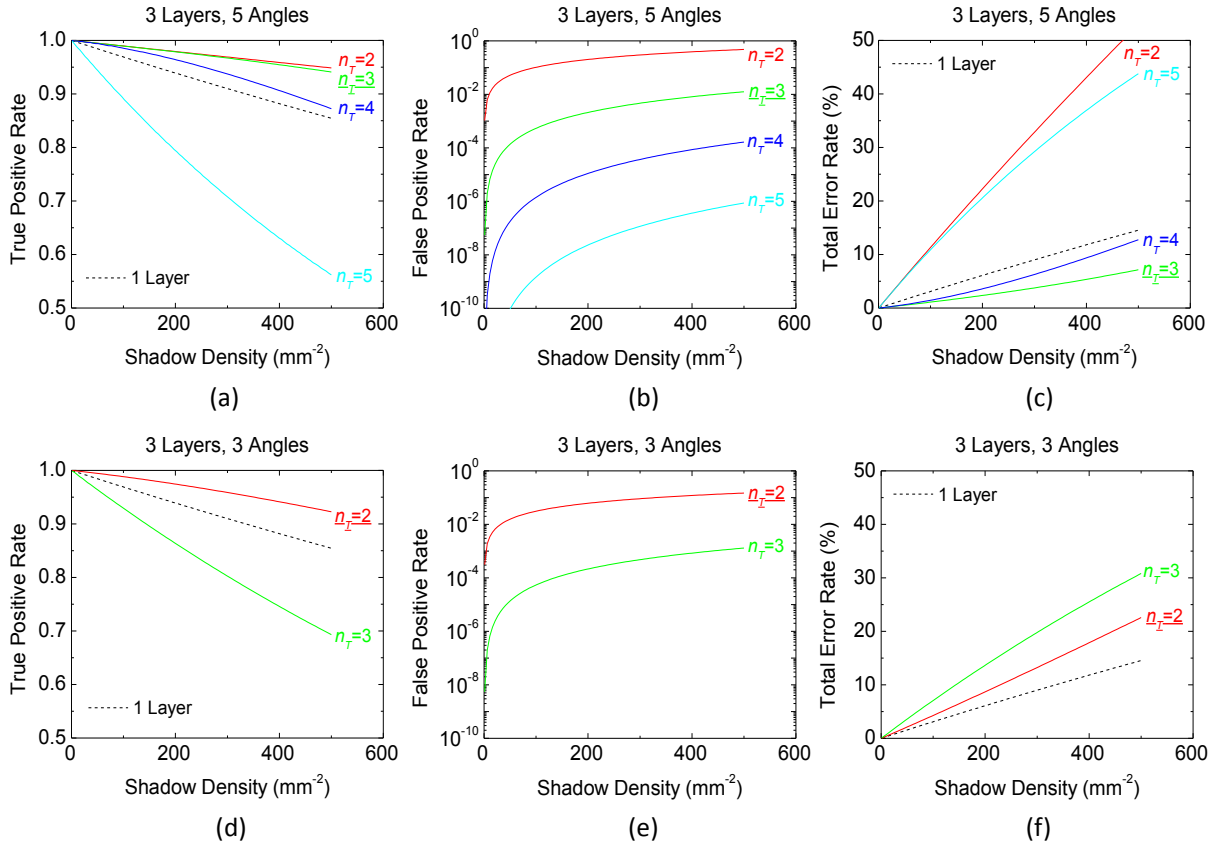

Figure A-11 | Same as Fig. A-10, except that the error characterization results as a function of the imaging throughput are now reported for 3 vertical layers of cells with different illumination conditions and ray threshold values (n_T).

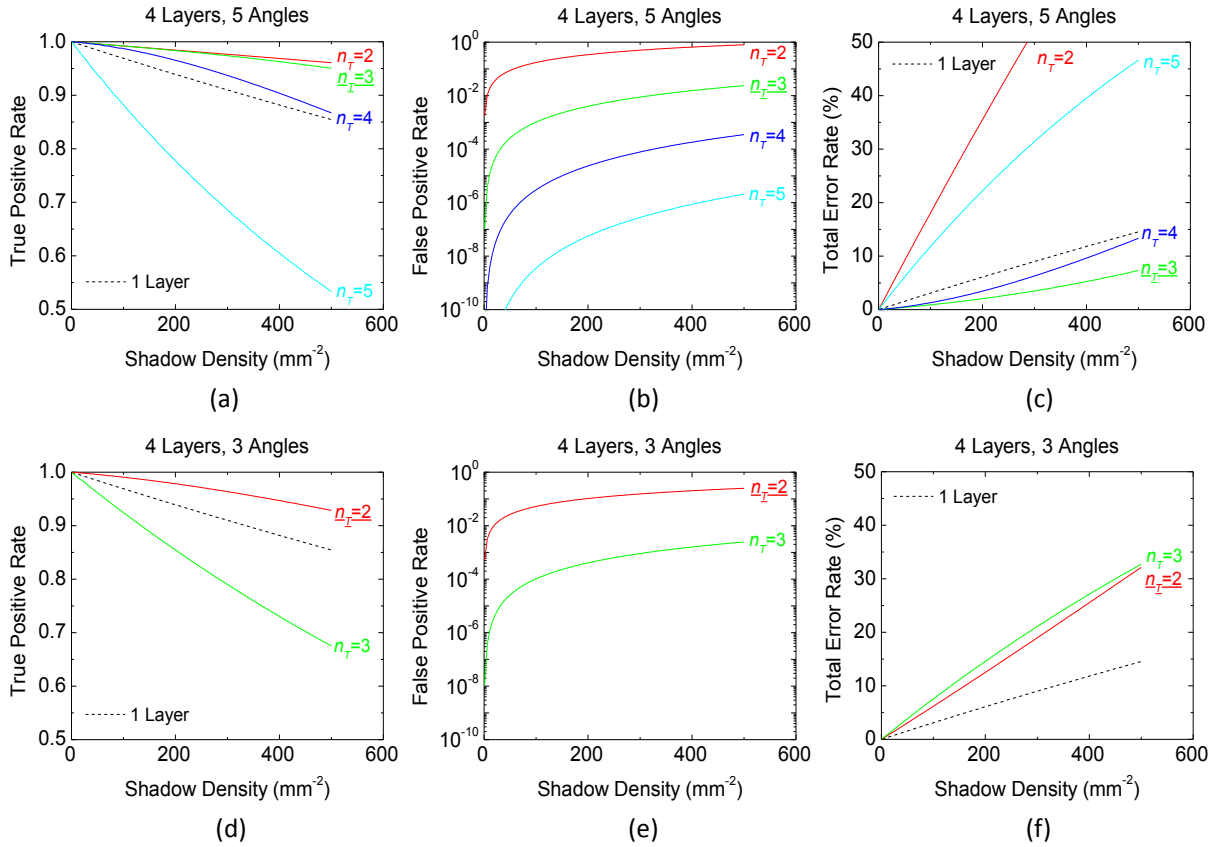

Figure A-12 | Same as Fig. A-10, except that the error characterization results as a function of the imaging throughput are now reported for 4 vertical layers of cells with different illumination conditions and ray threshold values (n_T).

The above discussion clearly shows this multi-angle holographic imaging platform can achieve a much higher throughput with multi-layered micro-fluidic devices. The compactness and increased throughput of this platform will greatly benefit point-of-care cytometry and diagnostics applications. Within a simple micro-fluidic device, the body fluid from multiple patients can be simultaneously imaged and characterized in isolated layers without the risk of cross-contamination.

References

1. Hell, S. W. Toward fluorescence nanoscopy. *Nat Biotech* **21**, 1347–1355 (2003).

2. Gustafsson, M. G. L. Nonlinear structured-illumination microscopy: Wide-field fluorescence imaging with theoretically unlimited resolution. *Proceedings of the National Academy of Sciences of the United States of America* **102**, 13081–13086 (2005).

3. Betzig, E. *et al.* Imaging Intracellular Fluorescent Proteins at Nanometer Resolution. *Science* **313**, 1642–1645 (2006).

4. Rust, M. J., Bates, M. & Zhuang, X. Sub-diffraction-limit imaging by stochastic optical reconstruction microscopy (STORM). *Nat Meth* **3**, 793–796 (2006).

5. Hess, S. T., Girirajan, T. P. K. & Mason, M. D. Ultra-High Resolution Imaging by Fluorescence Photoactivation Localization Microscopy. *Biophysical Journal* **91**, 4258–4272 (2006).

6. Ma, Z., Gerton, J. M., Wade, L. A. & Quake, S. R. Fluorescence near-field microscopy of DNA at sub-10 nm resolution. *Phys. Rev. Lett* **97**, 260801 (2006).

7. Chung, E., Kim, D., Cui, Y., Kim, Y.-H. & So, P. T. C. Two-Dimensional Standing Wave Total Internal Reflection Fluorescence Microscopy: Superresolution Imaging of Single Molecular and Biological Specimens. *Biophysical Journal* **93**, 1747–1757 (2007).

8. Pavani, S. R. P. *et al.* Three-dimensional, single-molecule fluorescence imaging beyond the diffraction limit by using a double-helix point spread function. *Proceedings of the National Academy of Sciences* **106**, 2995–2999 (2009).

9. Zipfel, W. R., Williams, R. M. & Webb, W. W. Nonlinear magic: multiphoton microscopy in the biosciences. *Nat Biotech* **21**, 1369–1377 (2003).

10. Evans, C. L. *et al.* Chemically-selective imaging of brain structures with CARS microscopy. *Opt. Express* **15**, 12076–12087 (2007).

11. Choi, W. *et al.* Tomographic phase microscopy. *Nat Meth* **4**, 717–719 (2007).

12. Barretto, R. P. J., Messerschmidt, B. & Schnitzer, M. J. In vivo fluorescence imaging with high-resolution microlenses. *Nat Meth* **6**, 511–512 (2009).

13. Rosen, J. & Brooker, G. Non-scanning motionless fluorescence three-dimensional holographic microscopy. *Nat Photon* **2**, 190–195 (2008).

14. Goda, K., Tsia, K. K. & Jalali, B. Serial time-encoded amplified imaging for real-time observation of fast dynamic phenomena. *Nature* **458**, 1145–1149 (2009).

15. Squires, T. M. & Quake, S. R. Microfluidics: Fluid physics at the nanoliter scale. *Reviews of Modern Physics* **77**, 977–1026 (2005).

16. Whitesides, G. M. The origins and the future of microfluidics. *Nature* **442**, 368–373 (2006).

17. Psaltis, D., Quake, S. R. & Yang, C. Developing optofluidic technology through the fusion of microfluidics and optics. *Nature* **442**, 381–386 (2006).

18. Haddad, W. S. *et al.* Fourier-transform holographic microscope. *Appl. Opt.* **31**, 4973–4978 (1992).

19. Xu, W., Jericho, M. H., Meinertzhagen, I. A. & Kreuzer, H. J. Digital in-line holography for biological applications. *Proceedings of the National Academy of Sciences of the United States of America* **98**, 11301–11305 (2001).

20. Pedrini, G. & Tiziani, H. J. Short-Coherence Digital Microscopy by Use of a Lensless Holographic Imaging System. *Appl. Opt.* **41**, 4489–4496 (2002).

21. Repetto, L., Piano, E. & Pontiggia, C. Lensless digital holographic microscope with light-emitting diode illumination. *Opt. Lett.* **29**, 1132–1134 (2004).

22. Garcia-Sucerquia, J., Xu, W., Jericho, M. H. & Kreuzer, H. J. Immersion digital in-line holographic microscopy. *Opt. Lett.* **31**, 1211–1213 (2006).

23. Cui, X. *et al.* Lensless high-resolution on-chip optofluidic microscopes for Caenorhabditis elegans and cell imaging. *Proc. Natl. Acad. Sci. USA* **105**, 10670–10675 (2008).

24. Ozcan, A. & Demirci, U. Ultra wide-field lens-free monitoring of cells on-chip. *Lab Chip* **8**, 98–106 (2008).

25. Seo, S., Su, T.-W., Erlinger, A. & Ozcan, A. Multi-color LUCAS: Lensfree On-chip Cytometry Using Tunable Monochromatic Illumination and Digital Noise Reduction. *Cellular and Molecular Bioengineering* **1**, 146–156 (2008).

26. Su, T.-W., Seo, S., Erlinger, A. & Ozcan, A. High-throughput lensfree imaging and characterization of a heterogeneous cell solution on a chip. *Biotechnology and Bioengineering* **102**, 856–868 (2009).

27. Brady, D. J. *Optical imaging and spectroscopy*. (John Wiley & Sons, Hoboken, NJ, USA: 2009).

28. Lohmann, A. W. Wavefront Reconstruction for Incoherent Objects. *J. Opt. Soc. Am.* **55**, 1555_1–1556 (1965).

29. Mertz, L. *Transformation in Optics*. (John Wiley & Sons, Hoboken, NJ, USA: 1965).

30. Dubois, F., Joannes, L. & Legros, J.-C. Improved Three-Dimensional Imaging with a Digital Holography Microscope With a Source of Partial Spatial Coherence. *Appl. Opt.* **38**, 7085–7094 (1999).

31. Dubois, F., Novella Requena, M.-L., Minetti, C., Monnom, O. & Istasse, E. Partial spatial coherence effects in digital holographic microscopy with a laser source. *Appl. Opt.* **43**, 1131–1139 (2004).

32. Gopinathan, U., Pedrini, G. & Osten, W. Coherence effects in digital in-line holographic microscopy. *J. Opt. Soc. Am. A* **25**, 2459–2466 (2008).

33. Monroy, F., Rincon, O., Torres, Y. M. & Garcia-Sucerquia, J. Quantitative assessment of lateral resolution improvement in digital holography. *Optics Communications* **281**, 3454–3460 (2008).

34. Nunez, R. *Flow Cytometry for Research Scientists: Principles and Applications*. (Horizon Press: 2001).

35. Givan, A. L. *Flow Cytometry: First Principles*. (Wiley-Liss: 2001).

36. Owens, M. A. & Loken, M. R. *Flow Cytometry Principles for Clinical Laboratory Practice: Quality Assurance for Quantitative Immunophenotyping*. (Wiley-Liss: 1994).

37. Xiang, Q., Xu, B. & Li, D. Miniature real time PCR on chip with multi-channel fiber optical fluorescence detection module. *Biomedical Microdevices* **9**, 443–449 (2007).

38. Pamme, N., Koyama, R. & Manz, A. Counting and sizing of particles and particle agglomerates in a microfluidic device using laser light scattering: application to a particle-enhanced immunoassay. *Lab on a Chip* **3**, 187 (2003).

39. Fu, L.-M., Yang, R.-J., Lin, C.-H., Pan, Y.-J. & Lee, G.-B. Electrokinetically driven micro flow cytometers with integrated fiber optics for on-line cell/particle detection. *Analytica Chimica Acta* **507**, 163–169 (2004).

40. Novak, L., Neuzil, P., Pipper, J., Zhang, Y. & Lee, S. An integrated fluorescence detection system for lab-on-a-chip applications. *Lab Chip* **7**, 27–29 (2006).

41. Jacobson, S. C. & Ramsey, J. M. Electrokinetic Focusing in Microfabricated Channel Structures. *Anal. Chem.* **69**, 3212–3217 (1997).

42. Wolff, A. *et al.* Integrating advanced functionality in a microfabricated high-throughput fluorescent-activated cell sorter. *Lab on a Chip* **3**, 22 (2003).

43. Lancaster, C. *et al.* Rare cancer cell analyzer for whole blood applications: Microcytometer cell counting and sorting subcircuits. *Methods* **37**, 120–127 (2005).

44. Shi, J., Mao, X., Ahmed, D., Colletti, A. & Huang, T. J. Focusing microparticles in a microfluidic channel with standing surface acoustic waves (SSAW). *Lab Chip* **8**, 221–223 (2008).

45. Xuan, X. & Li, D. Focused electrophoretic motion and selected electrokinetic dispensing of particles and cells in cross-microchannels. *ELECTROPHORESIS* **26**, 3552–3560 (2005).

46. Yang, R.-J., Chang, C.-C., Huang, S.-B. & Lee, G.-B. A new focusing model and switching approach for electrokinetic flow inside microchannels. *Journal of Micromechanics and Microengineering* **15**, 2141–2148 (2005).

47. Chau, L.-K., Osborn, T., Wu, C.-C. & Yager, P. Microfabricated Silicon Flow-Cell for Optical Monitoring of Biological Fluids. *Analytical Sciences* **15**, 721–724 (1999).

48. Kamei, T. *et al.* Integrated Hydrogenated Amorphous Si Photodiode Detector for Microfluidic Bioanalytical Devices. *Anal. Chem.* **75**, 5300–5305 (2003).

49. Niehren, S., Kinzelbach, W., Seeger, S. & Wolfrum, J. An All-Solid-State Flow Cytometer for Counting Fluorescent Microspheres. *Anal. Chem.* **67**, 2666–2671 (1995).

50. Lin, C.-H., Lee, G.-B., Fu, L.-M. & Hwey, B.-H. Vertical focusing device utilizing dielectrophoretic force and its application on microflow cytometer. *Microelectromechanical Systems, Journal of* **13**, 923 – 932 (2004).

51. Xu, W., Jericho, M. H., Kreuzer, H. J. & Meinertzhagen, I. A. Tracking particles in four dimensions with in-line holographic microscopy. *Opt. Lett.* **28**, 164–166 (2003).

52. Heng, X. *et al.* Optofluidic microscopy-a method for implementing a high resolution optical microscope on a chip. *Lab Chip* **6**, 1274–1276 (2006).

53. Lew, M., Cui, X., Heng, X. & Yang, C. Interference of a four-hole aperture for on-chip quantitative two-dimensional differential phase imaging. *Opt. Lett.* **32**, 2963–2965 (2007).

54. Kim, N., Dempsey, C. M., Zoval, J. V., Sze, J.-Y. & Madou, M. J. Automated microfluidic compact disc (CD) cultivation system of Caenorhabditis elegans. *Sensors and Actuators B: Chemical* **122**, 511–518 (2007).

55. Saleh, B. E. A. & Teich, M. C. *Fundamentals of Photonics*. (2001).at <http://onlinelibrary.wiley.com/book/10.1002/0471213748>

56. Born, M. & Wolf, E. *Principles of Optics: Electromagnetic Theory of Propagation, Interference and Diffraction of Light*. (Cambridge University Press: 1997).

57. Seo, S., Su, T.-W., Tseng, D. K., Erlinger, A. & Ozcan, A. Lensfree holographic imaging for on-chip cytometry and diagnostics. *Lab Chip* **9**, 777–787 (2009).

58. Shaked, N. T., Satterwhite, L. L., Bursac, N. & Wax, A. Whole-cell-analysis of live cardiomyocytes using wide-field interferometric phase microscopy. *Biomed. Opt. Express* **1**, 706–719 (2010).

59. Granero, L., Micó, V., Zalevsky, Z. & García, J. Superresolution imaging method using phase-shifting digital lensless Fourier holography. *Opt. Express* **17**, 15008–15022 (2009).

60. Marquet, P. *et al.* Digital holographic microscopy: a noninvasive contrastimaging technique allowing quantitative visualization ofliving cells with subwavelength axial accuracy. *Opt. Lett.* **30**, 468–470 (2005).

61. Khmaladze, A. *et al.* Dual-wavelength linear regression phase unwrapping in three-dimensional microscopic images of cancer cells. *Opt. Lett.* **36**, 912–914 (2011).

62. Kemper, B. & von Bally, G. Digital holographic microscopy for live cell applications and technical inspection. *Appl. Opt.* **47**, A52–A61 (2008).

63. Miccio, L. *et al.* Dynamic DIC by digital holography microscopy for enhancing phase-contrast visualization. *Biomed. Opt. Express* **2**, 331–344 (2011).

64. Shaked, N. T., Zhu, Y., Rinehart, M. T. & Wax, A. Two-step-only phase-shifting interferometry with optimized detector bandwidth for microscopy of live cells. *Opt. Express* **17**, 15585–15591 (2009).

65. Sciammarella, C. A. & Sciammarella, F. M. Measurement of mechanical properties of materials in the micrometer range using electronic holographic moiré. *Opt. Eng.* **42**, 1215 (2003).

66. Rappaz, B., Charrière, F., Depeursinge, C., Magistretti, P. J. & Marquet, P. Simultaneous cell morphometry and refractive index measurement with dual-wavelength digital holographic microscopy and dye-enhanced dispersion of perfusion medium. *Opt. Lett.* **33**, 744–746 (2008).

67. Mudanyali, O. *et al.* Compact, light-weight and cost-effective microscope based on lensless incoherent holography for telemedicine applications. *Lab Chip* **10**, 1417–1428 (2010).

68. Dubois, F. *et al.* Digital Holographic Microscopy Working with a Partially Spatial Coherent Source. *Coherent Light Microscopy* **46**, 31–59 (2011).

69. Sherman, G. C. Application of the Convolution Theorem to Rayleigh's Integral Formulas. *J. Opt. Soc. Am.* **57**, 546–547 (1967).

70. Fienup, J. R. Reconstruction of an object from the modulus of its Fourier transform. *Opt. Lett.* **3**, 27–29 (1978).

71. Koren, G., Polack, F. & Joyeux, D. Iterative algorithms for twin-image elimination in in-line holography using finite-support constraints. *J. Opt. Soc. Am. A* **10**, 423–433 (1993).

72. Situ, G. & Sheridan, J. T. Holography: an interpretation from the phase-space point of view. *Opt. Lett.* **32**, 3492–3494 (2007).

73. Seo, S. *et al.* High-Throughput Lens-Free Blood Analysis on a Chip. *Analytical Chemistry* **82**, 4621–4627 (2010).

74. Stybayeva, G. *et al.* Lensfree Holographic Imaging of Antibody Microarrays for High-Throughput Detection of Leukocyte Numbers and Function. *Anal. Chem.* **82**, 3736–3744 (2010).

75. Bishara, W. *et al.* Holographic pixel super-resolution in portable lensless on-chip microscopy using a fiber-optic array. *Lab Chip* (2011).doi:10.1039/c0lc00684j

76. Mudanyali, O., Oztoprak, C., Tseng, D., Erlinger, A. & Ozcan, A. Detection of waterborne parasites using field-portable and cost-effective lensfree microscopy. *Lab Chip* **10**, 2419 (2010).

77. Björndahl, L. *et al. A Practical Guide to Basic Laboratory Andrology*. (Cambridge University Press: 2010).

78. Foote, R. H. The history of artificial insemination: Selected notes and notables. *J. Anim Sci.* **80**, 1–10 (2002).

79. World Health Organization *WHO Laboratory Manual for the Examination of Human Semen and Sperm-Cervical Mucus Interaction*. (Cambridge University Press: 1999).

80. Sokoloski, J. E., Blasco, L., Storey, B. T. & Wolf, D. P. Turbidimetric analysis of human sperm motility. *Fertil. Steril* **28**, 1337–1341 (1977).

81. Atherton, R. W., Radany, E. W. & Polakoski, K. L. Spectrophotometric quantitation of mammalian spermatozoon motility. I. Human. *Biol. Reprod* **18**, 624–628 (1978).

82. Atherton, R. W. *et al.* A correlation between a spectrophotometric quantitation of rabbit spermatozoan motility and velocity. *Arch. Androl* **3**, 301–308 (1979).

83. Levin, R. M., Shofer, J. & Greenberg, S. H. A quantitative method for determining the effects of drugs on spermatozoal motility. *Fertil. Steril* **33**, 631–635 (1980).

84. Levin, R. M., Greenberg, S. H. & Wein, A. J. Clinical use of the turbidimetric analysis of sperm motility: comparison with visual techniques. *Fertil. Steril* **35**, 332–336 (1981).

85. Morton, B. E. & Sagadraca, R. Quantitation of sperm population migration: capillary scanning assay. *Arch. Androl* **7**, 219–227 (1981).

86. Levin, R. M., Hypolite, J. A. & Wein, A. J. Clinical use of the turbidimetric analysis of sperm motility: an update. *Andrologia* **16**, 434–438 (1984).

87. Halangk, W. & Bohnensack, R. Quantification of sperm motility by a turbidimetric assay. Correlation to cellular respiration. *Biomed. Biochim. Acta* **45**, 331–341 (1986).

88. Jouannet, P., Volochine, B., Deguent, P., Serres, C. & David, G. Light scattering determination of various characteristic paramenters of spermatozoa motility in a serie of human sperm. *Andrologia* **9**, 36–49 (1977).

89. Naylor, G. P., Martin, J. S. & Chantler, E. N. Apparatus for the study of motile sperm using microprocessor analysis of scattered laser light. *Med Biol Eng Comput* **20**, 207–214 (1982).

90. Craig, T., Hallett, F. R. & Nickel, B. Motility analysis of circularly swimming bull spermatozoa by quasi-elastic light scattering and cinematography. *Biophys J* **38**, 63–70 (1982).

91. Woolford, M. W. & Harvey, J. D. Light-scattering studies of bull spermatozoa. II. Interaction and concentration effects. *Biophys J* **40**, 7–16 (1982).

92. Rigler, R. & Thyberg, P. Rotational and translational swimming of human spermatozoa: a dynamic laser light scattering study. *Cytometry* **5**, 327–332 (1984).

93. Earnshaw, J. C., Munroe, G., Thompson, W. & Traub, A. I. Automated laser light scattering system for assessment of sperm motility. *Med Biol Eng Comput* **23**, 263–268 (1985).

94. Frost, J. & Cummins, H. Motility assay of human sperm by photon correlation spectroscopy. *Science* **212**, 1520–1522 (1981).

95. Wilson, M. C. & Harvey, J. D. Twin-beam laser velocimeter for the investigation of spermatozoon motility. *Biophys. J* **41**, 13–21 (1983).

96. Wilson, M. C., Harvey, J. D. & Shannon, P. Aerobic and anaerobic swimming speeds of spermatozoa investigated by twin beam laser velocimetry. *Biophysical Journal* **51**, 509–512 (1987).

97. Mortimer, S. A critical review of the physiological importance and analysis of sperm movement in mammals. *Hum Reprod Update* **3**, 403–439 (1997).

98. Coetzee, K., de Villiers, A., Kruger, T. F. & Lombard, C. J. Clinical value of using an automated sperm morphology analyzer (IVOS). *Fertility and Sterility* **71**, 222–225 (1999).

99. Mortimer, S. T. CASA--practical aspects. *J. Androl* **21**, 515–524 (2000).

100. Agarwal, A. & Sharma, R. K. Automation is the key to standardized semen analysis using the automated SQA-V sperm quality analyzer. *Fertility and Sterility* **87**, 156–162 (2007).

101. Ramió, L. *et al.* Dynamics of motile-sperm subpopulation structure in boar ejaculates subjected to ‘in vitro’ capacitation and further ‘in vitro’ acrosome reaction. *Theriogenology* **69**, 501–512 (2008).

102. Maree, L., du Plessis, S. S., Menkveld, R. & van der Horst, G. Morphometric dimensions of the human sperm head depend on the staining method used. *Hum. Reprod.* **25**, 1369–1382 (2010).

103. Tomlinson, M. J. *et al.* Validation of a novel computer-assisted sperm analysis (CASA) system using multitarget-tracking algorithms. *Fertility and Sterility* **93**, 1911–1920 (2010).

104. Liu, D. Y., Clarke, G. N. & Baker, H. W. Relationship between sperm motility assessed with the Hamilton-Thorn motility analyzer and fertilization rates in vitro. *J Androl* **12**, 231–239 (1991).

105. Barratt, C. L., Tomlinson, M. J. & Cooke, I. D. Prognostic significance of computerized motility analysis for in vivo fertility. *Fertil. Steril* **60**, 520–525 (1993).

106. Kuo, Y. L. *et al.* New system for long-term monitoring of sperm motility: EDTA effect on semen. *Arch. Androl* **41**, 127–133 (1998).

107. Glenn, D. R. J., McVicar, C. M., McClure, N. & Lewis, S. E. M. Sildenafil citrate improves sperm motility but causes a premature acrosome reaction in vitro. *Fertility and Sterility* **87**, 1064–1070 (2007).

108. McCurnin, D. M. & Bassert, J. M. *Clinical Textbook for Veterinary Technicians*. (W.B. Saunders Company: 2002).

109. Clifford F. Shipley Breeding soundness examination of the boar. *Swine Health Prod* **7**, 117 (1999).

110. Turner, R. M. Current Techniques for Evaluation of Stallion Fertility. *Clinical Techniques in Equine Practice* **4**, 257–268 (2005).

111. About BabyStart Male Infertility Test (FertilMARQ). at <http://www.embryotech.com/babystart/bs-male/index.htm>

112. ContraVac - Products for Male Fertility. at <http://www.contravac.com/products/spermcheck/fertility.php>

113. Segerink, L. I., Sprenkels, A. J., Braak, P. M. ter, Vermes, I. & Berg, A. van den On-chip determination of spermatozoa concentration using electrical impedance measurements. *Lab Chip* **10**, 1018–1024 (2010).

114. Lindeberg, T. Edge Detection and Ridge Detection with Automatic Scale Selection. *Int. J. Comput. Vision* **30**, 117–156 (1998).

115. Su, T.-W. *et al.* Multi-angle lensless digital holography for depth resolved imaging on a chip. *Opt. Express* **18**, 9690–9711 (2010).

116. Chawla, A. Vasectomy follow-up: Clinical significance of rare nonmotile sperm in postoperative semen analysis. *Urology* **64**, 1212–1215 (2004).

117. Dhar, N. B., Bhatt, A. & Jones, J. S. Determining the success of vasectomy. *BJU Int* **97**, 773–776 (2006).

118. Su, T.-W., Erlinger, A., Tseng, D. & Ozcan, A. Compact and Light-Weight Automated Semen Analysis Platform Using Lensfree on-Chip Microscopy. *Analytical Chemistry* **82**, 8307–8312 (2010).

119. Lewis, S. E. M. Is sperm evaluation useful in predicting human fertility? *Reproduction* **134**, 31–40 (2007).

120. Phillips, D. M. Comparative analysis of mammalian sperm motility. *J Cell Biol* **53**, 561–573 (1972).

121. Rikmenspoel, R. Movement of Sea Urchin Sperm Flagella. *The Journal of Cell Biology* **76**, 310–322 (1978).

122. Serres, C., Feneux, D., Jouannet, P. & David, G. Influence of the flagellar wave development and propagation on the human sperm movement in seminal plasma. *Gamete Research* **9**, 183–195 (1984).

123. Ishijima, S., Oshio, S. & Mohri, H. Flagellar movement of human spermatozoa. *Gamete Research* **13**, 185–197 (1986).

124. Mortimer, S. T. & Swan, M. A. Variable Kinematics of Capacitating Human Spermatozoa. *Hum. Reprod.* **10**, 3178–3182 (1995).

125. Mortimer, S. T., Schëväert, D., Swan, M. A. & Mortimer, D. Quantitative Observations of Flagellar Motility of Capacitating Human Spermatozoa. *Hum. Reprod.* **12**, 1006–1012 (1997).

126. Woolley, D. M. & Vernon, G. G. A Study of Helical and Planar Waves on Sea Urchin Sperm Flagella, with a Theory of How They Are Generated. *J Exp Biol* **204**, 1333–1345 (2001).

127. Woolley, D. M. Motility of Spermatozoa at Surfaces. *Reproduction* **126**, 259–270 (2003).

128. Smith, D. J., Gaffney, E. A., Gadêlha, H., Kapur, N. & Kirkman-Brown, J. C. Bend propagation in the flagella of migrating human sperm, and its modulation by viscosity. *Cell Motility and the Cytoskeleton* **66**, 220–236 (2009).

129. Gillies, E. A., Cannon, R. M., Green, R. B. & Pacey, A. A. Hydrodynamic propulsion of human sperm. *Journal of Fluid Mechanics* **625**, 445 (2009).

130. Friedrich, B. M., Riedel-Kruse, I. H., Howard, J. & Jülicher, F. High-precision tracking of sperm swimming fine structure provides strong test of resistive force theory. *Journal of Experimental Biology* **213**, 1226 –1234 (2010).

131. Gurarie, E., Grünbaum, D. & Nishizaki, M. Estimating 3D Movements from 2D Observations Using a Continuous Model of Helical Swimming. *Bulletin of Mathematical Biology* **73**, 1358–1377 (2011).

132. Ishijima, S. Mechanical constraint converts planar waves into helices on tunicate and sea urchin sperm flagella. *Cell Struct. Funct.* **37**, 13–19 (2012).

133. Crenshaw, H. C. A New Look at Locomotion in Microorganisms: Rotating and Translating. *Amer. Zool.* **36**, 608–618 (1996).

134. Crenshaw, H. C., Ciampaglio, C. N. & McHenry, M. Analysis of the Three-Dimensional Trajectories of Organisms: Estimates of Velocity, Curvature and Torsion from Positional Information. *J Exp Biol* **203**, 961–982 (2000).

135. Corkidi, G., Taboada, B., Wood, C. D., Guerrero, A. & Darszon, A. Tracking sperm in three-dimensions. *Biochemical and Biophysical Research Communications* **373**, 125–129 (2008).

136. Malkiel, E., Sheng, J., Katz, J. & Strickler, J. R. The Three-Dimensional Flow Field Generated by a Feeding Calanoid Copepod Measured Using Digital Holography. *J Exp Biol* **206**, 3657–3666 (2003).

137. Jericho, S. K., Garcia-Sucerquia, J., Xu, W., Jericho, M. H. & Kreuzer, H. J. Submersible digital in-line holographic microscope. *Review of Scientific Instruments* **77**, 043706–043706–10 (2006).

138. Lewis, N. I. *et al.* Swimming speed of three species of Alexandrium (Dinophyceae) as determined by digital in-line holography. *Phycologia* **45**, 61–70 (2006).

139. Heydt, M. *et al.* Digital In-Line Holography as a Three-Dimensional Tool to Study Motile Marine Organisms During Their Exploration of Surfaces. *The Journal of Adhesion* **83**, 417–430 (2007).

140. Sheng, J. *et al.* Digital Holographic Microscopy Reveals Prey-Induced Changes in Swimming Behavior of Predatory Dinoflagellates. *PNAS* **104**, 17512–17517 (2007).

141. Frentz, Z., Kuehn, S., Hekstra, D. & Leibler, S. Microbial population dynamics by digital in-line holographic microscopy. *Review of Scientific Instruments* **81**, 084301–084301–6 (2010).

142. Sohn, M. *et al.* Determination of the swimming trajectory and speed of chain-forming dinoflagellate Cochlodinium polykrikoides with digital holographic particle tracking velocimetry. *Marine Biology* **158**, 561–570 (2011).

143. Lee, S. J., Seo, K. W., Choi, Y. S. & Sohn, M. H. Three-dimensional motion measurements of free-swimming microorganisms using digital holographic microscopy. *Measurement Science and Technology* **22**, 064004 (2011).

144. A. Greenbaum, U. Sikora & A. Ozcan Field-portable wide-field microscopy of dense samples using multi-height pixel super-resolution based lensfree imaging. *Lab on a Chip* (2012).doi:10.1039/C2LC21072J

145. Isikman, S. O. *et al.* Lens-free optical tomographic microscope with a large imaging volume on a chip. *Proceedings of the National Academy of Sciences* (2011).doi:10.1073/pnas.1015638108

146. Crocker, J. C. & Grier, D. G. Methods of Digital Video Microscopy for Colloidal Studies. *Journal of Colloid and Interface Science* **179**, 298–310 (1996).

147. World Health Organization *WHO Laboratory Manual for the Examination of Human Semen and Sperm-Cervical Mucus Interaction*. (Cambridge University Press: 1999).

148. Herraiz, J. L. *et al.* GPU acceleration of a fully 3D Iterative Reconstruction Software for PET using CUDA. *2009 IEEE Nuclear Science Symposium Conference Record (NSS/MIC)* 4064–4067 (2009).doi:10.1109/NSSMIC.2009.5402402

149. Winet, H., Bernstein, G. S. & Head, J. Observations on the Response of Human Spermatozoa to Gravity, Boundaries and Fluid Shear. *J Reprod Fertil* **70**, 511–523 (1984).

150. Cosson, J., Huitorel, P. & Gagnon, C. How spermatozoa come to be confined to surfaces. *Cell Motil. Cytoskeleton* **54**, 56–63 (2003).

151. Smith, D. J., Gaffney, E. A., Blake, J. R. & Kirkman-Brown, J. C. Human Sperm Accumulation Near Surfaces: A Simulation Study. *Journal of Fluid Mechanics* **621**, 289–320 (2009).

152. Elgeti, J., Kaupp, U. B. & Gompper, G. Hydrodynamics of Sperm Cells near Surfaces. *Biophysical Journal* **99**, 1018–1026 (2010).

153. Sung Cheol Park, Min Kyu Park & Moon Gi Kang Super-resolution image reconstruction: a technical overview. *IEEE Signal Process. Mag.* **20**, 21–36 (2003).

154. Hardie, R. C., Barnard, K. J. & Armstrong, E. E. Joint MAP registration and high-resolution image estimation using a sequence of undersampled images. *IEEE Trans. on Image Process.* **6**, 1621–1633 (1997).

155. Woods, N. A., Galatsanos, N. P. & Katsaggelos, A. K. Stochastic methods for joint registration, restoration, and interpolation of multiple undersampled images. *IEEE Trans. on Image Process.* **15**, 201–213 (2006).

156. Luenberger, D. *Linear and nonlinear programming*. (Addison-Wesley: Reading Mass., 1984).

157. Bishara, W., Su, T.-W., Coskun, A. F. & Ozcan, A. Lensfree on-chip microscopy over a wide field-of-view using pixel super-resolution. *Opt. Express* **18**, 11181–11191 (2010).

158. Clack, N. G., Salaita, K. & Groves, J. T. Electrostatic readout of DNA microarrays with charged microspheres. *Nat Biotech* **26**, 825–830 (2008).

159. Sheng, J., Malkiel, E. & Katz, J. Digital holographic microscope for measuring three-dimensional particle distributions and motions. *Appl. Opt.* **45**, 3893–3901 (2006).

160. Lee, S.-H. *et al.* Characterizing and tracking single colloidal particles with video holographic microscopy. *Opt. Express* **15**, 18275–18282 (2007).

161. Soulez, F., Denis, L., Fournier, C., Thiebaut, E. & Goepfert, C. Inverse-problem approach for particle digital holography: accurate location based on local optimization. *J. Opt. Soc. Am. A* **24**, 1164–1171 (2007).

162. Canham, P. B. & Burton, A. C. Distribution of Size and Shape in Populations of Normal Human Red Cells. *Circulation Research* **22**, 405–422 (1968).

163. Shvalov, A. N. *et al.* Light-Scattering Properties of Individual Erythrocytes. *Appl. Opt.* **38**, 230–235 (1999).

164. Morgan, J. S., Slater, D. C., Timothy, J. G. & Jenkins, E. B. Centroid position measurements and subpixel sensitivity variations with the MAMA detector. *Appl. Opt.* **28**, 1178–1192 (1989).

165. Ares, J. & Arines, J. Influence of Thresholding on Centroid Statistics: Full Analytical Description. *Appl. Opt.* **43**, 5796–5805 (2004).

166. Alexander, B. F. & Ng, K. C. Elimination of systematic error in subpixel accuracy centroid estimation [also Letter 34(11)3347-3348(Nov1995)]. *Opt. Eng.* **30**, 1320–1331 (1991).

167. Armitage, P. An overlap problem arising in particle counting. *Biometrika* **36**, 257–266 (1949).